Examining Low Frequency Molecular Modulations from the High Frequency Vantage Point: Anharmonically-Coupled Low Frequency Modes in PCET Model Systems

Anthony Reynolds

A dissertation

submitted in partial fulfillment of the

requirements for the degree of

Doctor of Philosophy

University of Washington

2015

Reading Committee:

Munira Khalil, Chair

Gary Drobny

Xiaosong Li

Program Authorized to Offer Degree

Chemistry

University of Washington

ABSTRACT

Examining Low Frequency Molecular Modulations from the High Frequency Vantage Point: Anharmonically-Coupled Low Frequency Modes in PCET Model Systems

Anthony Reynolds

Chair of the Supervisory Committee:
Associate Professor Munira Khalil
Department of Chemistry

Proton-coupled electron transfer model systems (PCET) are examined using polarization selective femtosecond infrared pump-probe spectroscopy to determine how the structural modes are coupled to the OH/OD stretching vibrational mode by monitoring low frequency oscillations in the ν_{OH}/ν_{OD} mode using pump-probe techniques. For all of the systems discussed in this dissertation, low frequency modes are anharmonically coupled to the OH/OD stretching vibration.

The OH/OD stretching vibration discussed in this dissertation have complex and broad lineshapes in the infrared region (IR) that are difficult to decipher. A broadband IR (BBIR) source, when used as part of a third order nonlinear infrared pump-probe spectroscopy, gains access into the electronic ground state potential energy surface. This information reveals the molecular dynamics that give rise to the complex structure in an IR spectra. The BBIR used for these experiments is generated by focusing 800 nm/400 nm pulses into compressed air and is tunable from 2 – 5 microns with a FWHM greater than 1200 wavenumbers. The BBIR is a crucial mid-

IR source in subsequent chapters for examining the broad lineshapes of the OH/OD stretching mode, which often exceeds 200 wavenumbers.

The coupling of low frequency structural modulations to hydrogen bonding dynamics in PCET systems is explored by using the OH/OD stretching vibration in CCl_4 or $CHCl_3$. Third order nonlinear ultrafast infrared pump-probe spectroscopy is used to gather information on the high frequency OH/OD stretching vibrational modes in the ground state such as vibrational relaxation time and anharmonic vibrational coupling to low frequency structural modulations. At least one anharmonically coupled low frequency mode between 120 and 250 wavenumbers has been observed in all systems. To better understand and visualize how the low frequency mode may contribute to the PCET chemistry, we calculated the fundamental frequencies and third order coupling constants using Gaussian09. These calculations show a low frequency modulation along the reaction coordinate at a similar frequency. This information will allow us to unravel how hydrogen bonding dynamics are involved in the PCET process.

TABLE OF CONTENTS

LIST OF FIGURES

LIST OF TABLES

GLOSSARY

1D: 1-dimensional

2D: 2-dimensional

A: Analyzer

$AgGaS_2$: Silver gallium sulfide

BBIR: Broadband infrared

BBO: β-Barium borate

BS: Beam splitter

CL: Calcite crystal

CM: Curved mirror

D: Deuterium

DBQ: 10-deuteroxybenzo[h]quinoline

DFG: Difference frequency generation

DFT: Density Functional Theory; here describes the type of calculation, i.e. quantum mechanical

DOAr-ND_2: C-(3,5-di-*tert*-butyl-2-hydroxyphenyl)-C,C-diphenylmethylamine

DOAr-Py: 3,5-di-*tert*-butyl-2-hydroxy-phenylpyridine

ESA: Excited state absorption

ESIPT: Excited-state intramolecular proton transfer

ET: Electron Transfer

FFT: Fast Fourier-Transform

FO: Focusing optic

fs: femtosecond

FT: Fourier-Transform

FTIR: Fourier-Transform Infrared

FWHM: full-width half-maximum

GC: Gas cell

GS: Ground state

GSB: Ground state bleach

GVM: Group velocity mismatch

HAT: Hydrogen atom transfer

HBQ: 10-hydroxybenzo[h]quinoline

HgCdTe: Mercury cadmium telluride

HWP: Half-waveplate

I: Intensity; Absolute Square of the electric field

Iso: Isotropic

IR: Infrared

MCT: Mercury cadmium telluride detector

MIR: mid-infrared

Mono: Monochromator

ν_{OD}: Deuteroxyl vibrational stretching mode

ν_{OH}: Hydroxyl vibrational stretching mode

OEC: Oxygen evolving complex

OPA: Optical parametric amplifier

P: Polarization optic

P_{680}^{+}: Chlorophyll containing pigments with an absorption spectrum peaked at 680 nm.

PES: Potential energy surface

PCET: Proton-coupled electron transfer

PM: Off-axis parabolic mirror

PP: Pump-probe

ps: picosecond

PS II: Photosystem II

PT: Proton transfer

SH: Second harmonic

S: Sample

Si: Silicon

Sig: Signal

SPIDER: Spectral phase interferometry for direct-electric field reconstruction

SNP: Sodium nitroprusside

W: Watt

XFROG: Cross-correlation frequency-resolved optical gating

ZZZZ: All fields of electric field are parallel to one another

ZZYY: The first two electric field interactions are crossed relative to the last two electric field interactions

ZZMM: The isotropic polarization response

DEDICATION

In memory of my father.

ACKNOWLEDGEMENTS

There are many people who have helped me along this long and arduous path toward completing my PhD in chemistry. The list of individuals is far too long, and there are far too few words to express my utmost gratitude. I would like to start by thanking Professor Munira Khalil for accepting me into her group during the summer of 2009. I came into the group with essentially no knowledge of infrared spectroscopy beyond a desktop IR instrument typically seen in undergraduate chemistry laboratory courses. With the help of Munira and senior graduate students Mike Lynch, Mark Cheng, and Ben Van Kuiken; I was able to slowly come to terms with the optics. Munira trusted me with the lab during the first round of experiments with the compounds from the Jim Mayer lab. She placed greater trust in me to continue the development of the second lab and collect my finishing set of data that is presented in this work. Furthermore, she had patience to stick with me despite my tendency to injure myself at the most inopportune moments, e.g. fracture of my right fibula from a mountain bike wreck June of 2013. Again I want to thank you, Munira.

The third group of students to join the Khalil lab included Jennifer (aka Jen) Brooks, Karla Slenkamp (spelled with a "k" and not a "c") and myself. As we trickled into the group over the course of our first year in graduate school, we quickly developed a close relationship that budded into a family away from home as we helped each other with course work and learned our way around the optics lab. We shared the fruits of our labor as well as the bitterness of many trials and tribulations. Karla assisted me during my first round of data collection despite my inability to acquire quality data during that period of my academic career. Jen and I also shared some unique experiences, some of which were less than ideal. The death of a parent is no easy matter to overcome. Unfortunately, Jen and I had to face that situation sooner rather than later with her

mother and my father passing. We both discovered that no words help alleviate that pain. It is situations like these that helped forge our relationship into professional scientists as well as a family. I would like to thank them for intellectually stimulating conversations over these past years as well as support during the bitter and sweet moments.

I would also like to thank the younger graduate students; Madhumitha Balasubramanian, Zach Fox, and James Gaynor for their engaging and challenging discussions that were key to my development. I hope that we laid a solid foundation to build upon in lab as well as an inviting social dynamic that encouraged engaging discussions in and out of the lab. The current group of post-docs, Matthew Ross and Trevor Courtney, were also key in what was likely the greatest improvement of my knowledge in ultrafast optics, as they were willing to discuss details thoroughly.

Indeed my family has played no small role in contributing to my academic career. I would like to thank my parents, Anita Steffey and Gary Reynolds, for bringing me into this world and nurturing me into a scientist. They sacrificed much so I could be the first in our family to finish my BA as well as my PhD. Unfortunately, my father was only able to watch me begin my graduate career. His life was too short, and I miss him dearly. I do not need to look too far to see his obsessive-compulsive nature in my own behavior. The orderliness that resulted from this inherited behavior was key to helping me organize my tools mentally and physically for quick, efficient access. My brothers, Ethan and Bryan, and I helped each other during that rough patch of life as our father and grandfather, Mont Reynolds, passed. We will always cherish the memories created in our youth.

My mother helped stimulate my thinking with her constant care packages of fresh jellies and jams that she made. Her annual visits helped make Seattle feel more like home and less like

a distant planet despite the long distance from my beginnings in Virginia. My weekends and holidays were a little warmer because of these gifts. I would also like to thank my step-father, Ronald Steffey, and the Steffey family for accepting me into their family. Their guidance has helped me develop a work ethic that was an essential ingredient for this process.

Over the past year and a half I have been fortunate enough to meet and know a particular person that has had a major impact in my life. My love for you, Erin, continues to grow with each passing day. Her ability to comfort me during trying moments, enjoy new experiences with me, and allow me to help her have been a key element to motivating me to finish strong. Her editing skills have helped make the task of writing this thesis much easier. I am excited to see what our future holds hand in hand, together. Doctors together.

CHAPTER 1

Introduction

1.1 Good Vibrations: Molecular Vibrations Assisting Charge Transfer Processes

The ability of flora to convert sunshine, water and carbon dioxide in stored energy in the form of hydrocarbon chains has been fascinating and inspiring people for centuries [1-4]. The underlying story of these chemical events has been a difficult one to unravel. Many biology and biochemistry texts books among other works have devoted chapters to the history and current understanding of photosynthesis [5, 6]. Photovoltaic devices are direct evidence of trying to mimic this phenomenon. Understanding the efficiency of charge transfer reactions in photosynthesis is crucial to improving the efficiency and cost effectiveness of photovoltaics. One of the key components of photosynthesis that has been incredibly difficult to understand is the molecular dynamics associated with charge transfer [7-9]. Recent work has hypothesized that hydrogen bonding plays a significant role in these dynamical processes. For example, studies on photosystem II (PS II) has shown the oxidation of the tyrosine residue involves long chain electron transfer to P_{680}^{+} accompanied by the transfer of the phenolic proton to a hydrogen-bonded imidazole [7, 10-17]. This reaction process is pivotal in the oxidation of water in the oxygen evolving complex (OEC) of PS II.

How do low frequency molecular motions affect the hydrogen bonding and what role does this play in the proton transfer? If we consider that slowly evolving structural modulations have some effect on the hydrogen bonding, then how would this manifest itself and how could we observe this effect. These question would yield information necessary for unraveling the mysteries related to the electron and proton transfer reaction mechanisms and quantum efficiency of photosynthesis. This demonstrates how important it is to have a molecular-level understanding of

these reactions. In order to get a molecular picture of these processes, it is necessary to build experimental tools that can examine the ground state dynamics. The goal of this dissertation is build a window into the time-evolving molecular structure of these systems and to examine how these dynamics affect the potential energy surface.

1.2 Importance of proton-coupled electron transfer reactions

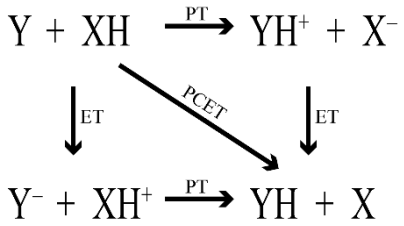

Figure 1.2.1: Basic square diagram of proton transfer (PT) and electron transfer (ET) reaction pathways. In this diagram, the separate electron transfer and proton transfer reactions occur along the edges of the square while the diagonal pathway represents the PT and ET reactions occurring in a single step. These reaction pathways, PT, ET, or PCET, can be applied to both hydrogen bonding systems and non-hydrogen bonding systems.

Proton-coupled electron transfer (PCET) reactions are of major significance in many chemical and biological processes [8-12, 18]. Until recently these reactions were viewed as two chemical events where the electron transfer (ET) reaction is the result an electron transferring from a donor X to acceptor Y^+ as shown by the left edge of Figure 1.2.1. This reaction is followed by a proton transfer (PT) reaction where the proton is transferred from an acid XH^+ to a base Y^-, as shown by the lower reaction pathway of Figure 1.2.1. One particular example of this reaction type is hydrogen atom transfer (HAT) where the proton and electron transfer occur along a common path. HAT reactions are important in many chemical processes such as oxidation and chemical syntheses to name a few and for this reason many studies have been devoted to this chemical process. One particular industrial application of this reaction type is the oxidation of *para*-xylene to terephthalic acid which occurs on a massive scale for the manufacture of polyester.

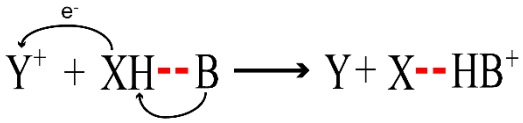

Figure 1.2.2: Basic scheme of a proton-coupled electron transfer reaction involving hydrogen bonding systems. In this reaction, the electron is transferred to an acceptor Y^+ from a donor parent X and the proton is transferred from donor parent X to a hydrogen bonded base B in a single concerted step. The reaction proceeds to form acceptor systems Y and HB^+ which is hydrogen bonded to the donor system X. This reaction pathway can occur between inter and intra-molecular hydrogen bonding systems.

However, recent work has shown that a small -yet growing- subset of this process occurs in a singular concerted step as shown by the diagonal pathway in Figure 1.2.1 [19]. The thermodynamic difference between concerted and step-wise mechanism can profound in some instances. In the instance of the concerted mechanism, a small addition of energy to the system yields a desirable product from what would be an energetically unfavorable reaction in a step-wise mechanism. Furthermore, hydrogen bonding can also play a pivotal role in this charge transfer process [20]. The oxidation of water in the OEC of photosystem II is one example mentioned is one of many in biology that follow the basic pathway shown in Figure 1.2.2. Another example is the electron transfer from heme a^{2+} to $heme_3^{3+}$ coupled to a proton transfer to the binuclear center [21-25].

The ubiquity of PCET reactions has led to numerous studies aiming to model and understand the overall chemical process. Electrochemical studies and quantum mechanical calculations have given credence for using nonadiabatic Marcus theory to describe the concerted proton-electron transfer [8, 26, 27]. Hammes-Schiffer *et al.* have shown fluctuations along the reaction coordinate are heavily reflected in the reorganizational energy and the quantum coupling of the electron and proton [28, 29]. In addition time-resolved electronic spectroscopy studies on photosynthetic systems have shown that low frequency vibrational modes play a significant role

in the charge transfer process [30, 31]. Understanding the effects of low frequency modes on fluctuations of the reaction coordinate will afford a window into the PCET reaction.

1.3 Applying vibrational spectroscopy to this unique problem

The vibrational transitions of molecules are highly sensitive to molecular properties and structure [32, 33]. The information gathered from vibrational spectroscopy provides a unique window into the molecular structure and dynamics. Linear continuous wave FTIR experiments provide limited insight into structural information and dynamical information of the PCET model compounds. The complexity of the line shapes limits what information can be extracted from a linear experiment [34]. Nonlinear ultrafast vibrational spectroscopy, such as the pump-probe pulse sequence in Figure 1.3.1 A, allows us to gain an understanding of the local environments that give rise to the line shapes as well as dynamical information [35, 36].

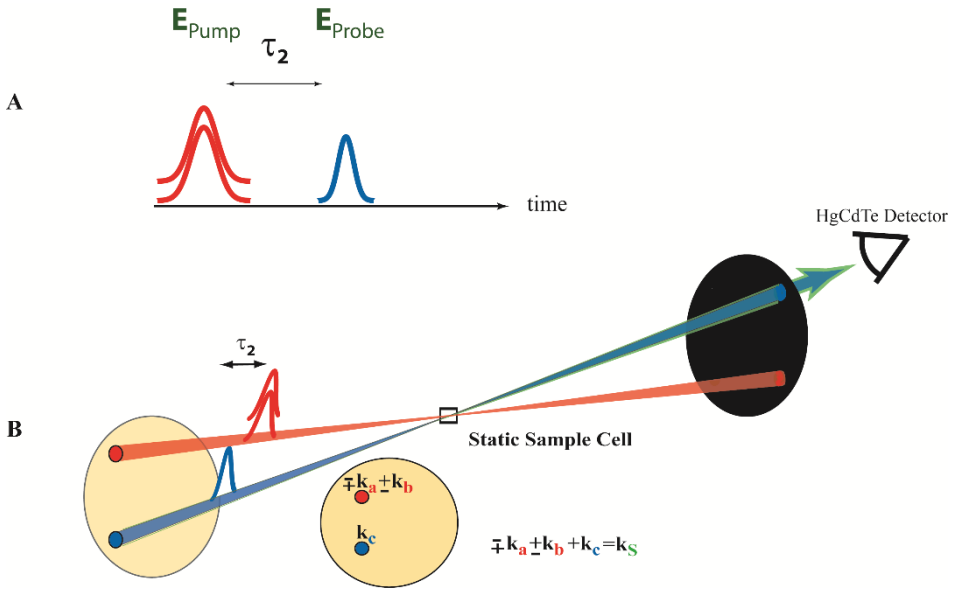

Figure 1.3.1: A) Pulse sequence for an ultrafast 3rd order nonlinear infrared pump-probe experiment. The E_{Pump} field interacts twice with the sample followed by some waiting time τ_2 after which the E_{Probe} field interacts with the sample resulting in a transient absorption on the first vibrational excited state or ground state bleach. **B)** The alignment of the three fields of pulse sequence in **A** onto a static sample cell in a pump-probe geometry. As indicated by the electric field vectors $\mathbf{k_a}$, $\mathbf{k_b}$, $\mathbf{k_c}$, and $\mathbf{k_s}$ for the three light-matter interactions that occur in a pump-probe experiment of which two are from the pump field, $\mathbf{k_a}$ and $\mathbf{k_b}$, and are indistinguishable from one another. The pump-field interactions with a sample and one interaction from the probe field $\mathbf{k_c}$ results in a signal field, $\mathbf{k_s}$, co-propagating with the probe field which is directed onto a Mercury Cadium Telluride (HgCdTe) detector.

Sub-picosecond resolution of ultrafast vibrational spectroscopy affords the possibility to investigate these dynamics as well as gain other information about the potential energy surface.

Vibrational lifetimes of molecules and anharmonicities give meaningful insight into the molecular dynamics that drive PCET. One such method of measuring these dynamics is pump-probe spectroscopy (see Figure 1.3.1 B). The theoretical framework necessary to understand how molecular response will manifest themselves in a spectrum retrieved from ultrafast 3rd order nonlinear spectroscopy, such as a pump-probe experiment, has been explained in great detail by Sung and Silbey [37] as well as many others [35, 38, 39].

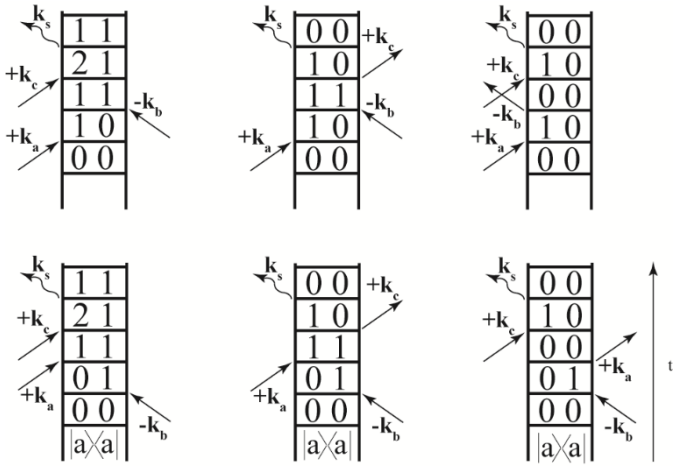

Figure 1.3.2: A sample of double sided Feynman diagrams for a three-level system "a" perturbed by a 3rd order nonlinear experiment. The side arrow indicates the direction of time. The electric field vectors aligned in the phase matching condition shown in Figure 1.3.1 are represented by $\mathbf{k_a}$, $\mathbf{k_b}$, and $\mathbf{k_c}$ following a sequential time ordering, t. The vibrational signal produced by the three light-matter interactions is produced in the $\mathbf{k_s}$ direction.

Feynman diagrams in Figure 1.3.2 offer an intuitive picture of the quantum pathways of a 3-level system perturbed by the pump and probe electromagnetic fields shown in Figure 1.3.1. The first diagram on the top row represents the system **a** being "walked" up the vibrational ladder to the first excited state. The first interaction with the pump-field $\mathbf{k_1}$ places the system in a coherence between the first excited state and the ground state ($\nu = 0 \rightarrow 1$, ν_{01}) on the bra side. The second pump interaction $\mathbf{k_2}$ populates the first excited state ($\nu = 1$) by placing the ket side into the first excited state. The probe-field interaction $\mathbf{k_3}$ places the system in a coherence between the first and second excited states ($\nu = 1 \rightarrow 2$, ν_{12}) after the waiting time τ_2 as shown in Figure 1.3.1B. This results in an emitted signal $\mathbf{k_s}$ at the frequency of the coherence ν_{12} as shown in Figure 1.3.3 which is the positive peak resulting from the excited state absorption (ESA) response.

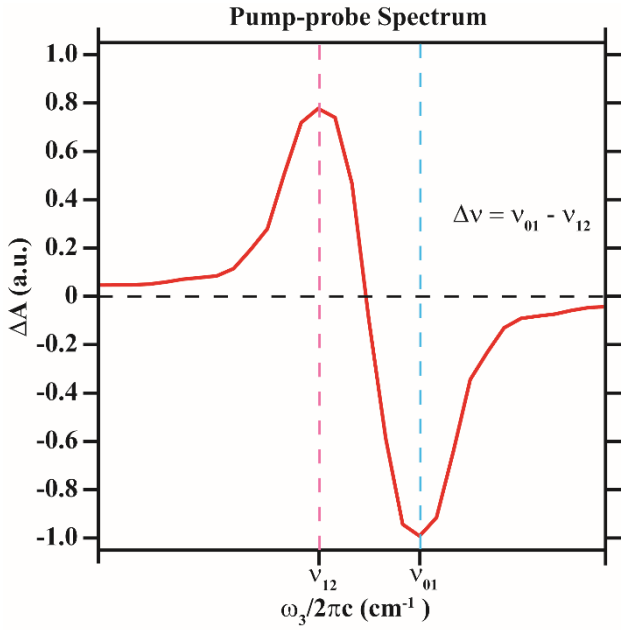

Figure 1.3.3: Cartoon pump-probe spectrum at τ_2 = 0 fs, where the positive peak is the excited state absorption at the coherence between the first and second excited vibration states, ν_{12}. The negative peak is the ground state bleach representing the coherence between the ground state and first excited vibration state, ν_{01}. The anharmoncity $\Delta\nu$ of the vibrational potential energy surface from the difference of the two states, $\Delta\nu = \nu_{01} - \nu_{12}$.

The second and third Feynman diagrams in Figure 1.3.2 give rise to the ground state bleach, ν_{01}, in a similar manner. In all, there are six Feynman diagrams that give rise to Figure 1.3.3 where four contribute to the ground state bleach (fundamental transition) and two give rise to the excited state absorption (overtone transition). Pump-probe spectroscopy examines all of these contributions to the fundamental and overtone transitions as a function of the waiting time, therefore gathering information about the anharmonicity ($\Delta\nu$) of the potential energy surface as well as vibrational lifetimes.

Pump-probe spectroscopy is an excellent tool for examining molecular dynamics through the O-D bond [40-43]. Elsaesser's *et al.* work on strongly hydrogen-bonding systems such as acetic acid dimers and Hayashi's work on benzoic acid dimers have given a framework through which we can begin to unravel how strong hydrogen bonding manifests itself in ultrafast studies

[44, 45]. Their work among others have shown vibrational lifetimes of the OD/OH stretch (ν_{OD}/ν_{OH}) are relatively fast 150-250 fs and are quite often correlated with low frequency structural modes generally around 50-150 cm^{-1} [43, 46, 47]. Additionally, work on hetero-dimers such as the 7-Azaindole-Pyrrolo[3,2 h]quinoline dimer by Petersen and co-workers[48] and asymmetric dimers like formic acid/pyridine dimers by Cheatum *et al.*[49] have shown that these strongly hydrogen-bonding systems exhibit similar dynamics with fast population decay <1 ps and low frequency structural oscillations 50-200 cm^{-1} anharmonically coupled to the $\nu_{OD/ND}$ mode [50]. In addition work on the ν_{OD} in HOD as well as other strong hydrogen bonding systems have shown two component population decay dynamics with a fast component correlating with a decay of 140 - 250 fs and slower component correlation with ~1 ps [45, 46, 51-54].

1.4 Motivation for a broadband IR source

Rudimentary interpretation of the hydroxyl stretching vibrational transition ν_{OH} in alcohols taught in undergraduate chemistry courses suggest a very broad yet weak IR absorption near 3300 wavenumbers. While this very basic picture is rather reliable it does have its limitations. Many of the hydroxyl transitions studied in this work have broad absorptions around 2800 wavenumbers which could be easily misinterpreted for alkyl stretch if one adheres to this guideline from basic organic chemistry too tightly. However, what we can glean from this "guideline" is that transition is typically weak and broad. The conventional methods for generating IR light for ultrafast experiments as outlined above generally have a bandwidth of 250-300 wavenumbers of bandwidth which is quite substantial for many vibrational transitions which are quite narrow, 5 - 25 wavenumbers in bandwidth, and strong. For example, the cyano- vibrational mode of Sodium nitroprusside that is centered at ~2144 cm^{-1} has a bandwidth corresponding to ~20 cm^{-1} [55, 56].

However, hydroxyl transitions can be very broad with the lineshape exceeding 200 to 300 wavenumbers for the fundamental transition of the hydroxyl mode [57, 58]. The bandwidth of the hydroxyl stretch in 10-hydroxybenzo[h]quinoline (see Section 5) stretch is ~447 cm^{-1} and has significantly more bandwidth than the conventional mid-IR source. This creates quite a dilemma for a vibrational spectroscopist as this make it exceedingly difficult to pump and probe the entire ν_{OH} utilizing a single mid-IR light source generated by conventional methods that typically has maximal bandwidths of approximately 300 cm^{-1}. One way examine these types of systems by conventional means is to employ a two-color system where you have two optical setups where one is tuned to generate light at the fundamental transition frequency to pump that transition while tuning the second in a piecewise manner in order to scan across the fundamental and overtone transitions. While this does achieve the ability to examine these systems it adds another layer of complexity to the optical makeup of the experiment while increasing the time needed to conduct the experiment. Additionally this also adds another layer of complexity to the analysis and interpretation of the data collected [59].

Another way of examining these very broad IR transitions is using a broadband IR (BBIR) source. Recently several groups have reported on the ability to generate ultra-broad continua in the IR region [60-63]. From our previous work to develop and characterize this source we can generate mid-IR with bandwidths exceeding 1000 wavenumbers and is tunable such that we can optimally probe the ν_{OH} or ν_{OD} modes [63]. For this reason, BBIR provides an excellent tool to probe the entire ν_{OH} region while also allowing the ability to examine other nearby vibrational transitions for possible coupling. However, BBIR is not without its limitations. While tuned to the region of interest for either ν_{OD} or ν_{OH} the peak power of the BBIR is approximately 80 nJ. This is adequate for single interaction but not enough for all three light-matter interactions

necessary for the experiments previously outlined. With the current output of the BBIR, the signal quality would be greatly reduced if used for all three light-matter interactions. Thus throughout this dissertation the conventional methods for generating mid-IR will be utilized for the pump-field (~400 nJ of mid-IR) and the BBIR will be used for the probe-field.

1.5 PCET model systems

We have chosen four model systems 3,5-di-*tert*-butyl-2-hydroxy-phenylpyridine (DOArm-Py), C-(3,5-di-*tert*-butyl-2-hydroxyphenyl)-C,C-diphenylmethylamine (DOAr-ND_2), and 10-hydroxybenzo[h]quinoline (HBQ) as well as it's deuteroxyl counterpart, 10-deuteroxybenzo[h]quinoline, (DBQ) were investigated due to its similarity to the oxidizing region of photosystem II (Fig 1.5.1).

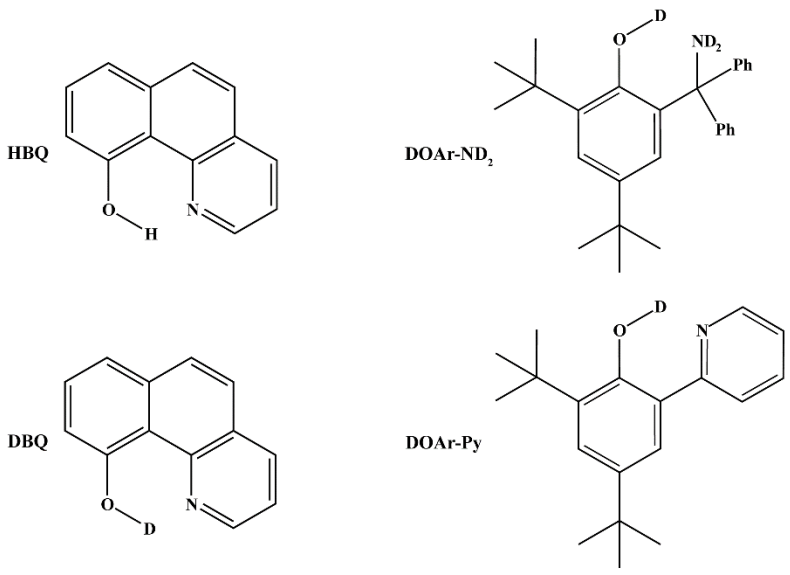

Figure 1.5.1: The four model systems chosen for this study DOAr-Py, DOAr-ND_2, HBQ, and DBQ

Electrochemical studies such as kinetics by Rhile and co-workers have been conducted on the DOAr-Py and DOAr-ND_2 complex. These studies have shown both model system undergoes

proton transfer (PT) and electron transfer (ET) in a single concerted step [10]. Ultrafast fluorescence and transient absorption studies by Chou and co-workers have been conducted on the HBQ and DBQ which also indicate this system also undergoes PT and ET [64]. However, their work does not indicate that this was in a single concerted step nor does it exclude the possibility. The role structural dynamics plays in the proton transfer of these type of reactions are not well characterized. Understanding the effects of low frequency modes on fluctuations of the reaction coordinate will afford a window into the PCET reaction.

1.6 Dissertation overview

This dissertation includes the implementation and application of a tunable broadband IR source on highly anharmonic model systems that are similar to those found in many biological systems. Chapter 2 briefly describes the development of the BBIR source. Furthermore, Chapter 2 describes the implementation and initial workup required to develop acquired data into usable spectra followed by the analytical methods employed for fitting the data as well as modeling of the data using quantum mechanical calculations of the vibrational spectra and anharmonic coupling terms using Gaussian09C [65]. Chapter 3 describes initial pump-probe studies on DOAr-Py prior to the implementation of the BBIR followed by the implementation of the BBIR in pump-probe spectroscopy on DOAr-ND_2. Chapter 4 describes the pump-probe studies on HBQ and its deuterated counterpart DBQ.

References

1. Tedder, J.M., *Which Factors Determine the Reactivity and Regioselectivity of Free Radical Substitution and Addition Reactions?* Angewandte Chemie International Edition in English, 1982. **21**(6): p. 401-410.
2. Ingold, K.U. and G.A. Russell, *Free Radicals*. 1973. 67ff.
3. Fischer, H., *Radical Reaction Rates in Liquids*. Vol. II/13. 1983.
4. Fossey, J., D. Lefort, and J. Sorba, Free Radicals in Organic Chemistry, 1993.

5. Voet, D. and J.G. Voet, *Biochemistry, 4th Edition*. 2010: John Wiley & Sons.
6. Berg, J.M., J.L. Tymoczko, and L. Stryer, *Biochemistry*. 2010: W. H. Freeman.
7. Tommos, C. and G.T. Babcock, *Proton and hydrogen currents in photosynthetic water oxidation.* Biochimica et Biophysica Acta (BBA) - Bioenergetics, 2000. **1458**(1): p. 199-219.
8. Mayer, J.M., *PROTON-COUPLED ELECTRON TRANSFER: A Reaction Chemist's View*. Annual Review of Physical Chemistry, 2004. **55**(1): p. 363-390.
9. Cukier, R.I. and D.G. Nocera, *PROTON-COUPLED ELECTRON TRANSFER.* Annual Review of Physical Chemistry, 1998. **49**(1): p. 337-369.
10. Rhile, I.J., et al., *Concerted Proton−Electron Transfer in the Oxidation of Hydrogen-Bonded Phenols.* Journal of the American Chemical Society, 2006. **128**(18): p. 6075-6088.
11. Markle, T.F. and J.M. Mayer, *Concerted Proton–Electron Transfer in Pyridylphenols: The Importance of the Hydrogen Bond.* Angewandte Chemie International Edition, 2008. **47**(4): p. 738-740.
12. Markle, T.F., et al., *Probing concerted proton–electron transfer in phenol–imidazoles.* Proceedings of the National Academy of Sciences, 2008.
13. Westlake, B.C., et al., *Concerted electron-proton transfer in the optical excitation of hydrogen-bonded dyes.* Proceedings of the National Academy of Sciences, 2011. **108**(21): p. 8554-8558.
14. Kühne, H. and G.W. Brudvig, *Proton-Coupled Electron Transfer Involving Tyrosine Z in Photosystem II†.* The Journal of Physical Chemistry B, 2002. **106**(33): p. 8189-8196.
15. Faller, P., et al., *Resolving intermediates in biological proton-coupled electron transfer: A tyrosyl radical prior to proton movement.* Proceedings of the National Academy of Sciences, 2003. **100**(15): p. 8732-8735.
16. Siegbahn, P.E.M., *Structures and Energetics for O2 Formation in Photosystem II.* Accounts of Chemical Research, 2009. **42**(12): p. 1871-1880.
17. Sjödin, M., et al., *The mechanism for proton-coupled electron transfer from tyrosine in a model complex and comparisons with Y(Z) oxidation in photosystem II.* Philosophical Transactions of the Royal Society B: Biological Sciences, 2002. **357**(1426): p. 1471-1511.
18. Mayer, J.M., *Simple Marcus-Theory-Type Model for Hydrogen-Atom Transfer/Proton-Coupled Electron Transfer.* The Journal of Physical Chemistry Letters, 2011. **2**(12): p. 1481-1489.
19. Neta, P., et al., *Solvent effects in the reactions of peroxyl radicals with organic reductants: evidence for proton-transfer-mediated electron transfer.* The Journal of Physical Chemistry, 1989. **93**(22): p. 7654-7659.
20. Barry, B.A., *Reaction dynamics and proton coupled electron transfer: Studies of tyrosine-based charge transfer in natural and biomimetic systems.* Biochimica et Biophysica Acta (BBA) - Bioenergetics, 2015. **1847**(1): p. 46-54.
21. Blair, D.F., et al., *Spectroelectrochemical study of cytochrome c oxidase: pH and temperature dependences of the cytochrome potentials. Characterization of site-site interactions.* Journal of Biological Chemistry, 1986. **261**(25): p. 11524-11537.
22. Kitagawa, T. and T. Ogura, *Oxygen Activation Mechanism at the Binuclear Site of Heme–Copper Oxidase Superfamily as Revealed by Time-Resolved Resonance Raman Spectroscopy*, in *Progress in Inorganic Chemistry*. 2007, John Wiley & Sons, Inc. p. 431-479.

23. Wikstrom, M., *Identification of the electron transfers in cytochrome oxidase that are coupled to proton-pumping.* Nature, 1989. **338**(6218): p. 776-778.
24. Gennis, R.B., *Multiple proton-conducting pathways in cytochrome oxidase and a proposed role for the active-site tyrosine.* Biochimica et Biophysica Acta (BBA) - Bioenergetics, 1998. **1365**(1–2): p. 241-248.
25. Malmstroem, B.G., *Vectorial chemistry in bioenergetics: cytochrome c oxidase as a redox-linked proton pump.* Accounts of Chemical Research, 1993. **26**(6): p. 332-338.
26. Cukier, R.I., *Mechanism for Proton-Coupled Electron-Transfer Reactions.* The Journal of Physical Chemistry, 1994. **98**(9): p. 2377-2381.
27. Schrauben, J.N., et al., *Multiple-Site Concerted Proton–Electron Transfer Reactions of Hydrogen-Bonded Phenols Are Nonadiabatic and Well Described by Semiclassical Marcus Theory.* Journal of the American Chemical Society, 2012. **134**(40): p. 16635-16645.
28. Hammes-Schiffer, S. and A.V. Soudackov, *Proton-Coupled Electron Transfer in Solution, Proteins, and Electrochemistry†.* The Journal of Physical Chemistry B, 2008. **112**(45): p. 14108-14123.
29. Soudackov, A., E. Hatcher, and S. Hammes-Schiffer, *Quantum and dynamical effects of proton donor-acceptor vibrational motion in nonadiabatic proton-coupled electron transfer reactions.* The Journal of Chemical Physics, 2005. **122**(1): p. 014505.
30. Fuller, F.D., et al., *Vibronic coherence in oxygenic photosynthesis.* Nat Chem, 2014. **6**(8): p. 706-711.
31. Novoderezhkin, V.I., E. Romero, and R. van Grondelle, *How exciton-vibrational coherences control charge separation in the photosystem II reaction center.* Physical Chemistry Chemical Physics, 2015.
32. Fayer, D., *Ultrafast Infrared And Raman Spectroscopy*. 2001: Taylor & Francis.
33. Huse, N., et al., *Vibrational Multilevel Quantum Coherence due to Anharmonic Couplings in Intermolecular Hydrogen Bonds.* Physical Review Letters, 2003. **91**(19): p. 197401.
34. Tokmakoff, A. and M.D. Fayer, *Infrared Photon Echo Experiments: Exploring Vibrational Dynamics in Liquids and Glasses.* Accounts of Chemical Research, 1995. **28**(11): p. 437-445.
35. Mukamel, S., *Principles of Nonlinear Optical Spectroscopy*. 1999: Oxford University Press.
36. Wright, J.C., *Multiresonant Coherent Multidimensional Spectroscopy.* Annual Review of Physical Chemistry, 2011. **62**(1): p. 209-230.
37. Sung, J. and R.J. Silbey, *Four wave mixing spectroscopy for a multilevel system.* The Journal of Chemical Physics, 2001. **115**(20): p. 9266-9287.
38. Fourkas, J.T., H. Kawashima, and K.A. Nelson, *Theory of nonlinear optical experiments with harmonic oscillators.* The Journal of Chemical Physics, 1995. **103**(11): p. 4393-4407.
39. Nitzan, A., *Chemical Dynamics in Condensed Phases: Relaxation, Transfer, and Reactions in Condensed Molecular Systems*. 2013: OUP Oxford.
40. Fourkas, J.T. and M.D. Fayer, *The transient grating: a holographic window to dynamic processes.* Accounts of Chemical Research, 1992. **25**(5): p. 227-233.
41. Tokmakoff, A., et al., *Vibrational spectral diffusion and population dynamics in a glass-forming liquid: Variable bandwidth picosecond infrared spectroscopy.* The Journal of Chemical Physics, 1995. **102**(10): p. 3919-3931.

42. Graener, H. and A. Laubereau, *Ultrafast overtone excitation for the study of vibrational population decay in liquids.* Chemical Physics Letters, 1983. **102**(1): p. 100-104.
43. Heyne, K., et al., *Coherent low-frequency motions of hydrogen bonded acetic acid dimers in the liquid phase.* The Journal of Chemical Physics, 2004. **121**(2): p. 902-913.
44. Yamaguchi, S., et al., *Vibrational dynamics of benzoic acid in nonpolar solvents studied by subpicosecond infrared pump–probe spectroscopy.* Chemical Physics Letters, 2008. **462**(4–6): p. 238-242.
45. Elsaesser, T., et al., *Ultrafast vibrational dynamics and anharmonic couplings of hydrogen-bonded dimers in solution.* Chemical Physics, 2007. **341**(1–3): p. 175-188.
46. Huse, N., et al., *Anharmonic Couplings Underlying the Ultrafast Vibrational Dynamics of Hydrogen Bonds in Liquids.* Physical Review Letters, 2005. **95**(14): p. 147402.
47. Rini, M., et al., *Femtosecond mid-infrared spectroscopy of condensed phase hydrogen-bonded systems as a probe of structural dynamics.* Faraday Discussions, 2003. **122**(0): p. 27-40.
48. Petersen, P.B., et al., *Ultrafast N−H Vibrational Dynamics of Cyclic Doubly Hydrogen-Bonded Homo- and Heterodimers.* The Journal of Physical Chemistry B, 2008. **112**(42): p. 13167-13171.
49. Gündoğdu, K., et al., *Relaxation and anharmonic couplings of the O–H stretching vibration of asymmetric strongly hydrogen-bonded complexes.* The Journal of Chemical Physics, 2007. **127**(4): p. 044501.
50. Dwyer, J.R., et al., *Ultrafast dynamics of vibrational N–H stretching excitations in the 7-azaindole dimer.* Chemical Physics Letters, 2006. **432**(1–3): p. 146-151.
51. Nicodemus, R.A., et al., *Collective Hydrogen Bond Reorganization in Water Studied with Temperature-Dependent Ultrafast Infrared Spectroscopy.* The Journal of Physical Chemistry B, 2011. **115**(18): p. 5604-5616.
52. Loparo, J.J., et al., *Reorientational and configurational fluctuations in water observed on molecular length scales.* Physical Review B, 2004. **70**(18): p. 180201.
53. Fecko, C.J., et al., *Ultrafast Hydrogen-Bond Dynamics in the Infrared Spectroscopy of Water.* Science, 2003. **301**(5640): p. 1698-1702.
54. Nibbering, E.T.J. and T. Elsaesser, *Ultrafast Vibrational Dynamics of Hydrogen Bonds in the Condensed Phase.* Chemical Reviews, 2004. **104**(4): p. 1887-1914.
55. Sando, G.M., Q. Zhong, and J.C. Owrutsky, *Vibrational and rotational dynamics of cyanoferrates in solution.* The Journal of Chemical Physics, 2004. **121**(5): p. 2158-2168.
56. Brookes, J.F., et al., *Effect of Solvent Polarity on the Vibrational Dephasing Dynamics of the Nitrosyl Stretch in an FeII Complex Revealed by 2D IR Spectroscopy.* The Journal of Physical Chemistry A, 2013. **117**(29): p. 6234-6243.
57. Asselin, M. and C. Sandorfy, *A low temperature infrared study of the band-width and frequency in self-associated alcohols.* Chem. Phys. Lett., 1971. **8**: p. 601.
58. Asselin, M. and C. Sandorfy, *Double Excitation in the Infrared Spectra of Self-Associated Alcohols.* The Journal of Chemical Physics, 1970. **52**(12): p. 6130-6134.
59. Lock, A.J. and H.J. Bakker, *Temperature dependence of vibrational relaxation in liquid H2O.* The Journal of Chemical Physics, 2002. **117**(4): p. 1708-1713.
60. Fuji, T. and T. Suzuki, *Generation of sub-two-cycle mid-infrared pulses by four-wave mixing through filamentation in air.* Optics Letters, 2007. **32**(22): p. 3330-3332 KW - Nonlinear optics, four-wave mixing KW - Infrared KW - Pulses UR - http://ol.osa.org/abstract.cfm?URI=ol-32-22-3330.

61. Cook, D.J. and R.M. Hochstrasser, *Intense terahertz pulses by four-wave rectification in air*. Optics Letters, 2000. **25**(16): p. 1210-1212 KW - Nonlinear optics, four-wave mixing KW - Infrared, far KW - Ultrafast nonlinear optics KW - Ultrafast technology UR - http://ol.osa.org/abstract.cfm?URI=ol-25-16-1210.
62. Petersen, P.B. and A. Tokmakoff, *Source for ultrafast continuum infrared and terahertz radiation.* Optics Letters, 2010. **35**(12): p. 1962-1964 KW - Nonlinear optics, four-wave mixing KW - Infrared KW - Ultrafast technology KW - Supercontinuum generation UR - http://ol.osa.org/abstract.cfm?URI=ol-35-12-1962.
63. Cheng, M., et al., *Generation of tunable octave-spanning mid-infrared pulses by filamentation in gas media.* Optics Letters, 2012. **37**(11): p. 1787-1789 KW - Ultrafast nonlinear optics KW - Spectroscopy, infrared KW - Pulses KW - Ultrafast phenomena UR - http://ol.osa.org/abstract.cfm?URI=ol-37-11-1787.
64. Chou, P.-T., et al., *Excited-State Intramolecular Proton Transfer in 10-Hydroxybenzo[h]quinoline.* The Journal of Physical Chemistry A, 2001. **105**(10): p. 1731-1740.
65. Frisch, M.J., et al., *Gaussian 09*. 2009, Gaussian, Inc.: Wallingford, CT, USA.

CHAPTER 2

Experimental Design, Implementation, and Analysis

2.1 Ultrafast Pump-probe studies

Understanding the potential energy surface of molecular systems is incredibly important to understanding energy transfer pathways and molecular dynamics in complex systems such as photosynthesis [1, 2]. In the molecular systems explored in this dissertation, many of the systems are influenced by strong intra-molecular hydrogen bonding which gives rise to broad lineshapes in infrared (IR) spectra and is difficult to decipher. Nonlinear ultrafast infrared spectroscopy offers a window into these dynamics by allowing direct examination of molecular dynamics through vibrational motions [3]. Here the experimental design, implementation, and analysis of a conventional mid-IR pump-broadband IR probe experiment is explored. By employing the methods described in the ensuing sections, a pump-probe experiment that examines the broad line-shapes associated with strong intra-molecular hydrogen-bonding systems can be realized. In this chapter, generation of the conventional mid-IR for the pump field is discussed in Section 2 followed by the development of the broadband IR (BBIR) source for the probe field in Section 3. The implementation of the BBIR and optical layout for the pump-probe studies are discussed in Sections 4 and 5, respectively. The analysis of the pump-probe data and DFT calculations used for modeling the systems discussed in Chapters 3 and 4 are discussed in Sections 6 and 7, respectively.

2.2 Generation of mid-IR Pump-field

The experiments discussed in this dissertation were performed using a commercially available 1 kHz Spectra-Physics Spitfire Ti:sapphire Laser system. The infrared pump-field was

generated by difference frequency generation (DFG) by an in-house built optical parametric amplifier (OPA). Here the 800 nm light generated by the Spitfire Laser was down-converted into a signal and idler beam in the near-IR regime. The near-IR signal and idler beam are then nonlinearly mixed in an 0.5 mm type II $AgGaS_2$ crystal to generate a pump-field between 2000-2800 cm^{-1} depending on the system of interest (see Figure 2.2.1) [4, 5].

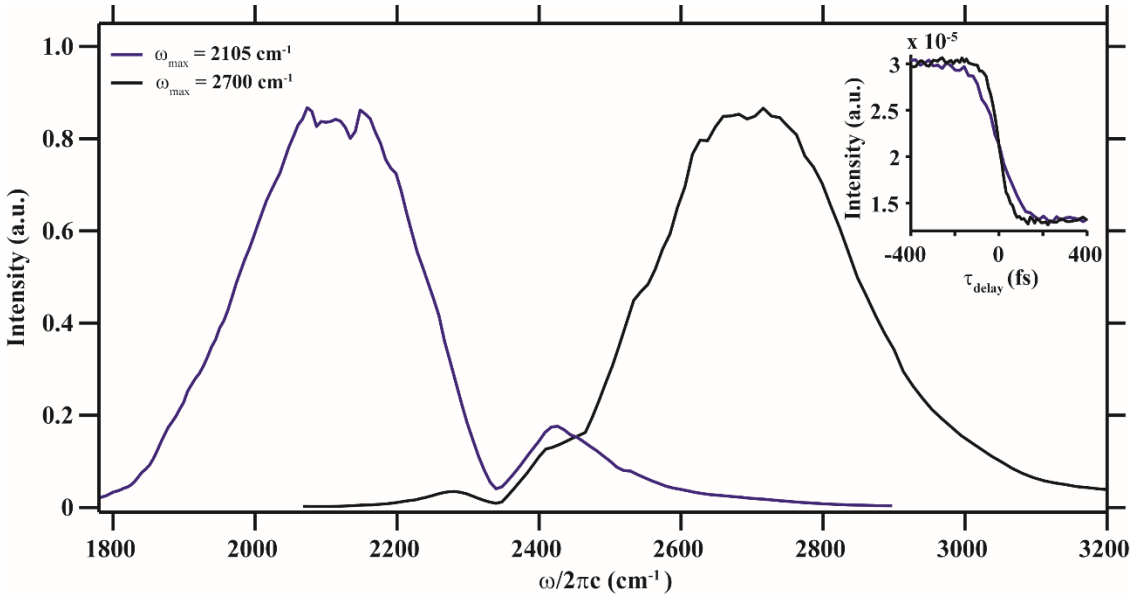

Figure 2.2.1: Normalized spectra of the mid-IR generated by the OPA-DFG. The OPA-DFG has been tuned to generate mid-IR at 2105 cm^{-1} in blue and 2700 cm^{-1} in black. Each spectrum was fit with a Gaussian function to determine the central frequency and bandwidth. For the spectrum tuned to 2105 cm^{-1} the bandwidth was 315 cm^{-1}. The mid-IR tuned to 2700 cm^{-1} had a bandwidth of 330 cm^{-1}. Inset is of an intensity cross correlation measurement of both mid-IR fields with a 35 fs 800 nm pulse in a 500 μm silicon wafer. The blue trace is the cross-correlation of the mid-IR centered at 2105 wavenumbers yielding in a pulse width of 103 fs. The black traces is the intensity cross correlation measurement of the mid-IR centered at 2700 cm^{-1} yielding a pulse width of 60 fs.

The crystal was tuned prior to each experiment to insure optimal bandwidth and overlap with the fundamental vibrational mode. For the red-shifted spectrum associated with the OD stretching mode (ν_{OD}) the spectrum was generally centered at 2100 wavenumbers as shown by the blue spectrum in Figure 2.2.1. The black spectrum in Figure 2.2.1 centered at 2700 wavenumbers was used for the pump-probe experiments on the OH stretching mode (ν_{OH}). Cross-correlations between the pump-field and a 35 fs 800 nm light source were collected in a 0.5 mm silicon wafer.

The 800 nm light was characterized by spectral phase interferometry for direct-electric field reconstruction (SPIDER)[6] to gather information about the temporal character of the 800 nm prior to the cross-correlation measurements. The resulting trace was fit with a sigmoidal function where τ in Equation 2.2.1 half of the pulse-width (see Figure 2.2.1).

$$y = \frac{A}{(1+\exp\{(t-t_0)/\tau\}} \tag{2.2.1}$$

The term t_0 represent the time at which both pulses are optimally overlapped temporally in the silicon wafer and A is the amplitude of the sigmoid curve. Intensity cross correlations were collected and characterized prior to each experiment yielding pulse widths at half max of ~100 fs and ~60 fs for the ν_{OD} and ν_{OH} experiments, respectively (see Figure 2.2.1).

2.3 Development of a broadband IR source for the probe

An alternative broadband mid-IR (BBIR) source was used for the probe beam which we have previously characterized [7]. Briefly, 800 nm light is passed through a type-I β-barium borate (BBO) crystal for second harmonic generation resulting in two collinear beams of the fundamental (ω) and second harmonic, 400 nm (2ω). The second harmonic is adjusted to overlap temporally using a calcite crystal. Due to the difference in refractive indices for the fundamental and overtone, slight angle changes of the crystal are able to account for the temporal mismatch introduced by the BBO crystal. The polarization mismatch between the fundamental and overtone are corrected using a birefringent wave plate that is a half-wave plate for the fundamental and full-wave plate for the second harmonic. Effectively, the wave plate allows independent polarization adjustment of the fundamental relative to the overtone. The result of this optical process yields a temporally and polarization matched fundamental and second harmonic that are collinearly aligned. These

fields are focused into a 1.5 m gas cell containing compressed air. The generated mid-IR is re-collimated with a matching concave mirror and separated from the remaining visible light by a 500 mm silicon wafer placed at Brewster's angle (see Figure 2.3.1).

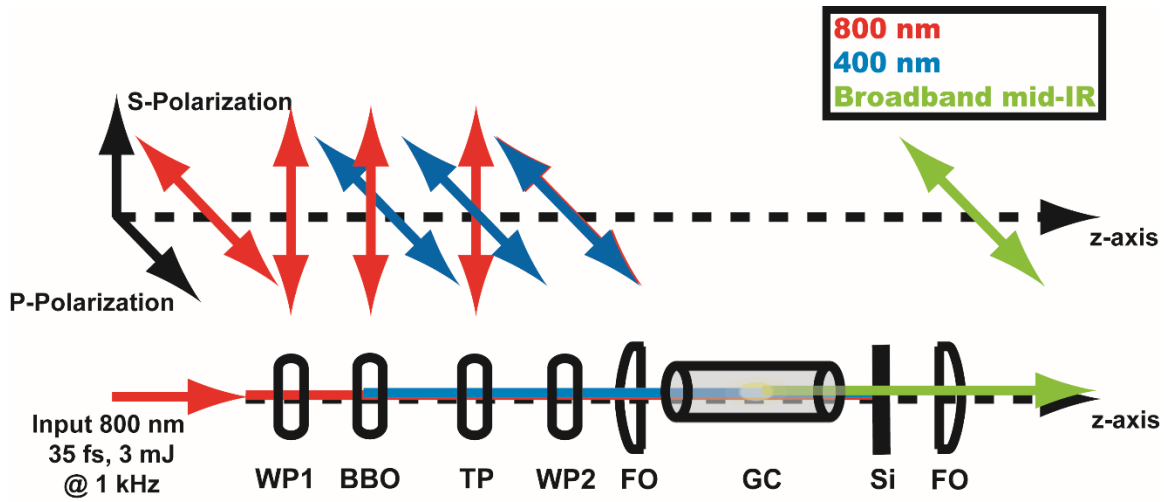

Figure 2.3.1: The experimental setup for broadband mid-IR generation. The abbreviations are: HWP-1, half-wave plate λ/2@800 nm; BBO, β-barium borate crystal (100 μm); CL, calcite crystal (1 mm); HWP-2, birefringent half-wave λ/2@800 nm + full-wave plate λ@400 nm; FO, concave mirror (f = 1.0 m); GC, gas cell (1.5 m in length); Si, silicon wafer (500 mm) placed at Brewster's angle.

The mid-IR generation is consistent with a four-wave mixing process based on the similar studies by Hochstrasser and co-workers and Tokmakoff and co-workers in addition to modeling of the data collected by Cheng and co-workers in our lab [8, 9].

By containing the mixing process within a closed gas cell, the gas media and pressure can be tuned to achieve desired spectral characteristics of the generated mid-IR. The tuneability of the mid-IR has been previously described by Cheng and co-workers. Briefly, decreasing the air pressure within the gas cell red-shifts the spectrum toward the spectral region containing the vibrational modes of interest, i.e. the hydroxyl/deuteroxyl stretch of the PCET model systems studied in Chapters 3 and 4. For the systems of interest the deuteroxyl stretch (ν_{OD}) is centered between 2000 and 2300 wavenumbers. Typically, this coincides with a pressure between 420 and

470 Torr which yields a spectrum centered at ~2300 cm^{-1} with a bandwidth of 1300 cm^{-1} as shown by the blue spectrum in Figure 2.3.2.

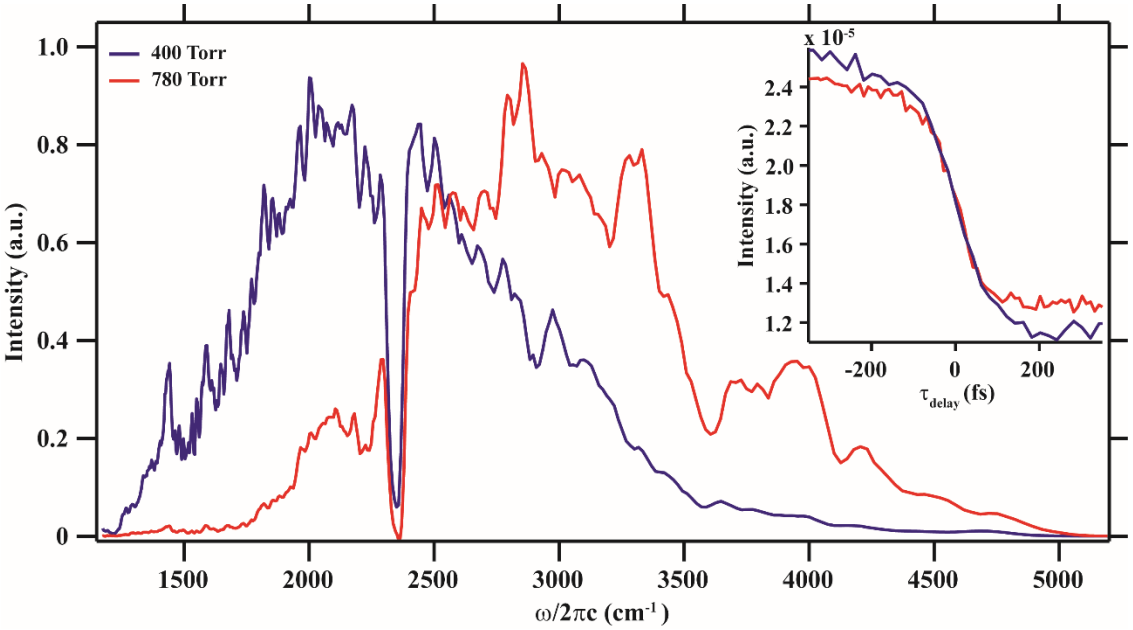

Figure 2.3.2: Normalized spectra of the BBIR. The two spectra are for the BBIR gas cell with air pressure set at 400 Torr in red and 780 Torr in blue. Each spectrum was fit with a Gaussian function to determine the central frequency and bandwidth. For the spectrum at 400 Torr the spectrum is centered at 2297 cm^{-1} with a bandwidth of 1285 cm^{-1}. The BBIR spectrum at 780 Torr is centered at 2980 cm^{-1} with a bandwidth of 1207 cm^{-1}. The spectrum at 400 Torr was multiplied by 5 to achieve a similar normalized intensity to the 780 Torr spectrum. Inset are the intensity cross correlation measurements of the BBIR at with 800 nm in a silicon wafer. The red cross correlation measurement in the inset of the 780 Torr spectrum resulted in a pulse width of 70 fs. The blue cross correlation in the inset of the 400 Torr spectrum resulted in a pulse width of 87 fs.

The red spectrum is the BBIR used for the equivalent hydroxyl stretch (ν_{OH}) is centered between 2500 and 2800 wavenumbers. For these experiments a pressure between 750 and 800 Torr was used which yields a spectrum centered at ~3000 cm^{-1} with a bandwidth of 1200 cm^{-1} (see Figure 2.3.2). The intensity of the BBIR is proportionally related to the pressure within the gas cell as indicated by previous studies by Cheng and co-workers. For this reason the pressure was chosen to obtain optimal spectral characteristics to encompass the vibrational mode of interest while also maintaining the maximum mid-IR intensity. For example having a lower pressure than 400 Torr may have the spectrum center better coincide with ν_{OD}=0→1 transition, however, the large

decrease in mid-IR intensity would have a significant impact on signal intensity and subsequent quality. The pressure was tuned prior to each experiment to insure optimal bandwidth and overlap with the fundamental and overtone of the vibrational mode.

The BBIR probe was temporally characterized by a cross-correlation with 800 nm light in a silicon wafer in the same manner as the pump-field mid-IR as described in Section 2. These cross correlations measurements resulted in a pulse width at half-max of 70 fs and 85 fs for the BBIR generated at 780 Torr and 400 Torr, respectively (Figure 2.3.2 inset). Additionally an intensity cross-correlation with the temporally characterized mid-IR pump-field were conducted in a 0.5 mm type I $AgGaS_2$ crystal prior to each experiment. Each trace was fit with a Gaussian function to determine the temporal window for pump-probe experiment (see Figure 2.3.3). The cross-correlation between the OPA-DFG generated mid-IR pump field tuned to 2105 cm^{-1} and the BBIR at 400 Torr resulted in a cross correlation measurement of 145 fs (see Figure 2.3.3). The red cross correlation, in Figure 2.3.3, between the OPA-DFG pump field tuned to 2700 wavenumbers and the BBIR at 780 Torr yielded a cross correlation measurement of 142 fs.

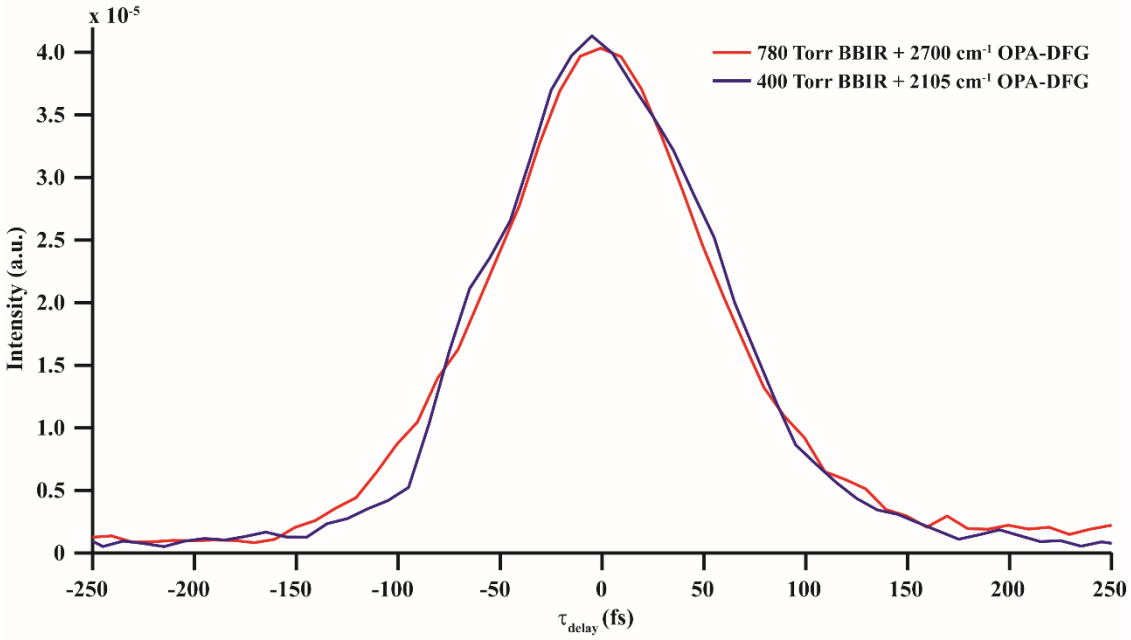

Figure 2.3.3: Cross-correlation measurements of the OPA-DFG mid-IR and BBIR in type I $AgGaS_2$. Each trace was fit with a Gaussian function to determine the cross correlation time. The blue trace is the cross correlation between the OPA-DFG mid-IR tuned to 2105 cm^{-1} and the BBIR at 400 Torr (spectrally centered at ~2300 cm^{-1}) resulting in a cross correlation time of 145 fs. The red trace is the cross correlation between the OPA-DFG mid-IR tuned to 2700 cm^{-1} and the BBIR at 780 Torr (spectrally centered at ~3000 cm^{-1}) resulting in a cross correlation time of 142 fs.

While these rudimentary measurements do gather information about the relative pulse duration of the BBIR, it does not reveal much information about the temporal character of the pulse envelope [10-15]. Previously collected cross-correlation frequency-resolved optical gating (XFROG) [11, 12, 15] measurements revealed a pulse width of 14.4 fs at 1000 Torr [7]. This is significantly different from the silicon cross-correlation measurement of 40 fs. Thus frequency dispersed measurements were collected of the BBIR and 800 nm cross-correlation in silicon as shown in Figure 2.3.4.

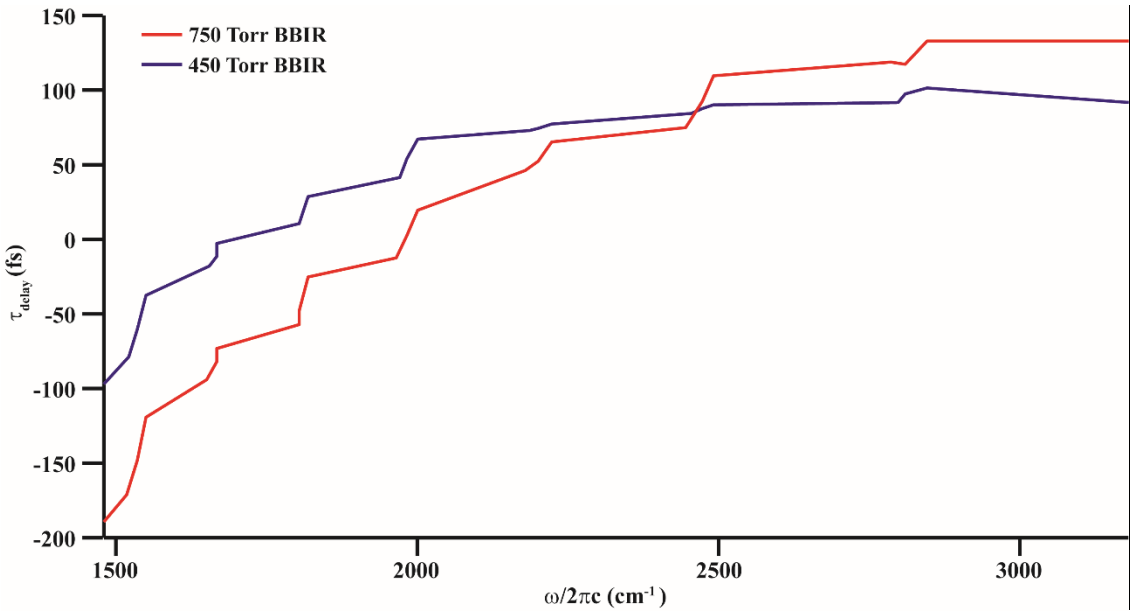

Figure 2.3.4: Dispersed intensity cross-correlation measurements of the BBIR and a 35 fs 800 nm light source in silicon wafer. The red trace of the BBIR at 750 Torr indicates a total temporal delay of 303 fs between 1500 and 3000 cm^{-1}. The blue trace of the BBIR at 450 Torr indicates a total temporal delay of 180 fs between 1500 and 3000 cm^{-1}.

While we have not utilized highly resolved pulse characterization methods such as the XFROG[12] to characterize the temporal structure of the BBIR, the dispersed measurements do reveal some information about the group velocity dispersion such as 180 fs delay between the 1500 and 3000 wavenumbers of the BBIR at 450 Torr (see Figure 2.3.4). The dispersion was not addressed prior to the experiments discussed in Chapters 3 or 4, however, the pulse-widths associated with frequency component was measured to be ~40 fs which is the limit of this characterization method as this coincides with the pulse width of the 800 nm field used for this cross-correlation. Furthermore, the delay between the blue-edge of the fundamental transition ($\nu = 0 \rightarrow 1$) and red-edge of the overtone transition ($\nu = 1 \rightarrow 2$) discussed in Chapters 3 and 4 was ~100 fs for the BBIR tuned to the ν_{OD} spectral region and ~110 fs for the BBIR tuned to the ν_{OH} spectral region.

2.4 Implementation of the BBIR for the probe of the pump-probe experiment

In nonlinear ultrafast pump-probe IR spectroscopy two coherent beams of mid-IR light were focused on to the sample as shown in Figure 2.4.1.

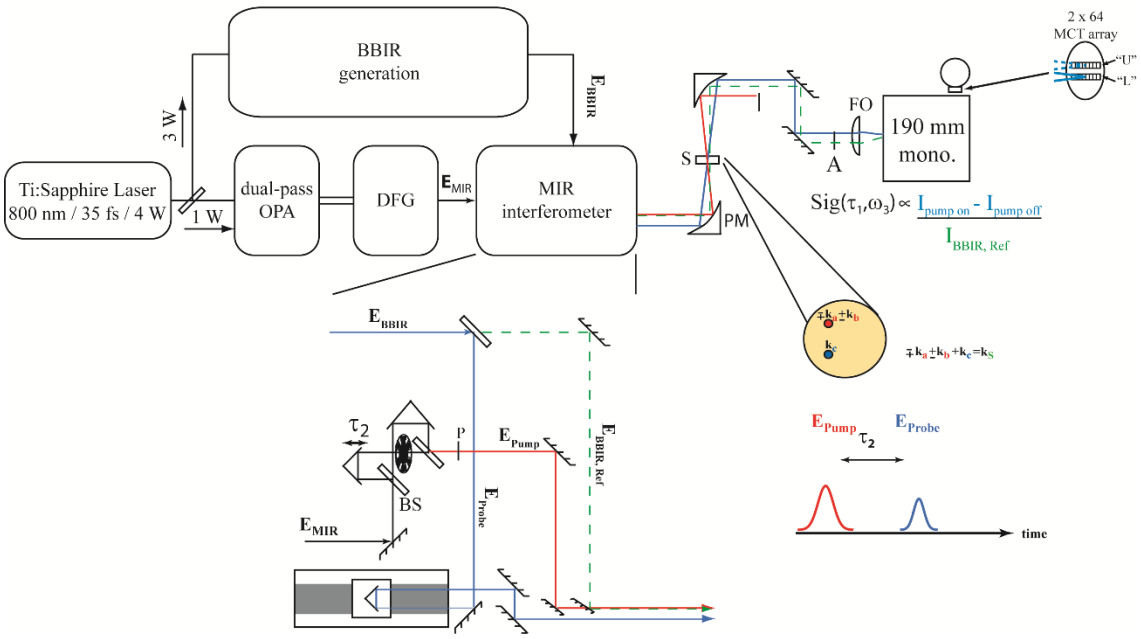

Figure 2.4.1: Schematic of the optics table layout. The layout shows the implementation of mid-IR light generated by the OPA-DFG (dual-pass OPA and DFG) and BBIR methods for pump-probe experiments. The mid-IR generated by the OPA-DFG process is directed into the mid-IR interferometer (MIR interferometer) where the time delay (t_2) between it and the BBIR is controlled by a mechanical stage. The delayed pulse is chopped to 500 Hz to achieve the pump on and pump off signals, and the polarization (P) is controlled using an MgF_2 half-wave plate and ZnSe wire-grid polarizer to achieve ZZZZ and ZZYY measurements. The generated BBIR is directed into mid-IR interferometer onto a long delay stage. This stage is designed around implementing the BBIR with the OPA-DFG mid-IR in a two dimensional (2D) IR experiment. This experiment has not been fully realized at this time and is beyond the scope of this work. The OPA-DFG mid-IR pump and BBIR probe are then directed to an off-axis parabolic mirror (PM) which focuses the pump and probe on a static sample S. The signal as a function of delay τ_2 and detection frequency ω_3 , $Sig(\tau_2,\omega_3)$, and co-propagating probe fields are recollimated by a matching PM and directed to the 190 mm monochromator (mono.) wherein a grating disperses the signal onto the upper stripe ("U") of the two stripe HgCdTe array detector (2x64 MCT array) with 64 bits per stripe. A reference BBIR beam is directed through the sample and subsequently onto the lower stripe ("L") of the array detector. An analyzer (A) maintains a polarization clean signal is focused (FO) into the array detector for the both the signal and reference fields. As indicated by the vectors $\mathbf{k_a}$, $\mathbf{k_b}$, $\mathbf{k_c}$, and $\mathbf{k_s}$ for the three light-matter interactions, the electric fields for the pump ($\mathbf{k_a}$ and $\mathbf{k_b}$) and probe ($\mathbf{k_c}$) are aligned in the $\mathbf{k_s} = \mathbf{k_a} - \mathbf{k_b} + \mathbf{k_c}$ phase matching condition. The signal field, $\mathbf{k_s}$, is co-propagating with probe field as a result of this alignment.

For this experiment ~0.1 μJ of IR beam was split off for the probe ($\mathbf{E_{Probe}}$) and held stationary. The pump beam ($\mathbf{E_{Pump}}$), ~0.35 μJ, was passed through an optical delay line to produce the waiting time τ_2. Both beams were focused in the sample area using an uncoated gold off-axis parabolic

mirror resulting in a FWHM spot-size of 190 μm ($1/e^2$). The home-built sample cell uses two 1 mm CaF_2 windows separated by a 200 μm thick Teflon spacer. The probe beam was recollimated after the sample with a matched off-axis parabolic mirror. The signal was collected in both parallel (ZZZZ) and crossed (ZZYY) polarizations to the input beams. The polarization of the pump was controlled by a MgF_2 tunable half-waveplate and a ZnSe wire-grid polarizer. The polarization of the probe field is held static. The intensity changes ($I = |\mathbf{E}|^2$) are measured using a 190 mm monochromator (Triax 190, Horiba Jobin Yvon) with a 75 mm^{-1} grating which disperses the signal onto a 2 × 64 pixel HgCdTe (MCT) array detector (See Figure 2.4.1) [16, 17]. The probe field and overlapped signal field were collected on the upper stripe ("U") on the MCT array detector. Additionally, a small portion of the BBIR beam was split from the original prior to focusing into the sample for reference $\mathbf{E}_{\mathbf{BBIR,Ref}}$ purposes. The reference field was routed such that the probe and reference were temporally mismatched by 2 ns delay in addition to spatial misalignment in the sample to minimize vibrational excitation and sample heating affects. The pump beam was chopped at 500 Hz prior to the first focusing onto the sample for signal collection. This chopping scheme allows for probe field interaction $I_{Pump\text{-}off}$ to be subtracted from signal and co-propagating probe fields $I_{Pump\text{-}on}$ resulting in the desired signal. The reference field was collected on the lower stripe ("L") of the MCT array detector shown in Figure 2.4.1. The reference field allows for greater signal quality by dividing out the probe field from signal on a shot-by-shot basis as this removes fluctuations in the probe field as they occur. The pump-probe data (transient absorption measurements) were collected by obtaining the difference between the pump on and pump off on a shot-by-shot basis for increased signal-to-noise ratio [18, 19].

2.5 Initial Workup of BBIR Pump-probe data

The many advantages of using a broadband IR source for nonlinear photophysical experiments also come with many complexities. The most notable is the initial post-collection data processing. As previously indicated in Section 4, the acquisition of the IR probe is collected by spectrally dispersing the BBIR probe-field on a 64 pixel array using a 75 mm^{-1} grating (see Figure 2.4.1). While this grating choice allows greater bandwidth collection over the array at the cost of frequency resolution, generally the bandwidth of the line-shapes for the PCET molecules of interest is greater than the total capability at a single grating position. Thus data is collected over several grating positions during the course of the experiment which may exceed 6 or 7 positions. Therefore each grating position must be combined at the corresponding delay times to form a full spectrum at a given pump field delay. The separation of the grating positions is chosen to allow minimum pixel overlap while having enough overlap that piecing the grating positions together allows for bad pixels, slight misalignment, and incongruent signal behavior. For the experiments discussed here, generally 28 pixels of overlap are utilized to achieve optimal signal quality.

The piece-wise joining of the grating positions is carried out in three phases. (1) Build the frequency axis and determine initial piece-wise joining positions (refer to Appendices A.1 and A.2 for MATLAB code). (2) Join data piece-wise based on first step while examining for spectral disparities from FTIR spectrum (refer to Appendix A.3 for MATLAB code). (3) Re-iterate first two steps to achieve satisfactory spectrum with minimum disparities. This method relies on objective data joining based on pixel overlap and grating position as well as subjective eye-test comparison to expected absorption spectra.

2.6 Pump-probe Data Analysis

The pump-probe studies were analyzed to gather information about the anharmonicities, vibrational lifetimes, and low frequency modes coupled to the vibrational mode of interest. For the pump-probe studies discussed in this article negative peak correlates with a ground state bleach and is centered at the peak of the FTIR transition. Similarly the positive peak is associated with an excited state absorption and is centered at the transition from the ν=1 to the ν=2 state. The ground state bleach and excited state absorption were fit at τ_2 = 0 fs with a Gaussian function of floating width to obtain the central frequency for the fundamental and the overtone transition of each mode. The anharmonicities were calculated by determining the difference between the fundamental and overtone of the vibrational mode(s). The isotropic response was calculated following the argument shown in Equation 2.6.1 from the ZZZZ and ZZYY polarization data [20].

$$S_{ISO} = \frac{S_{ZZZZ} - 2S_{ZZYY}}{3} \tag{2.2.2}$$

The reorganizational motions associated with molecular rotations have been removed in the isotropic response allowing for a more accurate portrayal of the vibrational population dynamics [20]. Depending on the dynamics exhibited by the isotropic pump-probe trace, each trace was fit with two exponential decays starting at 110 fs to extract information about the population dynamics. Residuals of the pump-probe measurements were calculated by subtracting exponential fits from the original data. A Nuttall apodization function is applied to residual to more heavily weight the initial 1 – 2 ps, depending on the length of any oscillatory comonents, and remove any oscillatory components remaining latter in the scan where the number of time-points is no longer in accordance with Nyquist rate (refer to Appendix A.4 for the MATLAB code for the apodization function) for a vibrational oscillation having a period between 110 and 280 fs. A Fast Fourier-

Transform (FFT) was performed on the residuals to investigate the low frequency modulations resulting in an intensity spectrum of the low frequency modes coupled to the high frequency vibrational mode.

2.7 Modeling by DFT calculations

Density functional theory (DFT) calculations of the equilibrium structure in the gas phase and IR spectra of DOAr-Py, DOAr-ND_2, HBQ, and DBQ were conducted in Gaussian 09C[21] using the B3LYP/6-311++G(d,p) functional and basis set. In addition to frequency calculations, anharmonic calculations were conducted to examine coupling constants of the cubic and quartic interaction terms. The integration grid for the anharmonic calculations was altered from default parameters to 99 radial points and 610 angular points for the DOAr-Py complex. For the DOAr-ND_2, HBQ, and DBQ systems the integration grid was set to 150 radial points and 770 angular points to insure accuracy of the optimized structure and anharmonic mode calculations [22] (refer to Appendix A.5 for Gaussian09C input file). The anharmonic frequency correction values for the DOAr-ND_2 generally resulted in imaginary frequencies when carried out using a similar grid to the DOAr-Py. This is likely due to the lack of rigidity for the DOAr-ND_2 complex while marginal changes were observed for the HBQ and DBQ systems between the lower and higher resolution integration methods. As noted by Barone, the accuracy of the optimized structure before these calculations is of utmost importance. For this reason, the optimization was very tight with tight symmetry tolerance (C2). Additionally, the appropriate scaling factor of 0.968 was applied to the frequency calculations as indicated by Truhlar and co-workers for the 6-311 basis set used for these calculations [23].

References

1. Wright, J.C., *Multiresonant Coherent Multidimensional Spectroscopy.* Annual Review of Physical Chemistry, 2011. **62**(1): p. 209-230.
2. Sundström, V., *Femtobiology.* Annual Review of Physical Chemistry, 2008. **59**(1): p. 53-77.
3. Sung, J. and R.J. Silbey, *Four wave mixing spectroscopy for a multilevel system.* The Journal of Chemical Physics, 2001. **115**(20): p. 9266-9287.
4. Elsaesser, T., H. Lobentanzer, and A. Seilmeier, *Generation of tunable picosecond pulses in the medium infrared by down-conversion in AgGaS2.* Optics Communications, 1985. **52**(5): p. 355-359.
5. Cerullo, G. and S. De Silvestri, *Ultrafast optical parametric amplifiers.* Review of Scientific Instruments, 2003. **74**(1): p. 1-18.
6. Iaconis, C. and I.A. Walmsley, *Spectral phase interferometry for direct electric-field reconstruction of ultrashort optical pulses.* Optics Letters, 1998. **23**(10): p. 792-794.
7. Cheng, M., et al., *Generation of tunable octave-spanning mid-infrared pulses by filamentation in gas media.* Optics Letters, 2012. **37**(11): p. 1787-1789 KW - Ultrafast nonlinear optics KW - Spectroscopy, infrared KW - Pulses KW - Ultrafast phenomena UR - http://ol.osa.org/abstract.cfm?URI=ol-37-11-1787.
8. Petersen, P.B. and A. Tokmakoff, *Source for ultrafast continuum infrared and terahertz radiation.* Optics Letters, 2010. **35**(12): p. 1962-1964 KW - Nonlinear optics, four-wave mixing KW - Infrared KW - Ultrafast technology KW - Supercontinuum generation UR - http://ol.osa.org/abstract.cfm?URI=ol-35-12-1962.
9. Cook, D.J. and R.M. Hochstrasser, *Intense terahertz pulses by four-wave rectification in air.* Optics Letters, 2000. **25**(16): p. 1210-1212 KW - Nonlinear optics, four-wave mixing KW - Infrared, far KW - Ultrafast nonlinear optics KW - Ultrafast technology UR - http://ol.osa.org/abstract.cfm?URI=ol-25-16-1210.
10. Backus, S., et al., *High power ultrafast lasers.* Review of Scientific Instruments, 1998. **69**(3): p. 1207-1223.
11. Linden, S., H. Giessen, and J. Kuhl, *XFROG — A New Method for Amplitude and Phase Characterization of Weak Ultrashort Pulses.* physica status solidi (b), 1998. **206**(1): p. 119-124.
12. Kane, D.J. and R. Trebino, *Characterization of arbitrary femtosecond pulses using frequency-resolved optical gating.* Quantum Electronics, IEEE Journal of, 1993. **29**(2): p. 571-579.
13. Lee, K.F., et al., *Characterization of mid-infrared femtosecond pulses [Invited]*. Journal of the Optical Society of America B, 2008. **25**(6): p. A54-A62.
14. Chilla, J.L.A. and O.E. Martinez, *Direct determination of the amplitude and the phase of femtosecond light pulses.* Optics Letters, 1991. **16**(1): p. 39-41.
15. Yabushita, A., T. Fuji, and T. Kobayashi, *SHG FROG and XFROG methods for phase/intensity characterization of pulses propagated through an absorptive optical medium.* Optics Communications, 2001. **198**(1–3): p. 227-232.
16. Brookes, J.F., et al., *Effect of Solvent Polarity on the Vibrational Dephasing Dynamics of the Nitrosyl Stretch in an FeII Complex Revealed by 2D IR Spectroscopy.* The Journal of Physical Chemistry A, 2013. **117**(29): p. 6234-6243.

17. Lynch, M.S., et al., *Coherent Fifth-Order Visible–Infrared Spectroscopies: Ultrafast Nonequilibrium Vibrational Dynamics in Solution.* The Journal of Physical Chemistry A, 2012. **116**(26): p. 7023-7032.
18. Tokmakoff, A., B. Sauter, and M.D. Fayer, *Temperature-dependent vibrational relaxation in polyatomic liquids: Picosecond infrared pump–probe experiments.* The Journal of Chemical Physics, 1994. **100**(12): p. 9035-9043.
19. Heyne, K., et al., J. Chem. Phys., 2004. **121**: p. 902.
20. Nicodemus, R.A., et al., *Collective Hydrogen Bond Reorganization in Water Studied with Temperature-Dependent Ultrafast Infrared Spectroscopy.* The Journal of Physical Chemistry B, 2011. **115**(18): p. 5604-5616.
21. Frisch, M.J., et al., *Gaussian 09*. 2009, Gaussian, Inc.: Wallingford, CT, USA.
22. Barone, V., *Vibrational zero-point energies and thermodynamic functions beyond the harmonic approximation.* The Journal of Chemical Physics, 2004. **120**(7): p. 3059-3065.
23. Alecu, I.M., et al., *Computational Thermochemistry: Scale Factor Databases and Scale Factors for Vibrational Frequencies Obtained from Electronic Model Chemistries.* Journal of Chemical Theory and Computation, 2010. **6**(9): p. 2872-2887.

CHAPTER 3

Polarization Selective Femtosecond Infrared Pump-probe studies on DOAr-Py and DOAr-ND_2

3.1 DOAr-Py and DOAr-ND_2: Model Systems for PCET Reactions

Intra-molecular hydrogen-bonds play a significant role in proton-coupled electron transfer (PCET) reactions, which are a ubiquitous phenomenon throughout chemistry. For example, the oxidation of the tyrosine residue in photosystem II (PS II) involves long chain electron transfer to pigment 680 (P_{680}^{+}) accompanied by the transfer of the phenolic proton to a hydrogen-bonded imidazole [1-9]. The two model systems; 3,5-di-*tert*-butyl-2-hydroxy-phenylpyridine (DOAr-Py) and C-(3,5-di-*tert*-butyl-2-hydroxyphenyl)-C,C-diphenylmethylamine (DOAr-ND_2); have significant similarities to the oxygen-evolving complex (OEC) in photosystem II where the oxidation of water occurs. The OD stretching vibration (ν_{OD}) is an excellent reporter of the hydrogen/deuteron bonding dynamics and was studied using spectrally dispersed infrared pump-probe spectroscopy. This study revealed that low frequency structural modulations at 120 cm^{-1} for DOAr-Py and 150 cm^{-1} for DOAr-ND_2 are anharmonically coupled to the ν_{OD} mode. In this chapter, previous studies on these systems are discussed in Section 2 followed by the experimental layout and results for DOAr-Py in Section 3 and 4, respectively. The experimental details for the studies of DOAr-ND_2 are discussed in Section 5, followed by the results in Section 6. Concluding remarks for both studies can be found in Section 7.

3.2 Previous work on DOAr-Py and DOAr-ND2

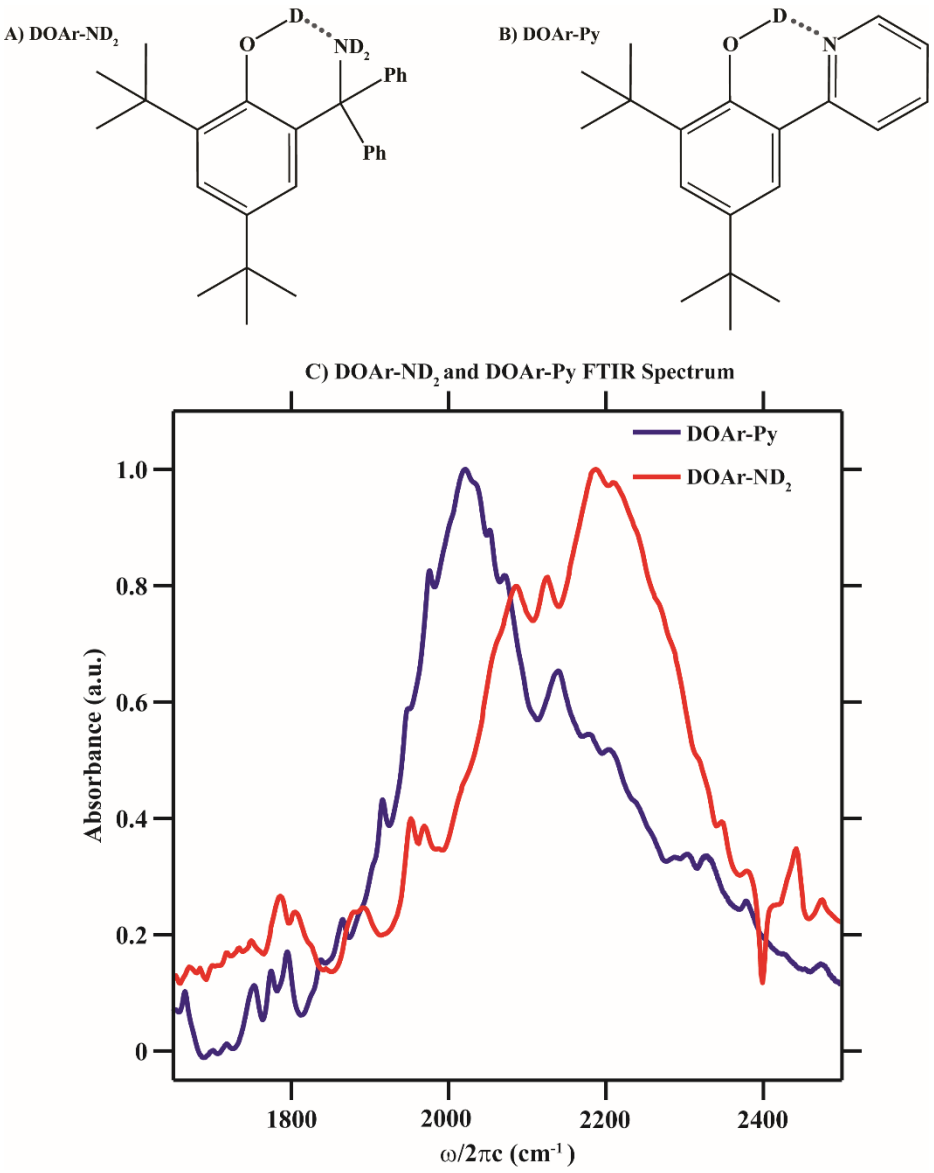

Figure 3.2.1: Molecular structures and normalized FTIR of PCET model systems DOAr-Py and DOAr-ND2. **A** and **B)** Molecular structures of DOAr-ND2 and DOAr-Py, respectively. These model systems mimic the OEC in the photosystem II where the charge transfer for the oxidation of water is driven by the hydrogen bonding of the phenolic proton of tyrosine to a nearby imidazole of histidine.[4] For the systems studied here imidazole was changed to a pyridine (DOAr-Py) or an amine (DOAr-ND2). **C)** Normalized FTIR spectra of the DOAr-Py and DOAr-ND2 compounds in the range of interest. The solid red line is the spectrum of the 0.6 M DOAr-ND2 in $CHCl_3$ and the solid green line is the spectrum of the 0.7 M DOAr-Py in CCl_4. The pathlengths for these measurements where 100 μm as determined by a Teflon spacer.

Electrochemical studies have shown these complexes undergo concerted-proton coupled electron transfer and give credence for using nonadiabatic Marcus theory to describe the concerted proton-electron transfer [10-13]. Hammes-Schiffer *et al.* have shown fluctuations along the reaction coordinate are heavily reflected in the reorganizational energy and the quantum coupling of the electron and proton. The line-shapes of IR spectra shown in Figure 3.2.1A have significant structure for both DOAr-Py and DOAr-ND_2, which makes it difficult to decipher the underlying dynamics that give rise to the broad features and multiple peaks. Ultrafast pump-probe experiments allow us to determine how low frequency structural fluctuations affect intra-molecular hydrogen bonding and to examine anharmonic coupling of the ν_{OD} to low frequency modes. Understanding the effects of low frequency modes on fluctuations of the reaction coordinate will afford a window into the PCET reaction [14, 15].

Rhile and co-workers have conducted a battery of thermo-chemical studies to gather information in an attempt to describe the reaction mechanism for both HOAr-Py and HOAr-NH_2 [3, 11, 16]. Briefly, crystallographic studies of HOAr-Py have indicated an O···N distance of 2.567 ± 0.005 Å [2, 3]. Proton NMR studies on HOAr-Py have a chemical shift of 14.83 ppm[3] which is significantly shifted downfield due to "resonance-assisted hydrogen bonding" and is typical of low-barrier hydrogen bonding systems commonly characterized by PCET reactions [17]. Kinetic studies with $[Fe(bpy)_3]^{3+}$ have shown a fast constant of $(5.2 \pm 0.8) \times 10^6$ $M^{-1}s^{-1}$ for the oxidation of HOAr-Py in a single kinetic step. Crystallographic studies of HOAr-NH_2 have indicated an O···N distance of 2.588 ± 0.035 Å [2, 3]. Proton NMR studies on HOAr-NH_2 have a chemical shift of 12.32 ppm[3] which is similar to the NMR studies of HOAr-Py results mentioned previously [17]. Kinetic studies with $[Fe(bpy)_3]^{3+}$ have shown a fast constant of $(4 \pm 1) \times 10^6$ $M^{-1}s^{-1}$ for the oxidation of HOAr-NH_2 in a single kinetic step. From these results Rhile and co-workers conclude that the

proton transfer and electron transfer occur in one concerted step instead of separate chemical events.

3.3 Experimental Details for DOAr-Py Pump-probe studies

The synthesis of the HOAr-Py form of the sample was performed by Rhile and co-workers using the method described by Inoue and co-workers [3, 18]. The deuterated versions of HOAr-Py was studied to minimize interference from nearby alkyl and aromatic vibrational modes. Schrauben and co-workers conducted the H/D exchange less than one day in advance of experimental measurements to ensure a fully enriched sample. HOAr-Py was prepared in CCl_4 at a concentration of 0.6 M. The use of CCl_4 for the solvent minimizes interference from the solvent on the intra-molecular hydrogen bonding network which is our reporter on how structural modulations affect molecular dynamics and subsequent PCET [19]. The home-built sample cell uses two 1 mm CaF_2 windows separated by a 125 μm thick Teflon spacer. All FTIR spectra were obtained using a JASCO FT/IR-4100 spectrometer with 2 cm^{-1} resolution.

The experiments discussed in this article were performed using a commercially available 1 kHz Spectra-Physics Spitfire Ti:sapphire Laser (3W, 35 fs) system [20, 21]. The mid-IR light was generated by two-pass optical parametric amplifier (OPA-800C, Newport). Here the 800nm light generated by the Spitfire Laser was down-converted into a signal and idler beam in the near-IR regime. Near-IR signal and idler pulses from the OPA are spatially and temporally overlapped and undergo difference-frequency mixing in a 0.5 mm $AgGaS_2$ crystal to produce mid-IR pulses with spectral bandwidths greater than 230 cm^{-1} at center at ~2040 cm^{-1} as shown by the black spectrum in Figure 3.4.1 [22, 23]. Auto-correlations were collected and characterized before data collection giving pulse widths at half max of ~70 fs.

In nonlinear ultrafast pump-probe IR spectroscopy two coherent beams of mid-IR light were focused on to the sample, S, in a pump-probe geometry as shown in Figure 3.3.1.

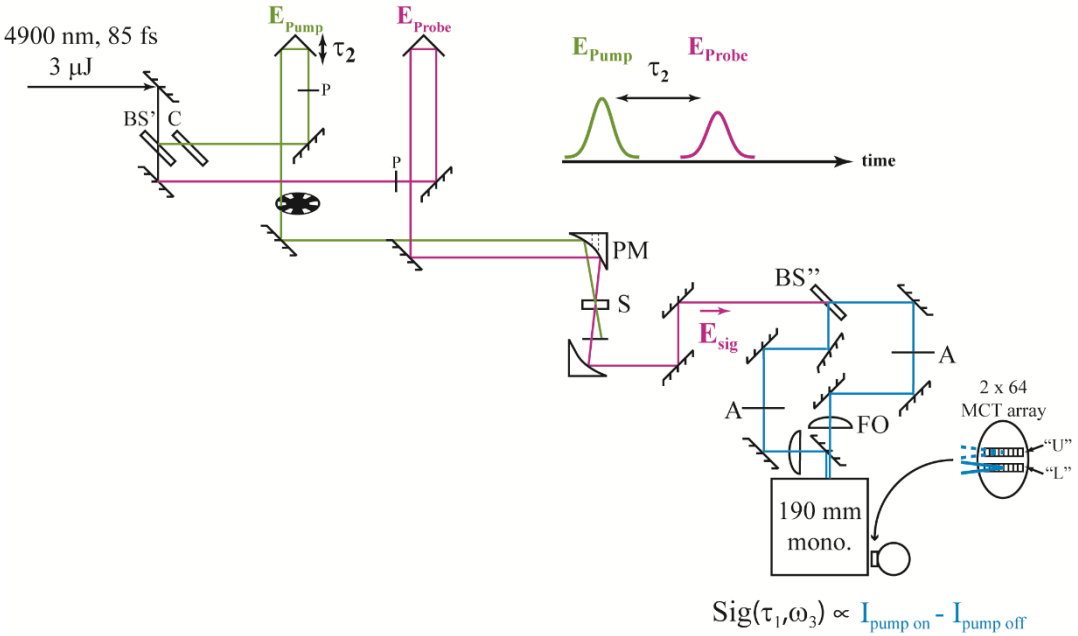

Figure 3.3.1: Schematic of the optics table layout. The layout shows the implementation of mid-IR light generated by the OPA-DFG (dual-pass OPA and DFG) for a pump-probe experiment. The mid-IR generated by the OPA-DFG process is directed into the mid-IR interferometer where the time delay (τ_2) between pump (E_{Pump}) and probe fields (E_{Probe}) is controlled by a mechanical stage. The delayed pulse is chopped to 500 Hz to achieve the pump-on ($I_{Pump\text{-}on}$) and pump-off ($I_{Pump\text{-}off}$) changes in intensity, and the polarization is controlled using polarization optics P (half-wave plate and polarizer pairing) to achieve ZZZZ polarization response for optimal signal intensity. The pump and probe fields are then directed to an off-axis parabolic mirror (PM) which focuses the pump and probe on a static sample S. The probe and overlapping signal as a function of detection frequency ω_3 and waiting time τ_2, $Sig(\tau_2,\omega_3)$, fields are recollimated by a matching PM and directed to the 190 mm monochromator (mono.) wherein a grating disperses the signal onto both stripes of an array detector (2x64 MCT detector) with 64 bits per stripe. An analyzer (A) maintains a polarization clean signal, which is focused (FO) into the array detector for the both the signal and reference fields.

For this experiment ~0.3 μJ of IR beam was split off for the probe field as shown in Figure 3.3.1 and held stationary. The pump field, ~0.6 μJ, was passed through an optical delay line to produce the waiting time τ_2. The probe beam was chopped at 500 Hz for signal collection (refer to Chapter 2 Section 4 for detail on chopping scheme). Both fields were focused in the sample area using an uncoated gold off-axis parabolic mirror resulting in a FWHM spot-size of 130 μm ($1/e^2$). The probe field was recollimated after the sample with a similar off-axis parabolic mirror. The polarization of the signal for the DOAr-Py was collected parallel (ZZZZ) to the input beams for

maximum response. The intensity changes are measured using a 190 mm monochromator (Triax 190, Horiba Jobin Yvon) with a 75 mm^{-1} grating which disperses the signal onto a 2 × 64 pixel HgCdTe array detector (see Figure 3.3.1). The pump-probe data (transient absorption measurements) were collected by obtaining the difference between the pump-on and pump-off intensity measurements [21, 24, 25]. The pump-probe traces were fit with two exponentials to extract information about the population dynamics starting at 140 fs. A Fourier transform of the residual that results from the subtraction of the fit from the data yields a spectrum containing low frequency modulations coupled to the high frequency ν_{OD} mode in the far-IR region. More details about the analysis can be found in Chapter 2 Section 6. DFT calculations were conducted on DOAr-Py to model this system. Details on the parameters for the DFT calculations can be found in Chapter 2 Section 7.

3.4 Pump-probe Results of DOAr-Py

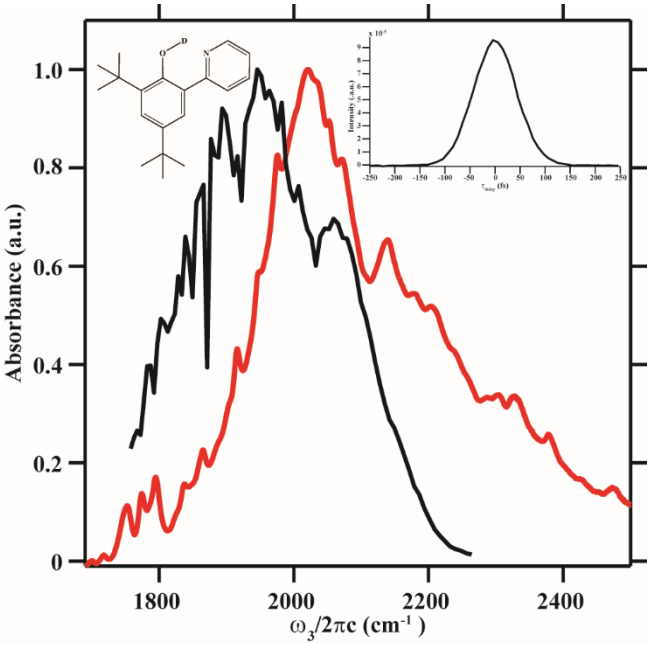

Figure 3.4.1: Normalized FTIR spectrum of the DOAr-Py compound in the range of interest in red. The solid black line is a spectrum of the mid-IR pump and probe fields. The upper right inset is of the DOAr-Py structure. The upper right inset is the trace from an intensity autocorrelation between the pump and probe field yielding a pulse width of 85 fs.

The FTIR spectra of the DOAr-Py sample shows a broad line shape centered in the 1650-2500 cm^{-1} range attributed to the ν_{OD} stretch (See Figure 3.4.1). As indicated in Figure 3.4.1, the mid-IR pump-field generated by the difference frequency generation does not contain enough spectral content to pump/probe the entire region of the ν_{OD} stretch. However, our mid-IR window allows us to monitor much of the dynamics of the fundamental ($\nu_{OD}=0\rightarrow1$) and overtone ($\nu_{OD}=1\rightarrow2$) region. The line-shape in this region has significant structure which makes it difficult to decipher the underlying dynamics which give rise to broad features and multiple peaks. The pump-probe measurements provide a window to view the dynamics in more detail.

The pump-probe spectra as a function of the detection frequency at various time delays is shown in Figure 3.4.2A. The bleach (negative peak) is centered at the peak of the IR transition and the excited state absorption (positive peak) is centered at the transition from the ν=1 to the ν=2 state. The fundamental and overtone peaks shown in Figure 3.4.2 at τ_2 = 0 fs were fit with a Gaussian function of floating width for the fundamental transition and the overtone transition of each local mode. For DOAr-Py the fundamental was determined to be 2033 cm^{-1} and the corresponding overtone 1825 cm^{-1}. The DOAr-Py complex exhibits a single broad OD mode in the FTIR spectrum which gives rise to an anharmonicity of 208 cm^{-1}. This anharmonicity value is within the 180 to 235 cm^{-1} region reported by Rospenk *et al.* for phenol•pyridine complexes in carbon tetrachloride [26]. Similar studies[27, 28] have shown that strong hydrogen bond formation increases the anharmonicity for the ν_{OD} stretch.

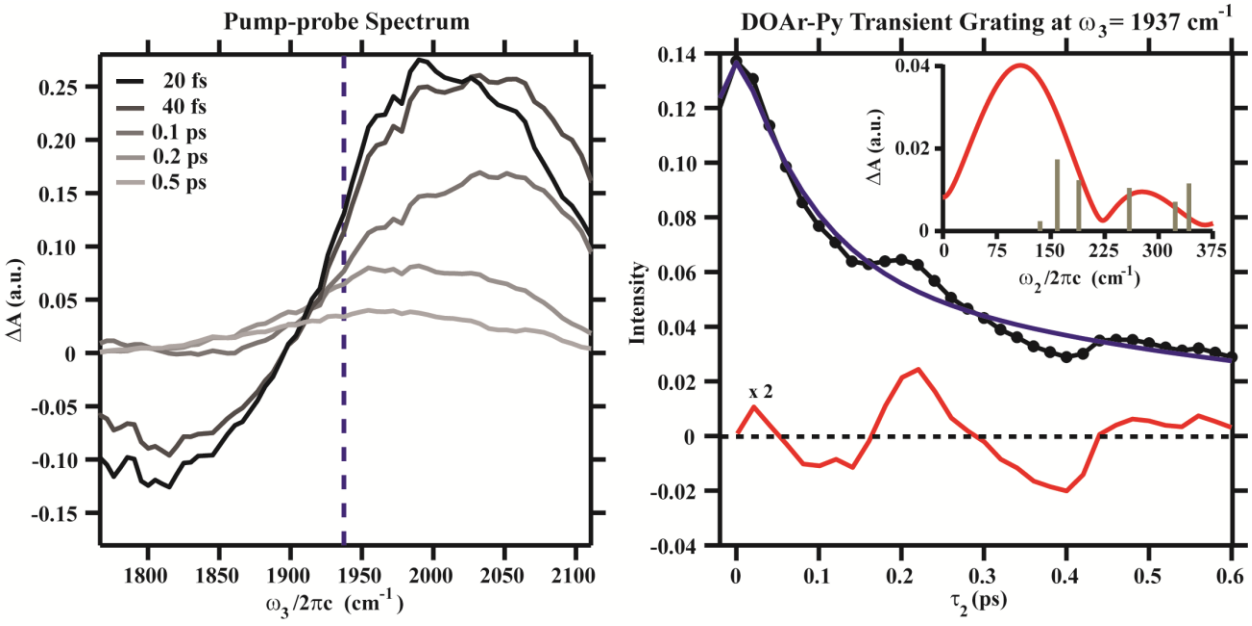

Figure 3.4.2: Pump-probe spectra of DOAr-Py at selected τ_2 points of 0, 40, 100, 200, and 500 fs. **B)** The pump-probe trace at 1937 cm^{-1} as indicated by the dashed-blue line in **A**. This trace was chosen as it has a strong oscillatory component near peak intensity. The blue-dashed line, black-solid line, and red-solid line in the pump-probe trace are the original data, exponential fit, and residual respectively. **C)** The spectral intensity calculated from the FFT of the residual in **B**. The grey sticks indicate harmonic frequency calculation (See Table 3.4.1).

The pump-probe measurement for DOAr-Py at the fundamental, 2033 cm^{-1}, was fit with a two exponentials of 88 fs and 383 fs. Additionally the trace at 1937 cm^{-1} is shown to demonstrate the oscillatory component which is prevalent among all of the traces (Figure 3.4.2B). Each of the traces were fit with a two exponential decays which reports a fast ν_{OD} relaxation by 51 fs and a longer decay of 740 fs. These two component decay rates are typical of strong hydrogen bonding systems such as those by the $\nu_{OH/OD}$ mode in D_2O/HOD vibrational relaxation experiments as attributed by Bakker and co-workers and Tokmakoff and co-workers in addition to many others [29-35]. The spectrum from the FT of the residual shown in Figure 3.4.2C for DOAr-Py shows a low frequency mode at 120 cm^{-1}. Furthermore, previous studies have measured the low frequency solvent modes of CCl_4 at 218, 315, and 464 cm^{-1}; indicating the low frequency mode shown here is not a result of the solvent [36, 37]. Additionally, the blue end (>2000 cm^{-1}) of the spectra appears

to grow in during the τ_2 time period and was fit with an exponential growth function which resulted in a rate of ~50 fs. As previously mentioned the spectral window of the IR generated from the difference frequency generation process (Figure 3.4.1) does not encompass the full spectral character of the OD stretch. This "growth" can be explained by the relaxation of ν_{OD} from the $\nu_{OD} = 1 \rightarrow 2$ coherence to a population in $\nu_{OD} = 1$. The overall effect of such phenomenon is weakening of the hydrogen-bond network. Lock and Bakker described a similar phenomenon in their HOD studies in D_2O [29]. In their work they attributed the weakening of the hydrogen bond to increased bend in the hydrogen bonding network of the H–O···H system. In the DOAr-Py system this weakening could also be attributed to a lengthening in the N···O distance. Determining which of these contributes more in this system is beyond the scope of this experiment, however, both of these phenomenon would lead to an overall blue-shift in the ν_{OD} mode.

The correlation spectrum from the FFT of all of the residuals exhibited a similar low frequency mode at 120 cm^{-1} (see Figure 3.4.3A).

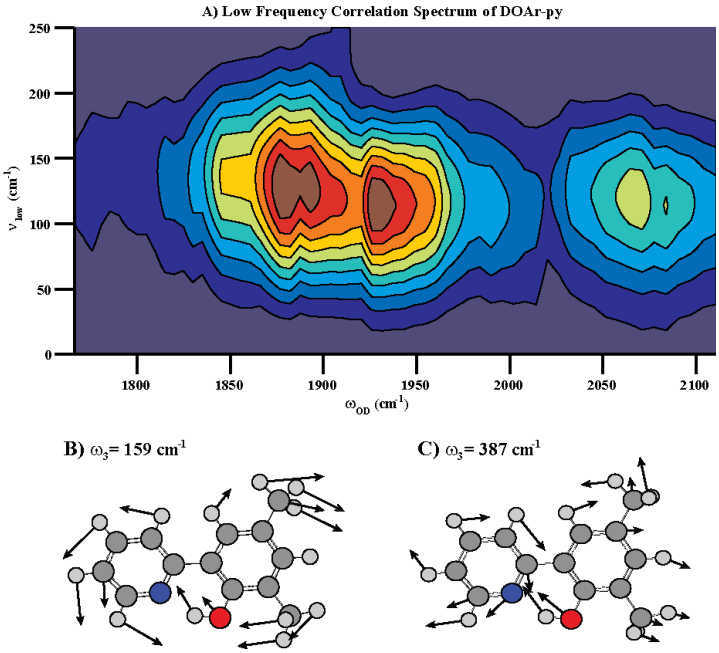

Figure 3.4.3 A) Correlation spectrum of DOAr-Py indicating correlation of many high frequency modes with the low frequency mode at ~120 cm^{-1}. As can be seen in the spectrum the low frequency correlation exhibits a negative slope indicating an anti-correlation between the high frequency mode and low frequency modulation. **B)** A low frequency mode of DOAr-Py at 159 cm^{-1} with displacement vectors that contributes to the correlation spectrum **A** as indicated by the coupling strength in Table 3.4.2. **C)** Another low frequency mode at 387 cm^{-1} that is strongly coupled to the ν_{OD} stretch though outside of the pump-field bandwidth.

The correlation spectrum clearly exhibits a negative slope indicating an anti-correlation between the high frequency modes and low frequency modulation. This anti-correlation can be attributed to the strength of the OD···N hydrogen bond of the pyridine ring modulating the strength of the ν_{OD} high frequency mode. Similar dynamics have been witnessed in strongly hydrogen-bonding systems [25, 36]. This correlation also strongly suggests possible anharmonic coupling of the hydrogen bonding vibrations which has been seen in strong hydrogen-bonding systems by Cheatum and co-workers[38] as well as Petersen *et al*.

The DFT calculations show a possible corresponding modulation at 159 cm^{-1} for the model system with methyl substituents. The calculations indicate an asymmetric bend of the structure providing the bond between the phenol and pyridine as the backbone for a breathing motion. The

anharmonic calculations provided cubic and semi-diagonal coupling terms of low frequency structural modes to the high frequency ν_{OD} mode. Tables 3.4.1 and 3.4.2 highlight the low frequency modes that are highly coupled to the ν_{OD} mode and contribute to the correlation spectrum shown in Figure 3.4.3A. The anharmonic frequency calculation for the structure yielded a ν_{OD} fundamental frequency of 2078 cm^{-1} (Table 3.4.1). This result closely matches the fundamental frequency of the FTIR spectrum at 2023 cm^{-1}.

Table 3.4.1: Description of the frequency calculation of DOAr-Py with the harmonic (ω_0) and anharmonic correction (ω). (ip = in-plane, oop = out-of-plane)

Low Frequency Mode	Mode	$\omega_{0,j}$ (cm^{-1})	ω_j (cm^{-1})
Butterfly (symmetric oop bending)	3	77	76
Methyl wagging, ip asymmetric bend	4	136	103
H-bond stretch (ip bending)	6	159	153
Asymmetric oop bend	7	190	188
Methyl-Methyl scissor, σ(Ph-Py) stretch	9	260	252
Assymetric Pyridyl-Phenyl and OH stretch	10	324	320
σ(Ph)/τ(Py) stretch and twist	11	343	337
H-bond shearing (ip bending)	13	388	384
OD stretch	66	2296	2078

As mentioned the most intense low frequency mode is at ~120cm^{-1}. Although the calculations were conducted with methyl substituents, the mode at 159 cm^{-1} is strongly coupled with a force constant of 1.65 cm^{-1} and within the pump spectrum (See Table 3.4.2).

Table 3.4.2: Cubic coupling constants ϕ_{ijk} (cm^{-1}) from anharmonic frequency calculation of the low frequency modes in DOAr-Py and ν_{OD} (66) mode are shown. The mode of interest 6 corresponds to the 159 cm^{-1} structural modes in Table 3.4.2, respectively.

Mode (*i* = 66)		***J***								
		3	**4**	**6**	**7**	**9**	**10**	**11**	**13**	**66**
K	**3**	5.08	1.04	-0.11	0.01	0.000	0.000	0.02	0.09	1.17
	4	-	-0.60	-0.01	-0.001	0.000	0.000	0.002	0.001	3.21
	6	-	-	1.65	0.001	0.000	0.000	-0.02	0.10	0.54
	7	-	-	-	1.57	0.000	0.000	0.48	0.19	-0.64
	9	-	-	-	-	1.70	-0.01	0.000	0.000	0.000
	10	-	-	-	-	-	-0.002	0.000	0.000	-0.003
	11	-	-	-	-	-	-	1.57	-0.03	-1.42
	13	-	-	-	-	-	-	-	183.70	4.19
	66	-	-	-	-	-	-	-	-	-18.82

3.5 Experimental Details for DOAr-ND_2 Pump-probe studies

The synthesis of the HOAr-NH_2 form of the sample was performed by Rhile and co-workers as described in their supporting information [16]. The deuteron versions of HOAr-NH_2 where studied to minimize interference from nearby alkyl and aromatic vibrational modes. The deuteron exchange was conducted by Schrauben and co-workers less than one day in advance to ensure fully enriched sample. HOAr-NH_2 was prepared in $CHCl_3$ at a concentration of 0.65 M. The use of $CHCl_3$ for the solvent minimizes interference from the solvent on the intra-molecular hydrogen bonding network which is our reporter on how structural modulations affect molecular dynamics and subsequent PCET. The home-built sample cell uses two 1 mm CaF_2 windows separated by a 200 μm thick Teflon spacer. More details about the experimental setup can be found in Chapter 2 Section 4. All FTIR spectra were obtained using a JASCO FT/IR-4100 spectrometer with 2 cm^{-1} resolution.

The experiments discussed in this article were performed using a commercially available 1 kHz Spectra-Physics Spitfire Ti:sapphire Laser system. The infrared pump-field was generated by difference frequency generation by an in-house built optical parametric amplifier. Here the

800nm light generated by the Spitfire Laser was down-converted into a signal and idler beam in the near-IR regime. The near-IR signal and idler beam were then nonlinearly mixed in an $AgGaS_2$ crystal to generate the mid-IR light tuned to 2177 cm^{-1}, as shown by the red spectrum in Figure 3.6.1 [22, 23]. The pump-field was temporally characterized, as discussed in Chapter 2 Section 2, resulting in a pulse width at half max of ~60 fs. These pulse durations correspond to bandwidths of ~270 cm^{-1}.

The mid-IR probe-field was generated by using the broadband IR (BBIR) technique described in Chapter 2 Section 3. For these experiments the pressure in the gas cell during BBIR generation was set at 450 Torr, which achieved a spectrum of greater than 1300 cm^{-1} centered at 2600 cm^{-1}, as shown by the black spectrum in Figure 3.6.1. The BBIR was temporally characterized by a cross correlation with 800 nm light in a silicon wafer as described in Chapter 2 Section 2. This cross-correlation yielded a pulse width of 40 fs for the BBIR. The mid-IR pump-field and BBIR generated probe-field were focused onto the sample in a pump-probe geometry as described in Chapter 2 Section 4 (refer to Figure 2.4.1 for details). A cross-correlation between the pump and probe fields was collected in $AgGaS_2$ to ensure spatial and temporal overlap in the sample and yielded a pulse width of 150 fs. The pump-probe traces were fit with two exponentials to extract information about the population dynamics starting at 90 fs.

3.6 Pump-probe Results of DOAr-ND_2

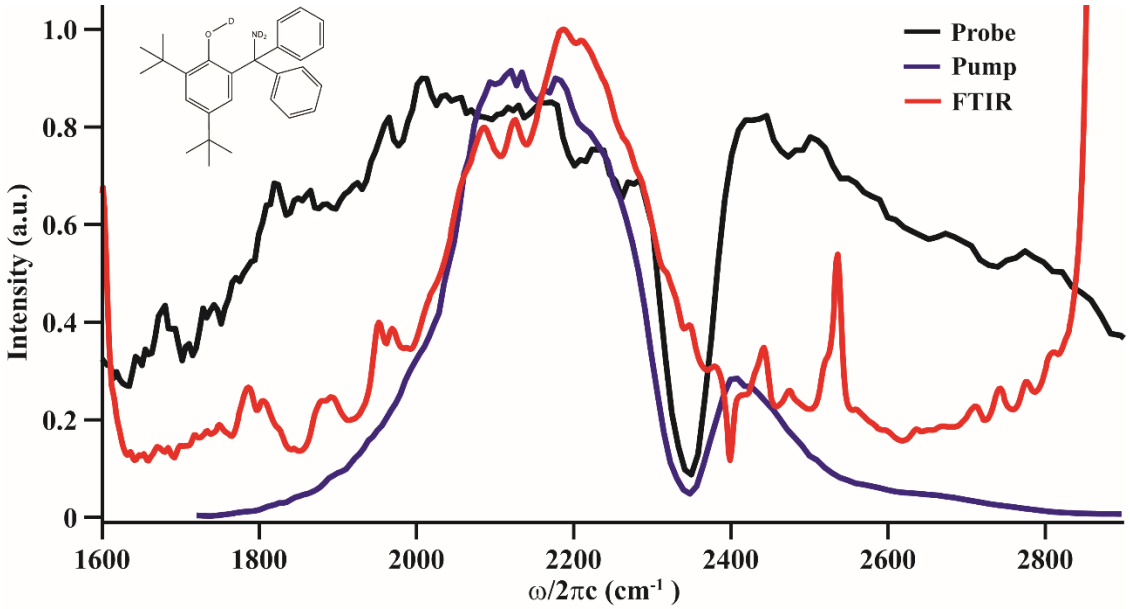

Figure 3.6.1: Normalized FTIR spectrum of the DOAr-ND_2 compound in the range of interest in red. The solid black line is a trace of the broadband mid-IR spectral content of the probe used during the pump-probe experiment. The solid blue line is a spectrum of the mid-IR pump-field. The inset is of the DOAr-ND_2 structure.

The FTIR spectra of the DOAr-ND_2 sample shows a broad line shape centered in the 1550-2400 cm^{-1} range attributed to the ν_{OD} stretch (see Figure 3.6.1). As indicated in Figure 3.6.1, the mid-IR pump-field generated by the difference frequency generation does not contain enough spectral content to pump the entire region of the ν_{OD} stretch, though it does cover most of the fundamental region. However, the BBIR probe allows us to probe the entire fundamental and overtone of the ν_{OD} region in addition to adjacent spectral information. The line-shape in this region has significant structure which makes it difficult to decipher the underlying dynamics that give rise to broad features and multiple peaks. The pump-probe measurements provide a window to view the dynamics in more detail.

The parallel (ZZZZ) and crossed (ZZYY) pump-probe spectra as a function of the detection frequency at various time delays are shown in Figure 3.6.2. The bleach (negative peak) is centered

at the peak of the FTIR transition and the excited state absorption (positive peak) is centered at the transition from the ν=1 to the ν=2 state. The ground state bleach and excited state absorption peaks shown in Figure 3.6.2 A at τ_2 = 0 fs were fit with a Gaussian function of floating width for the fundamental and the overtone of each local mode. For DOAr-ND_2 the energy of the fundamental transition was determined to be 2185 cm^{-1} and the corresponding overtone transition was 1879 cm^{-1}. The DOAr-ND_2 complex exhibits a single broad OD mode which gives rise to an anharmonicity of 306 cm^{-1}. This anharmonicity value is significantly larger than the 180 to 235 cm^{-1} range reported by Rospenk *et al*. for phenol•pyridine complexes in carbon tetrachloride and suggests a very strong intra-molecular hydrogen bond.[26] Similar studies[27, 28] have shown that strong hydrogen bond formation increases the anharmonicity for the ν_{OD} stretch.

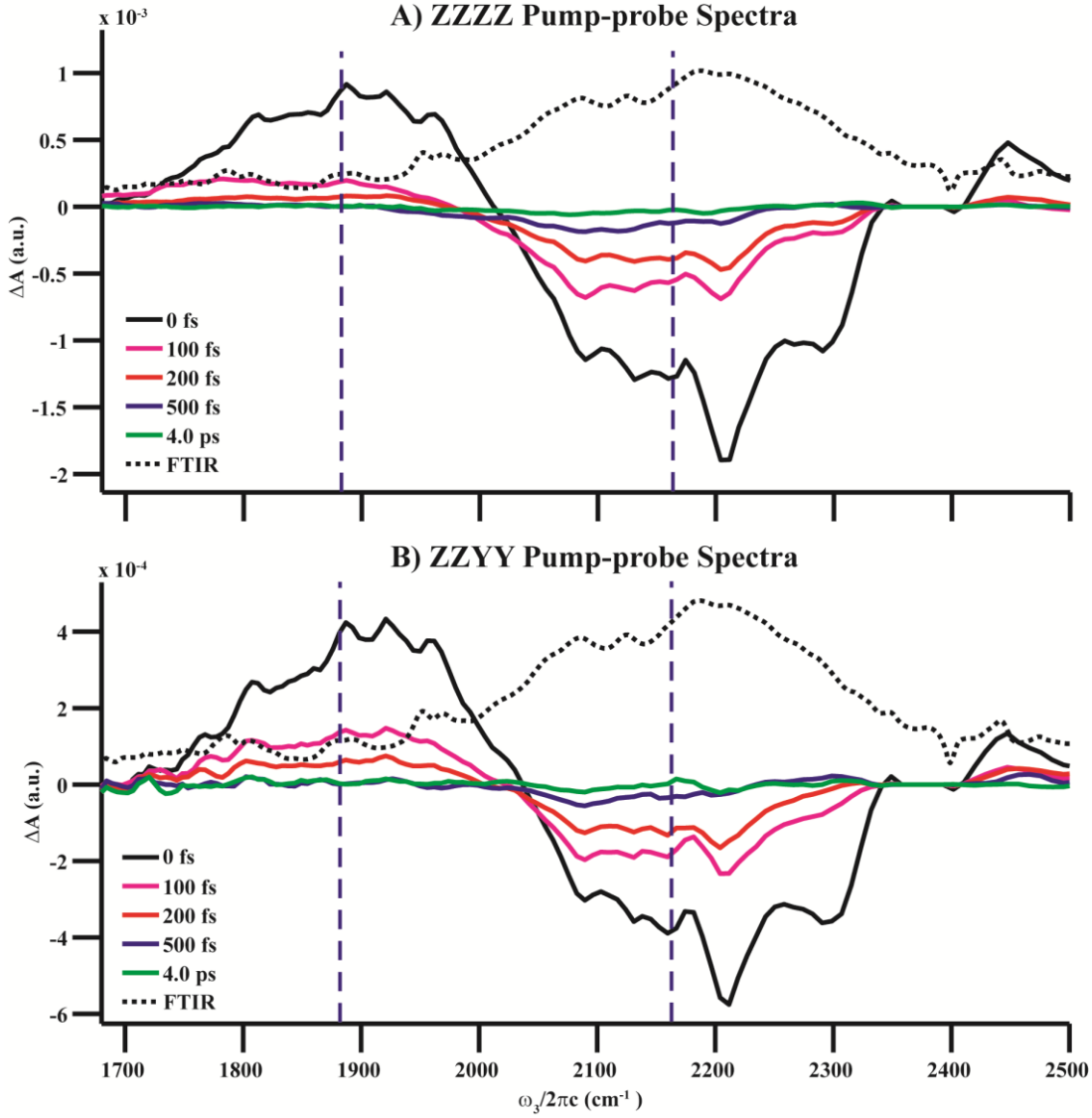

Figure 3.6.2: Polarization selective pump-probe spectra of DOAr-ND_2. **A)** The ZZZZ Pump-probe spectra of DOAr-ND_2 at selected τ_2 points of 0, 100, 200, 500, and 4000 fs. **B)** The ZZYY Pump-probe spectra of DOAr-ND_2 at selected τ_2 points of 0, 100, 200, 500, and 4000 fs. The FTIR of DOAr-ND_2 in both spectra were scaled to 1.2× the amplitude of the respective overtone transitions at τ_2 = 0 fs. The blue-dashed lines represent the frequency of the traces shown if Figure 3.6.3 for both the ZZZZ and ZZYY pump-probe spectra.

The isotropic pump-probe trace for DOAr-ND_2 at the fundamental, 2185 cm^{-1}, was fit with a two exponentials of 165 fs and 1.8 ps. Details of how the isotropic response is calculated from the parallel (ZZZZ) and crossed (ZZYY) datasets shown in Figure 3.6.2 is described in Chapter 2 Section 6. The reorganizational motions associated with molecular rotations have been removed

in the isotropic response allowing for a more accurate portrayal of the ν_{OD} population dynamics [33]. The overtone at 1879 cm^{-1} exhibited somewhat faster dynamics with an initial decay of 140 fs and longer decay of 2.2 ps. These two component decay rates are typical of strong hydrogen bonding systems such as those by the $\nu_{OH/OD}$ mode in D_2O/HOD vibrational relaxation experiments as previously described above in Section 4 [29-35].

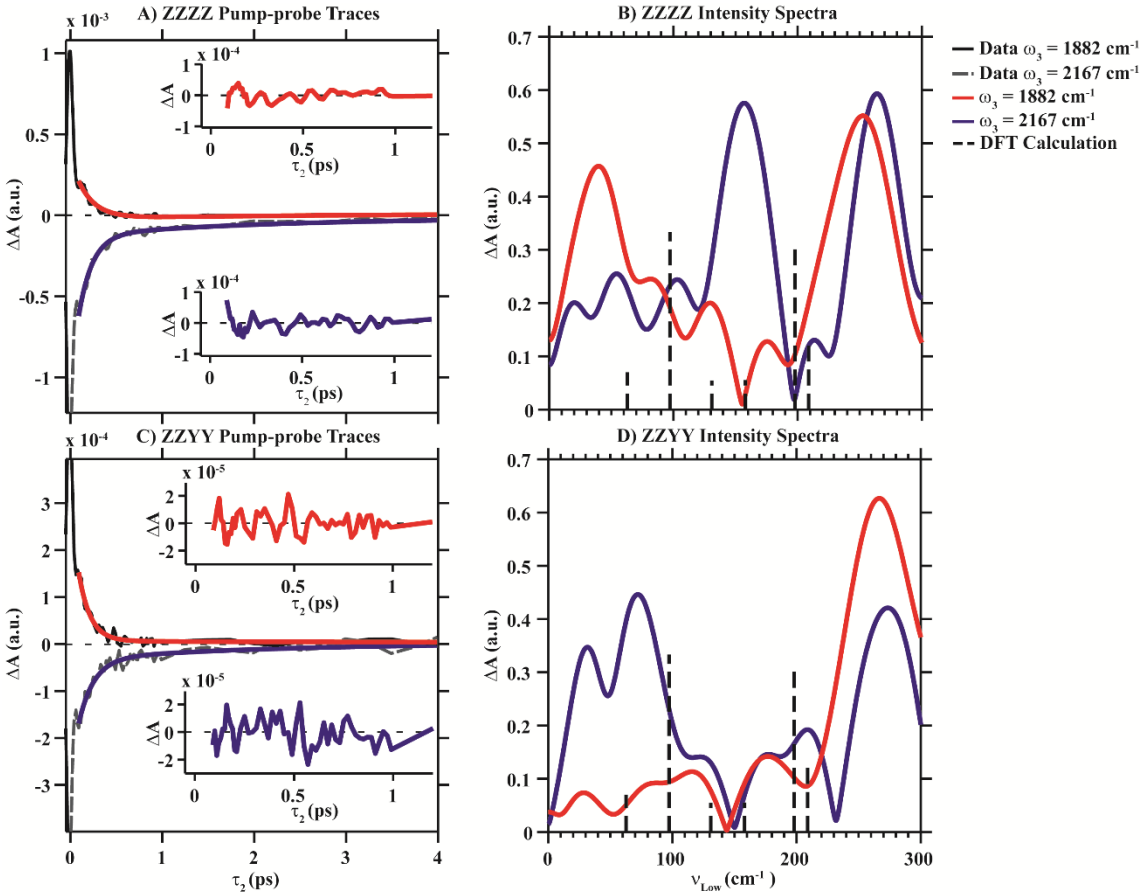

Figure 3.6.3: Polarization selective pump-probe traces and coupled low frequency modes of DOAr-ND_2. **A)** The ZZZZ pump-probe traces at 1882 and 2167 cm^{-1} as indicated by the dashed-blue line in Figure 3.6.2 **A**. These traces were chosen as they represent the fundamental and overtone spectral regions. The black-solid line and red-solid line for the 1882 cm^{-1} frequency trace are the original data and exponential fit, respectively. Likewise, the grey-dashed line and blue-solid line for the 2167 cm^{-1} frequency trace are the original data and exponential fit, respectively. The residual for each trace is shown as an inset to **A**. The red-solid line in the upper inset is the residual for the 1882 cm^{-1} trace and blue-solid in the lower inset is the residual for the 2167 cm^{-1} trace. **B)** The intensity spectra of the trace along 1882 and 2167 cm^{-1} calculated from the Fast-Fourier Transform of the residual in the insets of **A**. The red-solid line is the intensity spectrum for the 1882 cm^{-1} trace, and the blue solid-line is the intensity spectrum for the 2167 cm^{-1} trace. The black-dashed sticks indicate harmonic frequency calculation (See Table 3.6.1). **C** and **D** represents the same treatment for the ZZYY response shown in Figure 3.6.2 **B**.

Additionally the residuals of the fits in the fundamental region demonstrate a strong oscillatory component (Figure 3.6.3 A and C). Figures 3.6.3 B and D show the spectrum from the FT of these residuals. The ZZZZ residual spectrum shows an anharmonically coupled low frequency mode at 127 and 157 cm^{-1} (see Figure 3.6.3 B). Furthermore, previous studies have measured the low

frequency solvent modes of $CHCl_3$ at 252 and 366 cm^{-1} indicating the low frequency modes shown here are not a result of the solvent[39, 40]. The lack of coupling to the 157 cm^{-1} and 127 cm^{-1} low frequency mode in ZZYY Figure 3.6.3 D indicates that these modes occur in the same plane as the ν_{OD} mode. This is in agreement with the displacement vectors calculated by DFT in Gaussian09C for these vibrational modes (see Figure 3.6.4 B and C) [41].

The isotropic correlation spectrum from the FFT of all of the residuals in the fundamental and overtone spectral regions exhibit a similar low frequency mode at 155 cm^{-1} (See Fig 3.6.4 A).

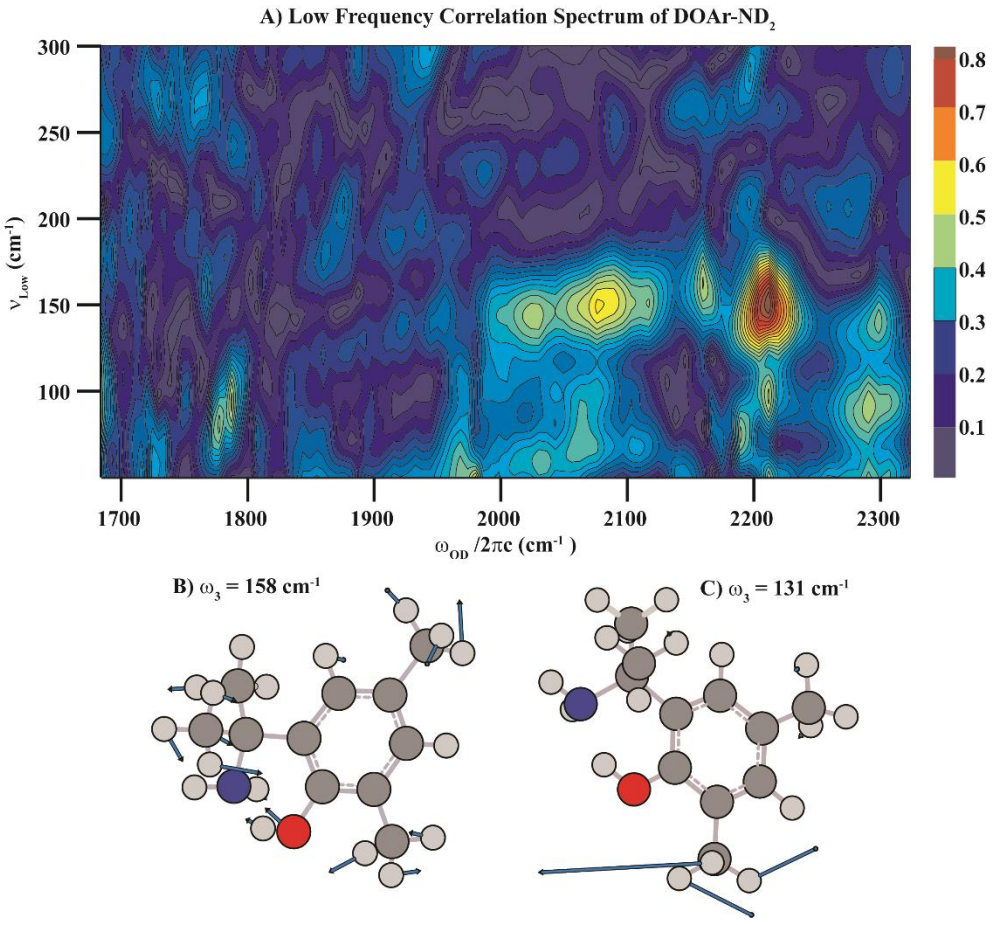

Figure 3.6.4: A) Isotropic correlation spectrum of DOAr-ND_2 indicating correlation of many high frequency modes with the low frequency mode at ~150 cm^{-1}. **B)** A low frequency mode of DOAr-ND_2 at 158 cm^{-1} with displacement vectors that contributes to the correlation spectrum **A** as indicated by the coupling strength in Table 3.6.2. **C)** Another low frequency mode at 131 cm^{-1} that also contributes to the correlation spectrum as indicated in far-IR spectrum of the 1882 cm^{-1} spectral component.

Unlike the anti-correlation seen in the DOAr-Py, there appears to be little-to-no correlation in the DOAr-ND_2 complex. The lack of rigidity of the DOAr-ND_2 and longer OD···N can explain this significant difference. However the strong presence of the correlation of the 155 cm^{-1} mode to the ground state bleach suggests possible anharmonic coupling of the hydrogen bonding vibrations which has been seen in strong hydrogen-bonding systems by Cheatum and co-workers[38] as well as Petersen *et al*. The overtone spectral region of the correlation spectrum suggests coupling to different low frequency modes such as the 127 cm^{-1} mode shown in Figure 3.6.3 B. This is also a departure from the DOAr-Py which had shown coupling to similar low frequency modes in both the fundamental and overtone spectral regions.

The DFT calculations show a possible corresponding modulation at 150 cm^{-1} for the model system with methyl substituents. The calculations indicate a symmetric out-of-plane bend accompanied by a twist of the $–Ph_2ND_2$ substituent of the structure providing the bond between the phenol and amine as the backbone for a breathing motion. The anharmonic calculations provided cubic and semi-diagonal coupling terms of low frequency structural modes to the high frequency ν_{OD} mode. Tables 3.6.1 and 3.6.2 highlights the low frequency modes that are highly coupled to the ν_{OD} mode and contribute to the correlation spectrum shown in figure 3.6.3A. The anharmonic frequency calculation for the structure yielded a ν_{OD} fundamental frequency of 2202 cm^{-1} (Table 3.6.1). This result closely matches the fundamental frequency of the FTIR spectrum at 2185 cm^{-1}.

Table 3.6.1: Description of the frequency calculation of DOAr-ND_2 with the harmonic (ω_0) and anharmonic correction (ω). (ip = in-plane, oop = out-of-plane)

Mode Type	Mode	$\omega_{0,j}$ (cm^{-1})	ω_j (cm^{-1})
τ(*p*-Me)/τ(-Ph_2ND_2) twist	2	62.7	62.0
Symmetric oop bend	3	97.2	88.7
τ(*o*-Me)/τ(-Ph_2ND_2) twist	4	130.9	109.1
Symmetric oop bend, t(-Ph2ND2) twist	5	158.0	147.7
Ph_2ND_2 Wagging, oop symmetric bend	6	197.9	189.4
Ph_2ND_2 Wagging, symmetric phenyl stretch	7	208.9	200.1
OD Stretch	68	2415.5	2202.2

As mentioned the most intense anharmonically coupled low frequency structural modulations are the 157cm^{-1} and possibly 127 cm^{-1} structural modes. Although the calculations were conducted with methyl substituents, the modes at 131 (mode 4) and 158 cm^{-1} (mode 5) are strongly coupled with force constants of 0.8096 and -3.7684 cm^{-1}, respectively, and within the pump spectrum bandwidth (Table 3.6.2). Additionally, Table 3.6.2 indicates strong cross coupling terms between the ν_{OD} (mode 68) and low frequency modes at 131 and 158 cm^{-1} where the cross coupling $mode_{ijk}$ = 68,68,4 corresponds to a coupling constant of -11.6189 cm^{-1} and $mode_{ijk}$ = 68,68,5 = 23.9577 cm^{-1}. The large cross coupling terms in DOAr-ND_2 are a departure from the small cross coupling terms in DOAr-Py.

Table 3.6.2: Cubic coupling constants ϕ_{ijk} (cm^{-1}) from anharmonic frequency calculation of the low frequency modes in DOAr-ND_2 and ν_{OD} mode (68) are shown. Modes of interest 4 and 5 correspond to the 131 and 158 cm^{-1} structural modes in Table 3.6.1, respectively.

Mode (*i* = 68)		***J***						
		2	**3**	**4**	**5**	**6**	**7**	**68**
k	**2**	0.5568	-	-	-	-	-	30.1596
	3	-	-1.6460	-	-0.6339	0.3526	-	6.0161
	4	-	-	0.8096	-	-	-	-11.6189
	5	-	-	-	-3.7684	0.7497	-	23.9577
	6	-	-	-	-	-1.03418	-	15.7706
	7	-	-	-	-	-	0.3176	0.5868
	68	-	-	-	-	-	-	3.2649

3.7 Concluding remarks on DOAr-Py and DOAr-ND_2

Due to the complexity of the lineshapes in the pump-probe measurements, also reflected in the FTIR spectra, it is difficult to give much detail about the vibrational landscape. In similar systems exhibiting strong hydrogen bonding, this underlying spectral structure has been attributed to Franck-Condon like overlap induced by anharmonic coupling through low frequency structural modes giving rise to broad lineshapes with complex structure[36]. These features have also been attributed to Fermi-resonance coupling of the ν_{OD} mode to the overtones[38, 42]. While neither explanation can be excluded, the correlation of the ν_{OD} stretch with the low frequency mode in the DOAr-Py and DOAr-ND_2 complex strongly suggests anharmonic coupling through low frequency structural modes gives rise to these broad lineshapes. Furthermore, the anti-correlation of the high frequency mode and low frequency mode in the DOAr-Py correlation spectrum gives more credence to this hypothesis by providing a broad environment for the ν_{OD} stretch to sample through strong OD···N hydrogen-bonding of the adjacent pyridine as suggested by fast kinetic rates and large anharmonicity.

However, the many differences between the correlation spectrum of the DOAr-Py and DOAr-ND_2 as alluded previously does indicate different molecular dynamics. We can conclude that the difference in the kinetic rates for OD/N hydrogen bonding population relaxation may be caused by the rigidity or lack thereof in each molecule and proximity of aromatic ring structures in the molecule. The faster population decay rates in the DOAr-Py of well over a picosecond may be indicative of a strong hydrogen-bonding environment further supported by relatively large anharmonicities. Furthermore, the pump-probe results and DFT calculations do indicate strong anharmonic coupling to low frequency modulations. These low frequency modes do strongly

affect the hydrogen bonding within these systems. Ultrafast visible-pump IR-probe experiments may yield information about the proton transfer and electron transfer.

References

1. Markle, T.F., et al., *Probing concerted proton–electron transfer in phenol–imidazoles.* Proceedings of the National Academy of Sciences, 2008. **105**(24): p. 8185-8190.
2. Markle, T.F. and J.M. Mayer, *Concerted Proton–Electron Transfer in Pyridylphenols: The Importance of the Hydrogen Bond.* Angewandte Chemie International Edition, 2008. **47**(4): p. 738-740.
3. Rhile, I.J., et al., *Concerted Proton−Electron Transfer in the Oxidation of Hydrogen-Bonded Phenols.* Journal of the American Chemical Society, 2006. **128**(18): p. 6075-6088.
4. Tommos, C. and G.T. Babcock, *Proton and hydrogen currents in photosynthetic water oxidation.* Biochimica et Biophysica Acta (BBA) - Bioenergetics, 2000. **1458**(1): p. 199-219.
5. Westlake, B.C., et al., *Concerted electron-proton transfer in the optical excitation of hydrogen-bonded dyes.* Proceedings of the National Academy of Sciences, 2011. **108**(21): p. 8554-8558.
6. Kühne, H. and G.W. Brudvig, *Proton-Coupled Electron Transfer Involving Tyrosine Z in Photosystem II†.* The Journal of Physical Chemistry B, 2002. **106**(33): p. 8189-8196.
7. Faller, P., et al., *Resolving intermediates in biological proton-coupled electron transfer: A tyrosyl radical prior to proton movement.* Proceedings of the National Academy of Sciences, 2003. **100**(15): p. 8732-8735.
8. Siegbahn, P.E.M., *Structures and Energetics for O2 Formation in Photosystem II.* Accounts of Chemical Research, 2009. **42**(12): p. 1871-1880.
9. Sjödin, M., et al., *The mechanism for proton-coupled electron transfer from tyrosine in a model complex and comparisons with Y(Z) oxidation in photosystem II.* Philosophical Transactions of the Royal Society B: Biological Sciences, 2002. **357**(1426): p. 1471-1511.
10. Cukier, R.I., *Mechanism for Proton-Coupled Electron-Transfer Reactions.* The Journal of Physical Chemistry, 1994. **98**(9): p. 2377-2381.
11. Schrauben, J.N., et al., *Multiple-Site Concerted Proton–Electron Transfer Reactions of Hydrogen-Bonded Phenols Are Nonadiabatic and Well Described by Semiclassical Marcus Theory.* Journal of the American Chemical Society, 2012. **134**(40): p. 16635-16645.
12. Cukier, R.I. and D.G. Nocera, *PROTON-COUPLED ELECTRON TRANSFER.* Annual Review of Physical Chemistry, 1998. **49**(1): p. 337-369.
13. Mayer, J.M., *PROTON-COUPLED ELECTRON TRANSFER: A Reaction Chemist's View.* Annual Review of Physical Chemistry, 2004. **55**(1): p. 363-390.
14. Hammes-Schiffer, S. and A.V. Soudackov, *Proton-Coupled Electron Transfer in Solution, Proteins, and Electrochemistry†.* The Journal of Physical Chemistry B, 2008. **112**(45): p. 14108-14123.

15. Soudackov, A., E. Hatcher, and S. Hammes-Schiffer, *Quantum and dynamical effects of proton donor-acceptor vibrational motion in nonadiabatic proton-coupled electron transfer reactions.* The Journal of Chemical Physics, 2005. **122**(1): p. 014505.
16. Rhile, I.J. and J.M. Mayer, *One-Electron Oxidation of a Hydrogen-Bonded Phenol Occurs by Concerted Proton-Coupled Electron Transfer.* Journal of the American Chemical Society, 2004. **126**(40): p. 12718-12719.
17. Gilli, P., et al., *Evidence for Intramolecular N−H···O Resonance-Assisted Hydrogen Bonding in β-Enaminones and Related Heterodienes. A Combined Crystal-Structural, IR and NMR Spectroscopic, and Quantum-Mechanical Investigation.* Journal of the American Chemical Society, 2000. **122**(42): p. 10405-10417.
18. Inoue, Y., et al., *Ethylene Polymerization Behavior of New Titanium Complexes Having Two Phenoxy-Pyridine Chelate Ligands.* Chemistry Letters, 2001. **30**(10): p. 1060-1061.
19. Allerhand, A. and P. von R. Schleyer, *Solvent Effects in Infrared Spectroscopic Studies of Hydrogen Bonding.* Journal of the American Chemical Society, 1963. **85**(4): p. 371-380.
20. Brookes, J.F., et al., *Effect of Solvent Polarity on the Vibrational Dephasing Dynamics of the Nitrosyl Stretch in an FeII Complex Revealed by 2D IR Spectroscopy.* The Journal of Physical Chemistry A, 2013. **117**(29): p. 6234-6243.
21. Lynch, M.S., et al., *Coherent Fifth-Order Visible–Infrared Spectroscopies: Ultrafast Nonequilibrium Vibrational Dynamics in Solution.* The Journal of Physical Chemistry A, 2012. **116**(26): p. 7023-7032.
22. Elsaesser, T., H. Lobentanzer, and A. Seilmeier, *Generation of tunable picosecond pulses in the medium infrared by down-conversion in AgGaS2.* Optics Communications, 1985. **52**(5): p. 355-359.
23. Cerullo, G. and S. De Silvestri, *Ultrafast optical parametric amplifiers.* Review of Scientific Instruments, 2003. **74**(1): p. 1-18.
24. Tokmakoff, A., B. Sauter, and M.D. Fayer, *Temperature-dependent vibrational relaxation in polyatomic liquids: Picosecond infrared pump–probe experiments.* The Journal of Chemical Physics, 1994. **100**(12): p. 9035-9043.
25. Heyne, K., et al., *Coherent low-frequency motions of hydrogen bonded acetic acid dimers in the liquid phase.* The Journal of Chemical Physics, 2004. **121**(2): p. 902-913.
26. Rospenk, M. and T. Zeegers-Huyskens, *FT-IR (7500−1800 cm-1) Study of Hydrogen-Bond Complexes between Phenols−OH(OD) and Pyridine. Evidence of Proton Transfer in the Second Vibrational Excited State.* The Journal of Physical Chemistry A, 1997. **101**(45): p. 8428-8434.
27. Asselin, M. and C. Sandorfy, *A low temperature infrared study of the band-width and frequency in self-associated alcohols.* Chemical Physics Letters, 1971. **8**(6): p. 601-603.
28. Asselin, M. and C. Sandorfy, *Double Excitation in the Infrared Spectra of Self-Associated Alcohols.* The Journal of Chemical Physics, 1970. **52**(12): p. 6130-6134.
29. Lock, A.J. and H.J. Bakker, *Temperature dependence of vibrational relaxation in liquid H2O.* The Journal of Chemical Physics, 2002. **117**(4): p. 1708-1713.
30. Nibbering, E.T.J. and T. Elsaesser, *Ultrafast Vibrational Dynamics of Hydrogen Bonds in the Condensed Phase.* Chemical Reviews, 2004. **104**(4): p. 1887-1914.
31. Rini, M., et al., *Femtosecond mid-infrared spectroscopy of condensed phase hydrogen-bonded systems as a probe of structural dynamics.* Faraday Discussions, 2003. **122**(0): p. 27-40.

32. Nienhuys, H.-K., et al., *Mechanism for vibrational relaxation in water investigated by femtosecond infrared spectroscopy.* The Journal of Chemical Physics, 1999. **111**(4): p. 1494-1500.
33. Nicodemus, R.A., et al., *Collective Hydrogen Bond Reorganization in Water Studied with Temperature-Dependent Ultrafast Infrared Spectroscopy.* The Journal of Physical Chemistry B, 2011. **115**(18): p. 5604-5616.
34. Loparo, J.J., et al., *Reorientational and configurational fluctuations in water observed on molecular length scales.* Physical Review B, 2004. **70**(18): p. 180201.
35. Fecko, C.J., et al., *Ultrafast Hydrogen-Bond Dynamics in the Infrared Spectroscopy of Water.* Science, 2003. **301**(5640): p. 1698-1702.
36. Petersen, P.B., et al., *Ultrafast N−H Vibrational Dynamics of Cyclic Doubly Hydrogen-Bonded Homo- and Heterodimers.* The Journal of Physical Chemistry B, 2008. **112**(42): p. 13167-13171.
37. Moore, P., et al., *The low frequency density of states and vibrational population dynamics of polyatomic molecules in liquids.* The Journal of Chemical Physics, 1995. **103**(9): p. 3325-3334.
38. Gündoğdu, K., et al., *Relaxation and anharmonic couplings of the O–H stretching vibration of asymmetric strongly hydrogen-bonded complexes.* The Journal of Chemical Physics, 2007. **127**(4): p. 044501.
39. apos, et al., *Infrared Spectra in Polarized Light of Crystalline Chloroform.* The Journal of Chemical Physics, 1972. **57**(10): p. 4136-4142.
40. Andrews, B., A. Anderson, and B. Torrie, *Raman and infrared spectra of crystalline chloroform.* Chemical Physics Letters, 1984. **104**(1): p. 65-70.
41. Frisch, M.J., et al., *Gaussian 09*. 2009, Gaussian, Inc.: Wallingford, CT, USA.
42. Dwyer, J.R., et al., *Ultrafast dynamics of vibrational N–H stretching excitations in the 7-azaindole dimer.* Chemical Physics Letters, 2006. **432**(1–3): p. 146-151.

CHAPTER 4

Polarization Selective Femtosecond Infrared Pump-probe studies on HBQ and DBQ

4.1 HBQ and DBQ: Model Systems for ESIPT Reactions

Excited state intramolecular proton transfer (ESIPT) process is a common charge transfer reaction pathway in systems that undergo proton transfer such as hydrogen atom transfer (HAT) and proton-coupled electron transfer (PCET) [1]. For example, chromophores with highly sensitive proton-accepting and donating character have been used to examine binding centers of proteins such as human serum albumin in fluorescent studies [2-5]. The sensitivity the ESIPT process on solvent polarity indicates complex molecular dynamics that important to the hydrogen atom transfer [6, 7]. The two systems; 10-Hydroxybenzo[h]quinoline (HBQ) and the deuteron isotope counterpart 10-Deuteroxybenzo[h]quinoline (DBQ); have complex structural dynamics that greatly affect the proton transfer in the excited state. Additionally, these systems are structurally similar to model systems used to study the proton-coupled electron transfer process in the oxygen evolving complex (OEC) in photosystem II [8-16]. The vibrational dynamics of the OH and OD stretching vibration (ν_{OH}/ν_{OD}) of these systems were studied using dispersed infrared pump-probe spectroscopy. This study revealed that low frequency structural modulations at 248 cm^{-1} for HBQ and 245 cm^{-1} for DBQ were anharmonically coupled to the ν_{OH} and ν_{OD} modes, respectively. In this chapter, previous studies on these systems are discussed in Section 2 followed by the experimental layout in Section 3. The pump-probe results for HBQ and DBQ are discussed in Sections 4 and 5, respectively. Concluding remarks for both studies can be found in Section 7.

4.2 Previous work on HBQ and DBQ

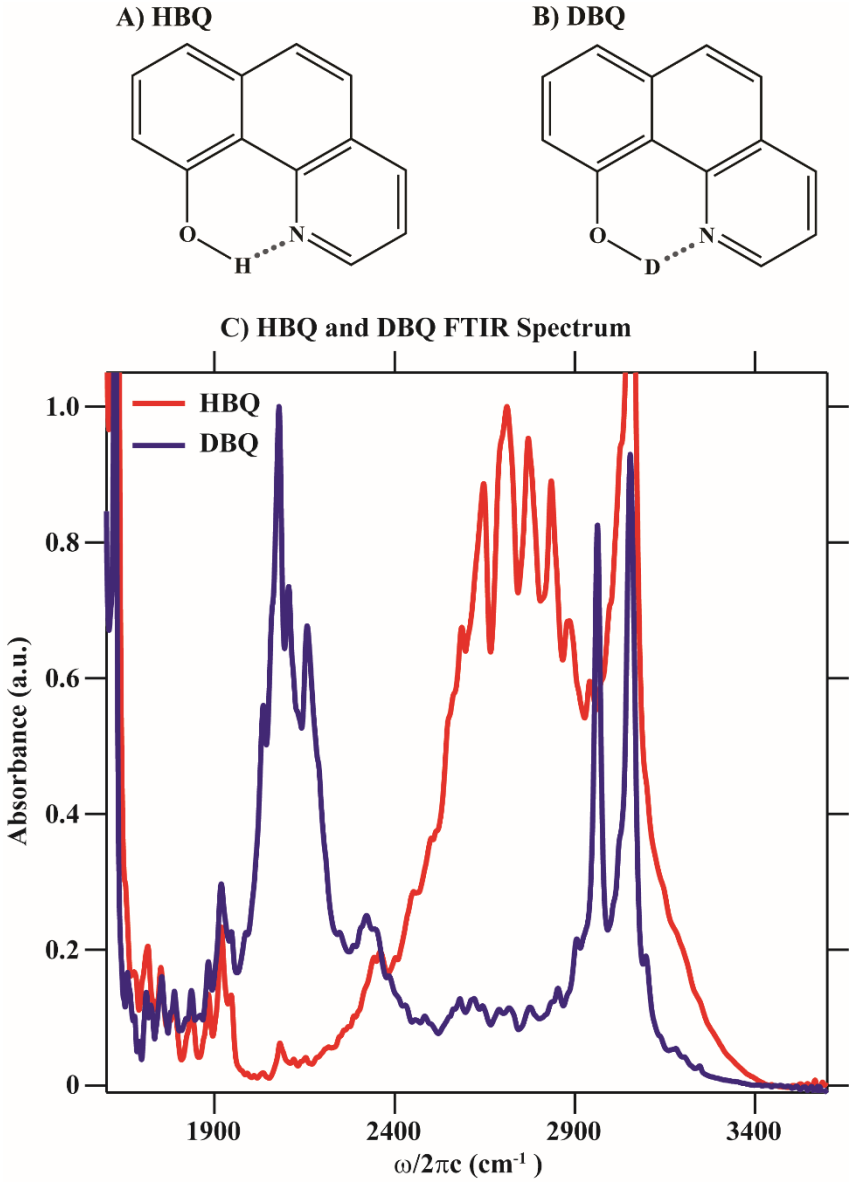

Figure 4.2.1: Molecular structures and normalized FTIR of PCET model systems HBQ and DBQ. **A** and **B)** Molecular structures of HBQ and DBQ, respectively. These model systems mimic the OEC in the photosystem II where the charge transfer for the oxidation of water is driven by the hydrogen bonding of the phenolic proton of tyrosine to a nearby imidazole of histidine.[11] For the systems studied here imidazole was changed to a pyridine for both HBQ and DBQ. **C)** Normalized FTIR spectra of 0.34 M HBQ in CCl_4 and 0.22 M DBQ in CCl_4 compounds in the range of interest. The solid red line is the spectrum of the HBQ and the solid blue line is the spectrum of the DBQ. The pathlengths for these measurements where 200 μm as determined by a Teflon spacer.

Chou and co-workers have conducted steady-state absorption as well as femtosecond fluorescence and transient absorption pump-probe studies in non-polar solvents to gather information on the ESIPT [17]. They were able to observe an enol to keto tautomerization reaction signified by a 30 nm red shift of the fluorescence signal. Based on this enol-keto tautomer reaction they were able to deduce a proton transfer rate of 9.8×10^{12} s^{-1} which roughly corresponds to transfer time of 100 fs. Based on vibrational analysis of their results they also concluded that low frequency skeletal modes modulating the O···N distance of the HBQ structure could play a significant role in the ESIPT. In particular they indicated an in-plane bending mode at 230-250 cm^{-1}. Here the hydron/deuteron isotope was exchanged to determine if there was a noticeable difference between the population decay rates and the effect on low frequency modes. Chou and co-workers concluded the differences between HBQ and DBQ for excited-state intramolecular proton transfer were not significant [17]. Additionally, crystallographic studies by Kubicki *et al* have measured O···N distances that correspond to 2.568 ± 0.008 Å [18]. Ultrafast pump-probe experiments allow us to determine how low frequency structural fluctuations affect intra-molecular hydrogen bonding and to examine anharmonic coupling of the ν_{OH}/ν_{OD} transition to low frequency modes. Understanding the effects of low frequency modes on fluctuations of the reaction coordinate will afford a window into the proton transfer mechanism of the ESIPT reaction [19, 20].

4.3 Experimental Details for HBQ and DBQ

HBQ is commercially available from TCI. DBQ was obtained by deuteron/hydron exchange to >90% enrichment in MeOD solvent. HBQ and DBQ were prepared in CCl_4 at a concentration of 0.34 M and 0.22 M, respectively. The use of CCl_4 for the solvent minimizes

interference from the solvent on the intra-molecular hydrogen bonding network which is our reporter on how structural modulations affect molecular dynamics and subsequent PCET. The home-built sample cell uses two 1 mm CaF_2 windows separated by a 200 μm thick Teflon spacer. More details about the experimental setup can be found in Chapter 2 Section 4. All FTIR spectra were obtained using a JASCO FT/IR-4100 spectrometer with 2 cm^{-1} resolution.

The experiments discussed in this article were performed using a commercially available 1 kHz Spectra-Physics Spitfire Ti:sapphire Laser system. The infrared pump-field was generated by difference frequency generation by an in-house built optical parametric amplifier. Here the 800nm light generated by the Spitfire Laser was down-converted into a signal and idler beam in the near-IR regime. The near-IR signal and idler beam are then nonlinearly mixed in an $AgGaS_2$ crystal to generate the mid-IR light tuned to 2706 cm^{-1} for HBQ and 2100 cm^{-1} DBQ as shown by the blue spectrum in figure 4.5.1 and 4.5.1, respectively [21, 22]. The pump-field was temporally characterized as discussed in Chapter 2 Section 2 resulting pulse widths at half max of ~60 fs. These pulse durations for the pump-field correspond to bandwidths of ~270 cm^{-1}.

The mid-IR probe-field was generated by using the broadband IR (BBIR) technique described in Chapter 2 Section 3. For the HBQ pump-probe experiments, the pressure in the gas cell was set at 780 Torr which achieved a spectral width greater than 1200 cm^{-1} centered at 2980 cm^{-1} as shown by the black spectrum in Figure 4.4.1. For the DBQ pump-probe experiments, the pressure in the gas cell was set at 460 Torr which achieved a spectral width greater than 1200 cm^{-1} centered at 2250 cm^{-1} as shown by the black spectrum in Figure 4.5.1. The BBIR was temporally characterized by a cross correlation with 800 nm light in a silicon wafer as described in Chapter 2 Section 2 prior to each experiment. This cross-correlation yielded a pulse width of 40 fs for the BBIR. The mid-IR pump-field and BBIR probe-field were focused onto the sample in a pump-

probe geometry (refer to Figure 2.4.1 for details). A cross-correlation between the pump and probe fields was collected in $AgGaS_2$ to ensure spatial and temporal overlap in the sample and yielded a pulse width of ~150 fs for both the HBQ and DBQ. The pump-probe traces were fit with two exponentials to extract information about the population dynamics starting at 110 fs. More details about the analysis of the data in this chapter can be found in Chapter 2 Sections 5 and 6. DFT calculations were performed on both HBQ and DBQ. Details about the parameters for these calculations can be found in Chapter 2 Section 7.

4.4 Pump-probe results of HBQ

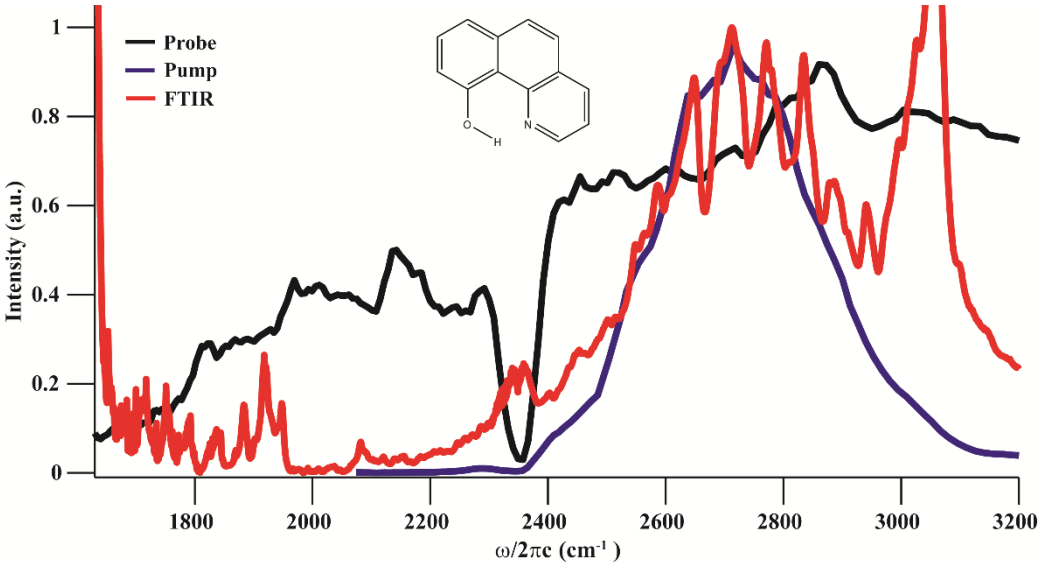

Figure 4.4.1: Normalized FTIR spectrum of the HBQ compound in the range of interest in red. The solid black line is a spectrum of the BBIR probe field. The solid blue line is a trace of the mid-IR pump-field. The inset is of the HBQ structure.

The FTIR spectra of the HBQ sample shows a broad line shape centered in the 2200-3300 cm^{-1} range attributed to the ν_{OH} stretch (see Figure 4.4.1). As indicated by Figure 4.4.1, the mid-IR pump-field generated by the difference frequency generation does not contain enough spectral content to pump the entire region of the ν_{OH} stretch although it does cover most of the fundamental

(ν_{OH}=0→1) region. However, the BBIR probe allows us probe the entire fundamental and overtone transitions of the ν_{OH} stretching mode in addition to monitoring adjacent spectral information. The lineshape in this region has significant structure which makes it difficult to decipher the underlying dynamics which give rise to broad features and multiple peaks. Pump-probe measurements provide a window to view the dynamics in more detail.

The parallel (ZZZZ) and crossed (ZZYY) pump-probe spectra as a function of the detection frequency at various time delays are shown in Figure 4.4.2. The bleach (negative peak) is centered at the peak of the FTIR transition and the excited state absorption (positive peak) is centered at the transition from the ν=1 to the ν=2 state. The ground state bleach and excited state absorption peaks shown in Figure 4.4.2 A at τ_2 = 0 fs were fit with a Gaussian function of floating width for the fundamental and the overtone transition of each local mode. For HBQ the fundamental was determined to be 2736 cm^{-1} and the corresponding overtone 1965 cm^{-1}. The HBQ complex exhibits a single broad ν_{OH} mode which gives rise to an anharmonicity of 771 cm^{-1}. This anharmonicity value is significantly larger than the 180 to 235 cm^{-1} range reported by Rospenk *et al*. for phenol•pyridine complexes in carbon tetrachloride.[23] Similar studies[24, 25] have shown that strong hydrogen bond formation increases the anharmonicity for the ν_{OD} stretch. However, the large anharmonicity value may also be due to the carbon dioxide absorption near the transition between fundamental and overtone spectral regions significantly interfering with this measurement which is the most probable cause of the strong absorption (negative peak) at 2305 wavenumbers.

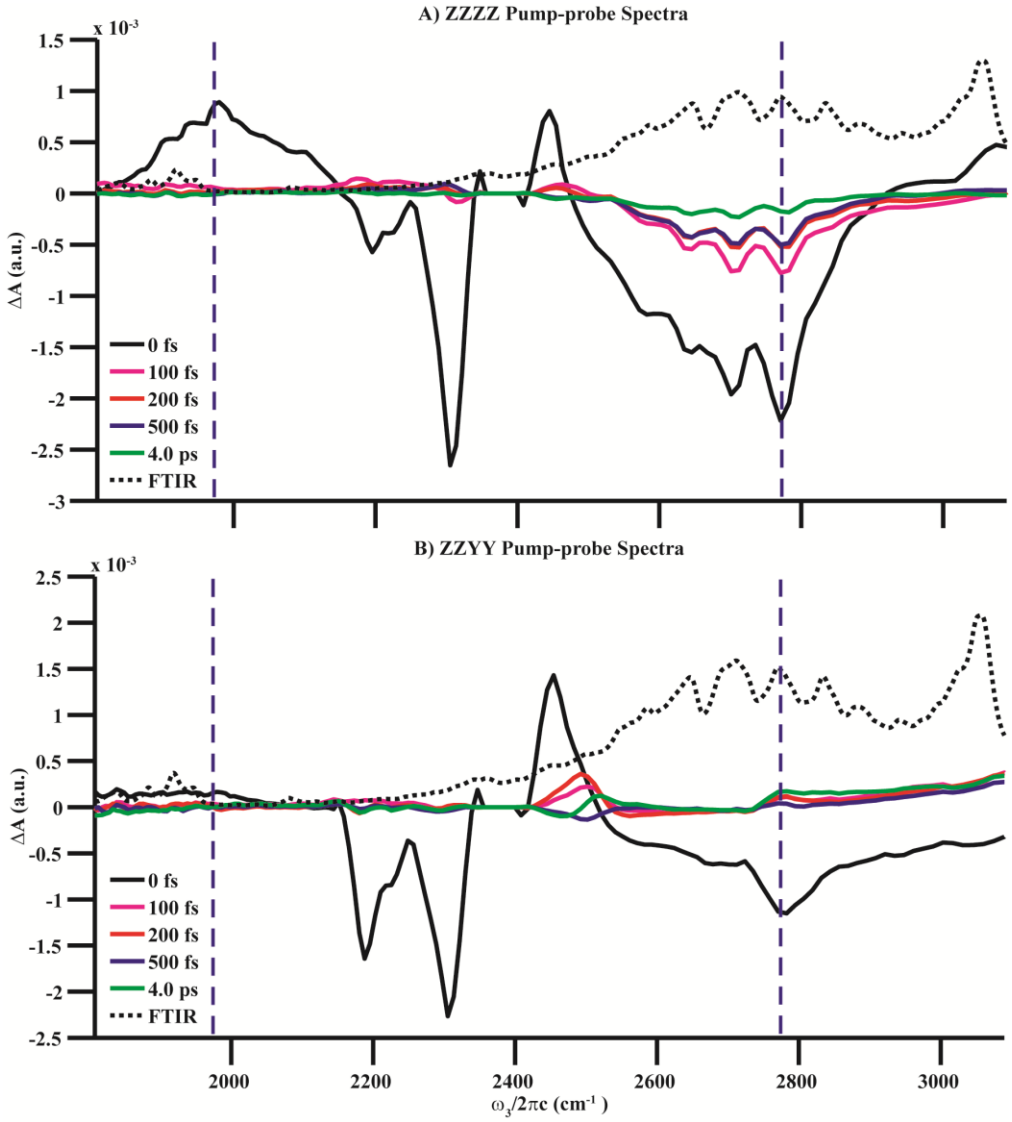

Figure 4.4.2: Polarization selective pump-probe spectra of HBQ. **A)** The ZZZZ pump-probe spectra of HBQ at selected τ_2 points of 0, 100, 200, 500, and 4000 fs. **B)** The ZZYY pump-probe spectra of HBQ at selected τ_2 points of 0, 100, 200, 500, and 4000 fs. The FTIR of HBQ in both of the ZZZZ and ZZYY spectra were scaled to 1.2× the amplitude of the ZZZZ overtone transition at $\tau_2 = 0$ fs. The blue-dashed lines represent the frequency of the traces shown if Figure 4.4.3 for both the ZZZZ and ZZYY pump-probe spectra.

The isotropic pump-probe trace for HBQ at the fundamental, 2771 cm^{-1}, was fit with a two exponentials of 130 fs and 1.2 ps. Details of how the isotropic response is calculated from the parallel (ZZZZ) and crossed (ZZYY) datasets shown in Figure 4.4.2 is described in Chapter 2 Section 6. The reorientational motions associated with molecular rotations have been removed in

the isotropic response allowing for a more accurate portrayal of the ν_{OD} population dynamics [26]. The overtone at 1968 cm^{-1} exhibited somewhat faster dynamics with an initial decay of 115 fs and longer decay of 1.1 ps. These two component decay rates are typical of strong hydrogen bonding systems such as those by the $\nu_{OH/OD}$ mode in D_2O/HOD vibrational relaxation experiments as attributed by Bakker and co-workers and Tokmakoff and co-workers in addition to many others [26-32]. In addition to the decay rates, the fundamental transition has an offset to account for the decay to a non-zero value. Tokmakoff and co-workers have reported this in HOD/D_2O experiments indicating arises from an altered hydrogen bonding network where the ν_{OD} mode relaxes into a “hot” ground state [26, 31].

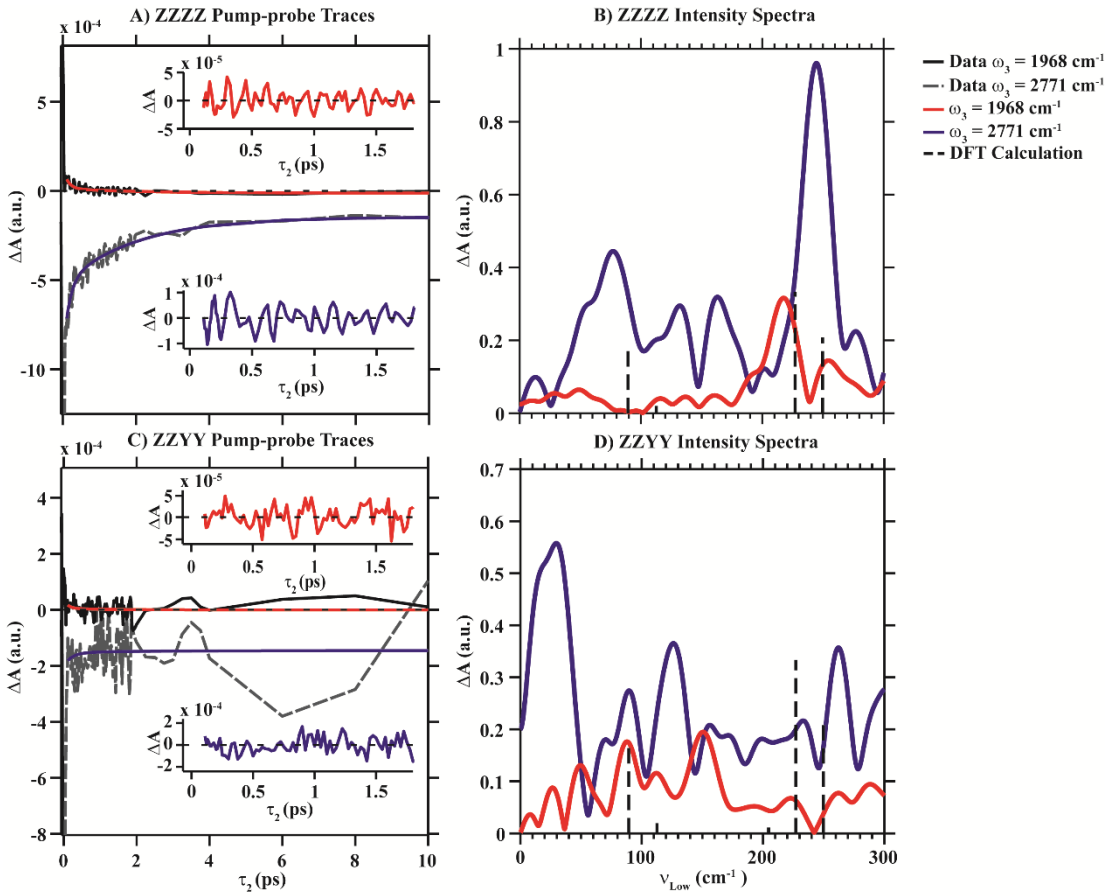

Figure 4.4.3: Polarization selective pump-probe traces and coupled low frequency modes of HBQ. **A)** The pump-probe traces at 1968 and 2771 cm^{-1} as indicated by the dashed-blue line in Figure 4.4.2A. These traces were chosen as they represent the fundamental and overtone spectral regions of the pump-probe spectrum. The black-solid line and red-solid line for the 1968 cm^{-1} frequency trace are the original data and exponential fit, respectively. Likewise, the grey-dashed line and blue-solid line for the 2771 cm^{-1} frequency trace are the original data and exponential fit, respectively. The residual for each trace is shown as an inset to **A**. The red-solid line in the upper inset is the residual for the 1968 cm^{-1} trace and blue-solid line in the lower inset is the residual for the 2771 cm^{-1} trace. **B)** The intensity spectra of the trace along 1968 and 2771 cm^{-1} calculated from the FFT of the residual in the insets in **A**. The red-solid line is the intensity spectrum for the 1968 cm^{-1} trace, and the blue solid-line is the intensity spectrum for the 2771 cm^{-1} trace. The black-dashed sticks indicate harmonic frequency calculation (See Table 4.4.1). **C** and **D** represents the same treatment for the ZZYY response shown in Figure 4.4.2 **B**.

Additionally the residuals of the fits in the fundamental region demonstrate a strong oscillatory component (Figure 4.4.2A). Figures 4.4.3 B and D show the spectra from the FFT of these residuals. The ZZZZ residual spectrum show an anharmonically coupled low frequency mode at 248 cm^{-1} (see Figure 4.4.2 B). Furthermore, previous studies have measured the low frequency solvent modes of CCl_4 at 218, 315, and 464 cm^{-1} indicating the low frequency modes shown here

are not a result of the solvent [33, 34]. The lack of coupling to the 248 cm^{-1} low frequency mode in ZZYY Figure 4.4.3 D indicates that these modes occur in the same plane as the ν_{OH} mode. This is in agreement with the displacement vectors calculated by DFT for these vibrational modes (see Figure 4.4.4 B)

Figure 4.4.4A clearly exhibits coupling to low frequency modulation at 248 cm^{-1} to the fundamental region of the vibrational response.

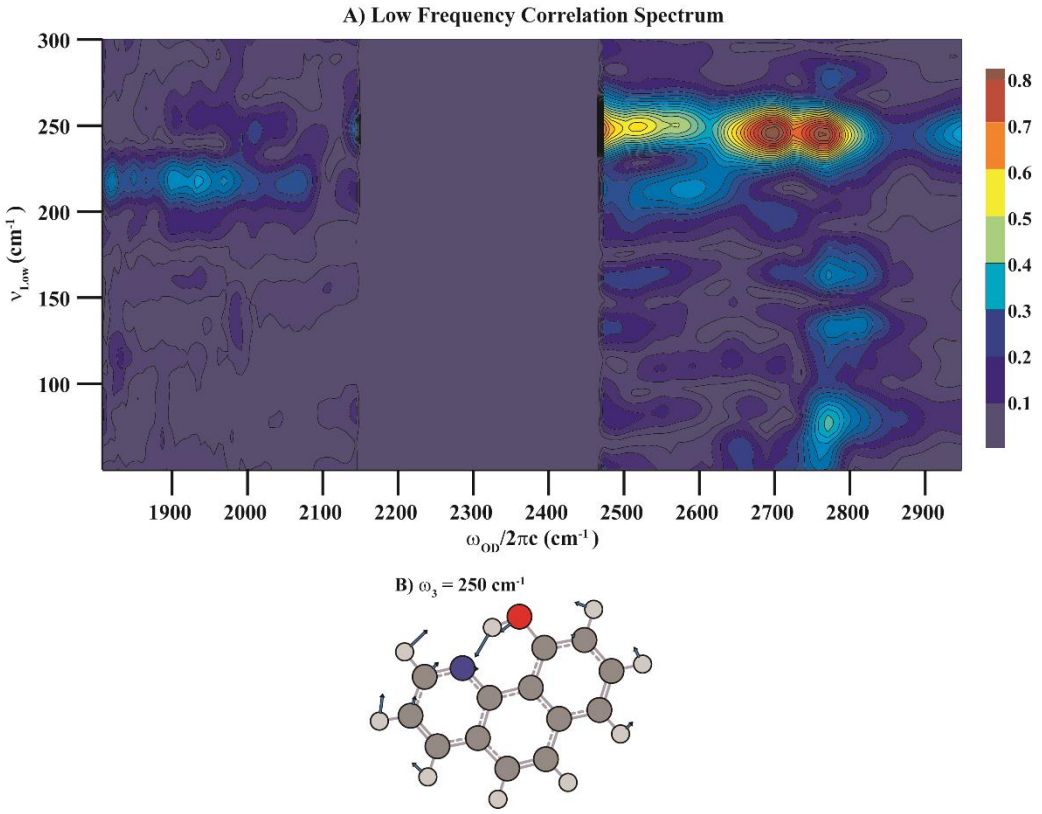

Figure 4.4.4: A) Correlation spectrum of HBQ indicating correlation of many high frequency modes with the low frequency modulation at 248 cm^{-1}. **B)** A low frequency mode of HBQ at 250 cm^{-1} with displacement vectors that contributes to the correlation spectrum **A** as indicated by the coupling strength in Table 4.4.2.

Like the anti-correlation seen in the DOAr-Py, there seems to a weak anti-correlation in the HBQ complex. The HBQ complex has significant rigidity due to the π-bonding and planar structure much like the DOAr-Py complex which likely plays a major role in how the structural dynamics affects the ν_{OH} vibrational dynamics. Additionally, the strong presence of the correlation of the

248 cm^{-1} mode to the fundamental transition mode suggests possible anharmonic coupling of the hydrogen bonding vibrations which has been seen in strong hydrogen-bonding systems by Cheatum and co-workers[35] as well as Petersen *et al*. The overtone transition region of the correlation spectrum suggests coupling to different low frequency modes such as a 212 cm^{-1} mode listed in Table 4.4.1. Table 4.4.2 suggests strong coupling to a mode at 207 cm^{-1}, however, it is difficult to discern this from the 217 cm^{-1} mode of CCl_4. For that reason, that mode was not further analyzed or discussed. However, the lack of coupling to the same mode in both the fundamental and overtone regions of HBQ is a departure from the DOAr-Py though similar to the trend observed in DOAr-ND_2 where the overtone region is coupled to a lower frequency structural modulation.

The anharmonic frequency calculations show a possible corresponding modulation at 250 cm^{-1} for the model system. The calculations indicate a 'cogwheel' like symmetric in-plane bend providing the bond between the phenol and amine as the backbone for a breathing motion. The anharmonic calculations provided cubic off-diagonal coupling terms of low frequency structural modes to the high frequency ν_{OH} mode. Tables 4.4.1 and 4.4.2 highlights the low frequency modes that are highly coupled to the ν_{OD} mode and contribute to the correlation spectrum shown in Figure 4.4.3A. The anharmonic frequency calculation for the structure yielded a ν_{OH} fundamental frequency of 2882 cm^{-1} (Table 4.4.1). Additionally, using the appropriate scaling factor of 0.968 further reduces the calculated fundamental frequency to 2766 cm^{-1} which closely matches the fundamental frequency of the FTIR at 2736 cm^{-1} (Refer to Chapter 2 Section 7 for additional scaling factor information) [36].

Table 4.4.1: Description of the frequency calculation of HBQ with the harmonic (ω_0) and anharmonic correction (ω). (ip = in-plane, oop = out-of-plane)

Mode Type	Mode	$\omega_{0,j}$ (cm^{-1})	ω_j (cm^{-1})
'Butterfly', Symmetric oop bend	1	89.30	92.90
τ(PhOH)/t(-Py) Structural torsion	2	112.63	114.05
β(PhOH)/β(-Ph) Symmetric oop bend	3	204.55	207.70
β(-Py) Symmetric oop bend	4	227.04	227.77
'Cogwheel', Symmetric ip bend	5	249.75	249.75
β(PhOH)/b(-Py) Asymmetric oop bend	6	286.90	292.59
H-bond shearing, Asymmetric ip bend	7	388.95	388.95
OH Stretch	66	3212.56	2881.85

As mentioned the most intense anharmonically coupled low frequency structural modulation is 248 cm^{-1}. The calculations indicate a 250 cm^{-1} frequency mode is coupled with an off-diagonal force constant of -11.939 cm^{-1} and within the pump spectrum bandwidth (Table 4.2). This also matches the vibrational analysis of the transient absorption data of Chou and workers, as previously mentioned.

Table 4.4.2: Cubic coupling constants ϕ_{ijk} (cm^{-1}) from anharmonic frequency calculation of the low frequency modes in HBQ and ν_{OH} (66) mode are shown. The mode of interest 5 corresponds to the 250 cm^{-1} structural modes in Table 4.4.1, respectively.

Mode (*i* = 66)		***J***							
		1	**2**	**3**	**4**	**5**	**6**	**7**	**66**
k	**1**	-	-	-	-	-	-	-	-10.968
	2		-	-	-	-	-	-	-45.092
	3			-	-	-	-	-	-34.550
	4				-	-	-	-	33.764
	5					-	-	-	-11.939
	6						-	-	33.750
	7							-	-29.473
	66								-

4.5 Pump-probe Results of DBQ

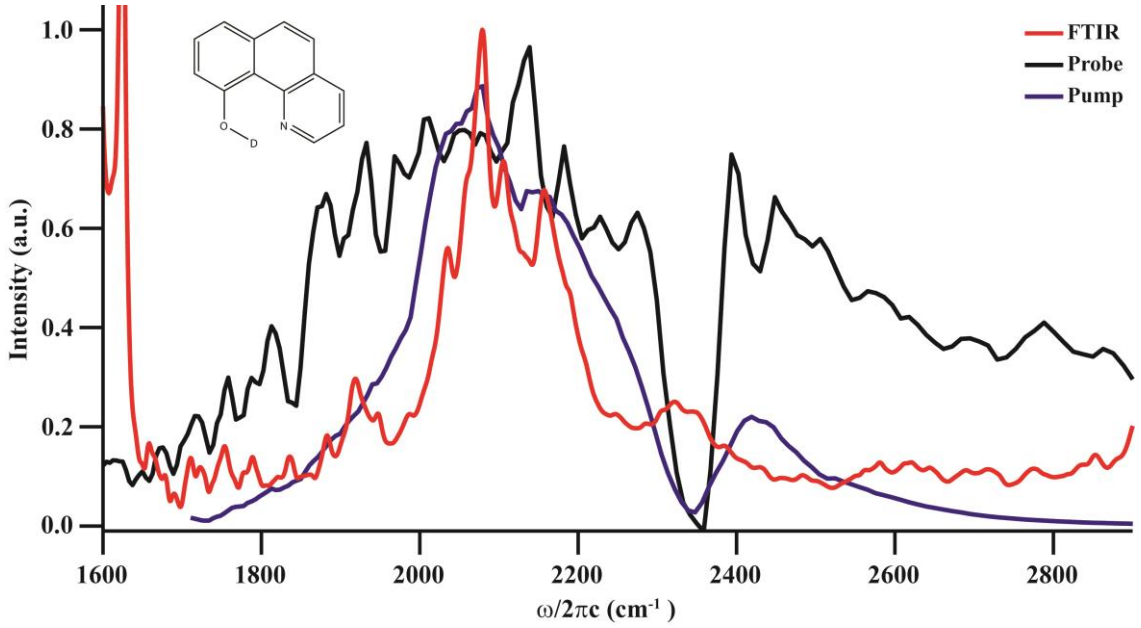

Figure 4.5.1: Normalized FTIR spectrum of the DBQ compound in the range of interest in red. The solid black line is a trace of the broadband mid-IR spectral content of the probe used during the pump-probe experiment. The solid blue line is a spectrum of the mid-IR pump-field. The inset is of the HBQ structure.

The FTIR spectra of the DBQ sample shows a broad line shape centered in the 1900-2300 cm^{-1} range attributed to the ν_{OD} stretch (see Figure 4.5.1). As indicated figure 4.5.1 and unlike the previous three pump-probe studies, the mid-IR pump-field does contain enough spectral content to pump the entire region of the ν_{OD} stretch. The BBIR probe-field allows us monitor the entire fundamental transition and overtone transition of the ν_{OD} region in addition to adjacent spectral information. The line-shape in this region has significant structure which makes it difficult to decipher the underlying dynamics which give rise to broad features and multiple peaks. The pump-probe measurements provide a window to view the dynamics in more detail.

The parallel (ZZZZ) and crossed (ZZYY) pump-probe spectra as a function of the detection frequency at various time delays are shown in Figure 4.5.2. The bleach (negative peak) is centered at the peak of the IR transition and the excited state absorption (positive peak) is centered at the

transition from the ν=1 to the ν=2 state. The ground state bleach and excited state absorption peaks shown in figure 4.5.2 A at τ_2 = 0 fs were fit with a Gaussian function of floating width for the fundamental transition and the overtone transition of each local mode. For DBQ the fundamental transition was determined to be 2072 cm^{-1} and the corresponding overtone 1751 cm^{-1}. The DBQ complex exhibits a single broad OD mode which gives rise to an anharmonicity of 320 cm^{-1}. This anharmonicity value is significantly larger than the 180 to 235 cm^{-1} range reported by Rospenk *et al*. for phenol•pyridine complexes in carbon tetrachloride.[23] Similar studies[24, 25] have shown that strong hydrogen bond formation increases the anharmonicity for the ν_{OD} stretch.

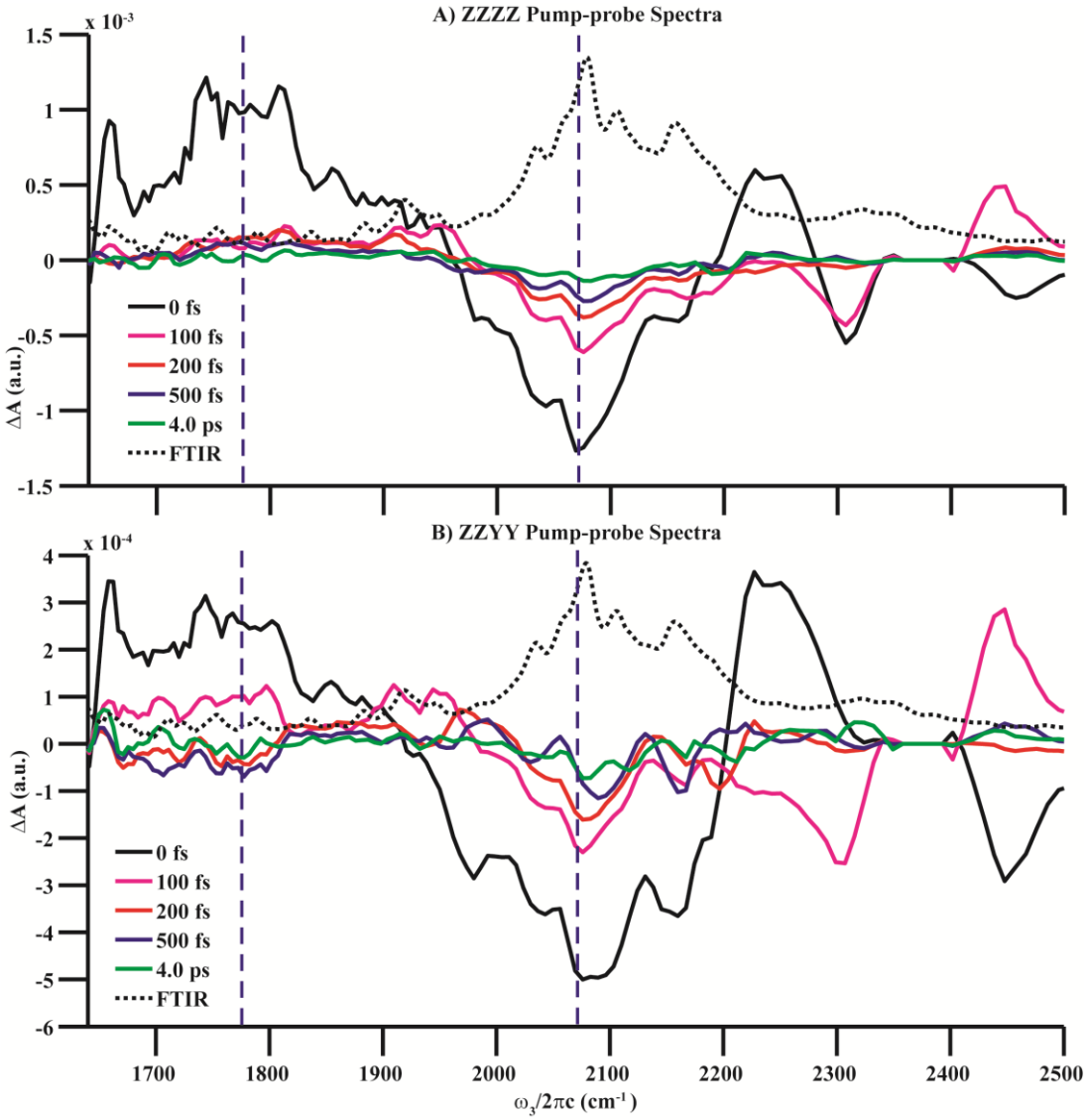

Figure 4.5.2: Polarization selective pump-probe spectra of DBQ. **A)** The ZZZZ pump-probe spectra of DBQ at selected τ_2 points of 0, 100, 200, 500, and 4000 fs. **B)** The ZZZZ pump-probe spectra of DBQ at selected τ_2 points of 0, 100, 200, 500, and 4000 fs. The FTIR of HBQ in both of the ZZZZ and ZZYY spectra were scaled to 1.2× the amplitude of the respective overtone transitions at τ_2 = 0 fs. The blue-dashed lines represent the frequency of the traces shown if Figure 4.5.3 for both the ZZZZ and ZZYY pump-probe spectra.

The isotropic pump-probe trace for DBQ at the fundamental, 2069 cm^{-1}, was fit with a two exponentials of 170 fs and 2.7 ps. Details of how the isotropic response is calculated from the parallel (ZZZZ) and crossed (ZZYY) datasets shown in Figure 3.6.2 is described in Chapter 2 Section 6. The reorganizational motions associated with molecular rotations have been removed

in the isotropic response allowing for a more accurate portrayal of the ν_{OD} population dynamics [26]. The overtone at 1753 cm^{-1} exhibited somewhat faster dynamics with an initial decay of 98 fs and longer decay of 1.1 ps. These fits were typical results for their respective spectral region. These two component decay rates are typical of strong hydrogen bonding systems such as those by the $\nu_{OH/OD}$ mode in D_2O/HOD vibrational relaxation experiments as previously described above in Section 4 [26-32].

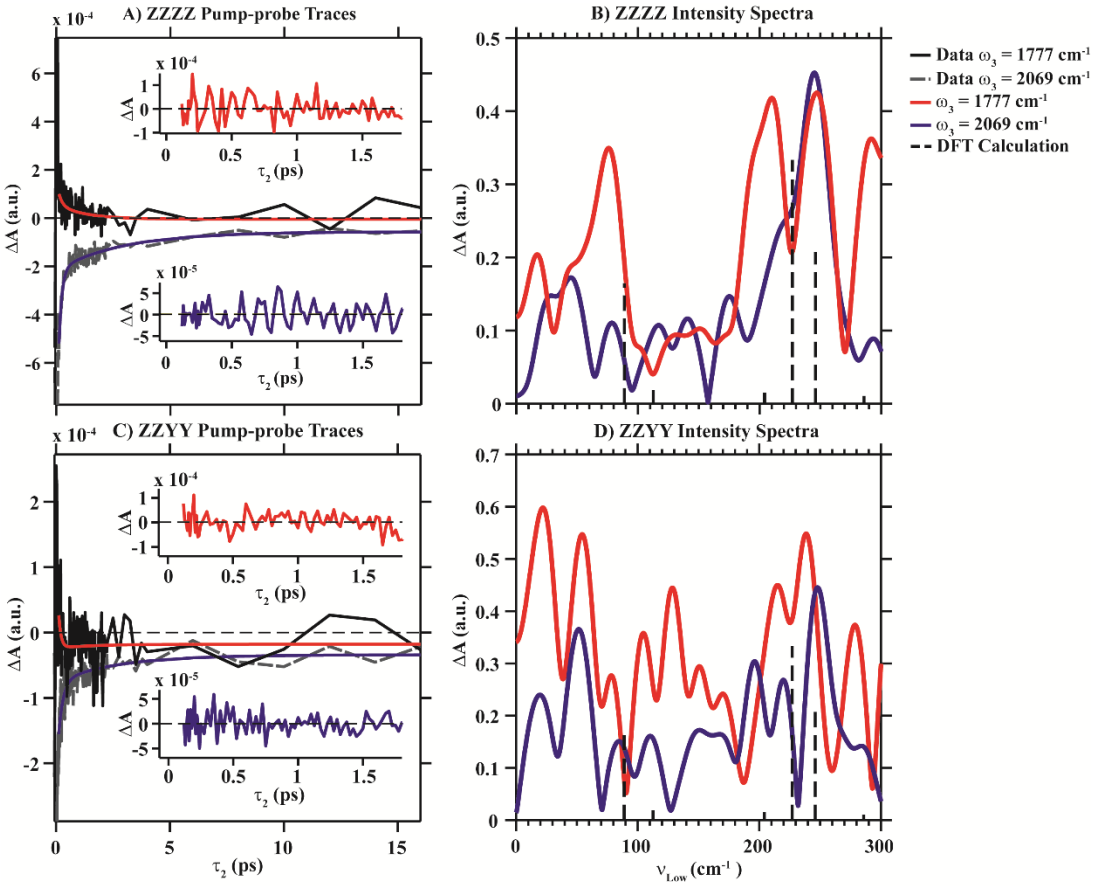

Figure 4.5.3: Polarization selective pump-probe traces and coupled low frequency modes of DBQ. **A)** The ZZZZ pump-probe traces at 1777 and 2069 cm^{-1} as indicated by the dashed-blue line in Figure 4.5.1A. These traces were chosen as they closely align with the fundamental and overtone frequencies from the Gaussian fit of the pump-probe spectrum. The black-solid line and red-solid line for the 1777 cm^{-1} frequency trace are the original data and exponential fit, respectively. Likewise, the grey-dashed line and blue-solid line for the 2069 cm^{-1} frequency trace are the original data and exponential fit, respectively. The residual for each trace is shown as an inset to **A**. The red-solid line in the upper inset is the residual for the 1777 cm^{-1} trace and blue-solid line in the lower inset is the residual for the 2069 cm^{-1} trace. **B)** The intensity spectra of the trace along 1777 and 2069 cm^{-1} calculated from the Fast Fourier-Transform of the residual in the insets in **A**. The red-solid line is the intensity spectrum for the 1777 cm^{-1} trace, and the blue solid-line is the intensity spectrum for the 2069 cm^{-1} trace. The black-dashed sticks indicate the DFT harmonic frequency calculation (See Table 3.5.1). **C** and **D** represent the same treatment for the ZZYY pump-probe data shown in Figure 4.5.2B.

Additionally the residuals of the fits in the fundamental region demonstrate a strong oscillatory component (Figure 4.5.2A). Figures 4.5.3 B and D show the spectrum from the FT of these residuals. The ZZZZ residual spectrum shows an anharmonically coupled low frequency mode at 245 cm^{-1}. Furthermore, previous studies have measured the low frequency solvent modes of CCl_4

at 218, 315, and 464 cm^{-1} indicating the low frequency mode shown here is not a result of the solvent [33, 34]. The weak coupling to the 245 cm^{-1} low frequency mode in ZZYY Figure 3.6.3 D indicates that these modes occur in the same plane as the ν_{OD} mode. This is in agreement with the displacement vectors calculated by DFT for these vibrational modes (see Figure 4.5.4 B)

The correlation spectra as a function of the low frequency modulations is shown in figure 4.5.4A is the result taking the FT of all residuals for the fundamental and overtone transitions.

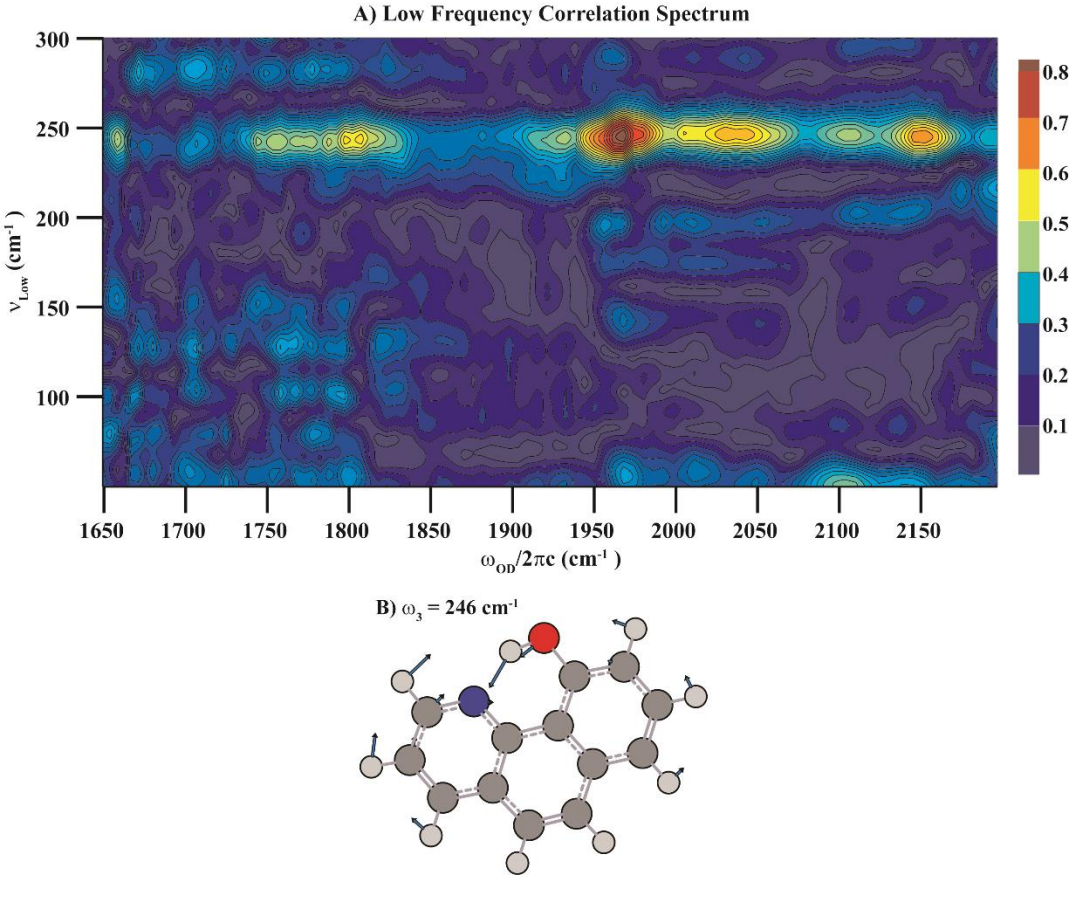

Figure 4.5.4: A) Isotropic correlation spectrum of DBQ indicating correlation of many high frequency modes with the low frequency structural mode at 245 cm^{-1}. **B)** A low frequency mode of DBQ at 246 cm^{-1} with displacement vectors that contributes to the correlation spectrum **A** as indicated by the coupling strength in Table 4.5.2.

The correlation spectrum clearly exhibits coupling to low frequency modulation at 245 cm^{-1} to both the fundamental and overtone spectral regions. Like the anti-correlation seen in HBQ and DOAr-Py (see Chapter 3 Section 4), DBQ also shows a weak anti-correlation. The DBQ complex

has significant rigidity due to the π-bonding and planar structure much like HBQ and DOAr-Py complex which plays a major role in how the structural dynamics affects the ν_{OD} vibrational dynamics. Additionally, the strong presence of the correlation of the 245 cm^{-1} mode to the fundamental mode suggests possible anharmonic coupling of the hydrogen bonding vibrations which has been seen in strong hydrogen-bonding systems by Cheatum and co-workers[35] as well as Petersen *et al*. The overtone spectral region of the correlation spectrum suggests coupling to additional low frequency modes such as 90 and 212 cm^{-1} mode listed in Table 4.5.1. Table 4.5.2 suggests strong coupling to a mode at 202 cm^{-1}, however, it is difficult to discern this from the 217 cm^{-1} mode of CCl_4. For that reason, that mode was not further analyzed or discussed. DBQ also shows strong coupling to additional different modes between the fundamental and overtone transitions. This behavior by DBQ is a departure from the DOAr-Py though similar to the trend observed in HBQ and DOAr-ND_2 (see Chapter 3 Section 6) where the overtone spectral region is coupled to additional lower frequency structural modulations.

The DFT calculations show a possible corresponding modulation at 245 cm^{-1} for the model system. The calculations indicate a 'cogwheel' like symmetric in-plane bend providing the bond between the phenol and amine as the backbone for a breathing motion. The anharmonic calculations provided cubic off-diagonal coupling terms of low frequency structural modes to the high frequency ν_{OD} mode. Table 4.5.1 and 4.5.2 highlights the low frequency modes that are coupled to the ν_{OD} mode and contribute to the correlation spectrum shown in Figure 4.5.4 A. The anharmonic frequency calculation for the structure yielded a ν_{OD} fundamental frequency of 2161 cm^{-1} (Table 4.5.1). Additionally, using the appropriate scaling factor of 0.968 further reduces the calculated fundamental frequency to 2074 cm^{-1} which very closely matches the fundamental frequency of the IR at 2072 cm^{-1} (Refer to Chapter 2 Section 7) [36].

Table 4.5.1: Description of the frequency calculation of DBQ with the harmonic (ω_0) and anharmonic correction (ω).

Mode Type	Mode	$\omega_{0,j}$ (cm^{-1})	ω_j (cm^{-1})
Butterfly', Symmetric oop bend	1	88.86	92.04
τ(PhOH)/t(-Py) Structural torsion	2	112.62	114.57
β(PhOH)/β(-Ph) Symmetric oop bend	3	204.17	207.11
β(-Py) Symmetric oop bend	4	227.00	226.80
Cogwheel', Symmetric ip bend	5	246.02	246.02
β(PhOH)/b(-Py) Asymmetric oop bend	6	285.83	291.38
H-bond shearing, Asymmetric ip bend	7	382.62	382.62
OD Stretch	58	2342.18	2161.65

As mentioned the most intense coupled low frequency mode is at 245 cm^{-1}. The calculations indicate a 246 cm^{-1} frequency mode is coupled with an off-diagonal force constant of 1.980 cm^{-1} and within the pump spectrum bandwidth (Table 4.5.2). The phenyl backbone for the HBQ and DBQ may limit the degree of coupling of low frequency modulations to the ν_{OH}/ν_{OD} mode which may explain the calculations in Table 4.4.2 and Table 4.5.2 showing no diagonal coupling constants for the third-order anharmonic frequency calculations. However, this low frequency mode matches the vibrational analysis of the transient absorption data of Chou and workers, as previously mentioned.

Table 4.5.2: Cubic coupling constants ϕ_{ijk} (cm^{-1}) from anharmonic frequency calculation of the low frequency modes in DBQ and ν_{OD} (58) mode are shown. The mode of interest 5 corresponds to the 246 cm^{-1} structural modes in Table 4.5.1, respectively.

Mode (*i* = 58)		***J***							
		1	**2**	**3**	**4**	**5**	**6**	**7**	**58**
k	**1**	-	-	-	-	-	-	-	-12.126
	2		-	-	-	-	-	-	-7.426
	3			-	-	-	-	-	21.727
	4				-	-	-	-	12.990
	5					-	-	-	1.980
	6						-	-	-8.320
	7							-	-14.374
	58								-

4.6 Concluding Remarks

Due to the complexity of the lineshapes in the pump-probe measurements, also reflected in the FTIR spectra, it is difficult to give much detail about the vibrational landscape. In other similar systems exhibiting strong hydrogen bonding, the structure has been attributed to Franck-Condon like overlap induced by anharmonic coupling through low frequency structural modes giving rise to broad lineshapes with complex structure [33]. These features have also been attributed to Fermi-resonance coupling of the ν_{OD} mode to the overtones [35, 37]. While neither explanation can be excluded, the correlation of the ν_{OD} stretch with the low frequency mode in the HBQ and DBQ complex strongly suggests anharmonic coupling through low frequency structural modes gives rise to these broad lineshapes. Furthermore, the anti-correlation of the high frequency mode and low frequency mode gives more credence to this hypothesis by providing a broad environment for the ν_{OH}/ν_{OD} stretch to sample through strong OD···N hydrogen-bonding of the adjacent pyridine as suggested by fast kinetic rates and large anharmonicity. Our observations coincide with the vibrational analysis of the data collected by Chou and co-workers in which they point to a vibrational mode between 230 and 250 cm^{-1} as having a significant impact on the ESIPT.

We also notice similar trends between the HBQ and DBQ which was also prevalent in Chou and co-workers data such as similar ν_{OH}/ν_{OD} lifetimes as well as similar coupling to low frequency modes. The main contrast between the HBQ and DBQ arises from different coupling in the overtone region of the ν_{OH}/ν_{OD}. This may arise from the overlap with the CO_2 absorption which occupies a significant region within the overtone and fundamental region of HBQ that we are unable to access. This lack of information does limit the conclusions we can make about possible coupling. However, the information we do have does clearly indicate very strong anharmonic coupling to low frequency structural modulations that likely play a major role in the

proton transfer mechanism of ESIPT reactions. Ultrafast visible-pump IR-probe experiments may yield information about the proton transfer and electron transfer.

References

1. Wenger, O.S., *Proton-coupled electron transfer with photoexcited ruthenium(II), rhenium(I), and iridium(III) complexes.* Coordination Chemistry Reviews, 2015. **282–283**(0): p. 150-158.
2. Sytnik, A. and M. Kasha, *Excited-state intramolecular proton transfer as a fluorescence probe for protein binding-site static polarity.* Proceedings of the National Academy of Sciences, 1994. **91**(18): p. 8627-8630.
3. Sytnik, A., D. Gormin, and M. Kasha, *Interplay between excited-state intramolecular proton transfer and charge transfer in flavonols and their use as protein-binding-site fluorescence probes.* Proceedings of the National Academy of Sciences, 1994. **91**(25): p. 11968-11972.
4. Demchenko, A.P. and A.I. Sytnik, *Solvent reorganizational red-edge effect in intramolecular electron transfer.* Proceedings of the National Academy of Sciences, 1991. **88**(20): p. 9311-9314.
5. Brand, L. and J.R. Gohlke, *Fluorescence Probes for Structure.* Annual Review of Biochemistry, 1972. **41**(1): p. 843-868.
6. Barbara, P.F., P.K. Walsh, and L.E. Brus, *Picosecond kinetic and vibrationally resolved spectroscopic studies of intramolecular excited-state hydrogen atom transfer.* The Journal of Physical Chemistry, 1989. **93**(1): p. 29-34.
7. Chou, P.-T. and C.-Y. Wei, *Photophysics of 10-Hydroxybenzo[h]quinoline in Aqueous Solution.* The Journal of Physical Chemistry, 1996. **100**(42): p. 17059-17066.
8. Markle, T.F., et al., *Probing concerted proton–electron transfer in phenol–imidazoles.* Proceedings of the National Academy of Sciences, 2008. **105**(24): p. 8185-8190.
9. Markle, T.F. and J.M. Mayer, *Concerted Proton–Electron Transfer in Pyridylphenols: The Importance of the Hydrogen Bond.* Angewandte Chemie International Edition, 2008. **47**(4): p. 738-740.
10. Rhile, I.J., et al., *Concerted Proton−Electron Transfer in the Oxidation of Hydrogen-Bonded Phenols.* Journal of the American Chemical Society, 2006. **128**(18): p. 6075-6088.
11. Tommos, C. and G.T. Babcock, *Proton and hydrogen currents in photosynthetic water oxidation.* Biochimica et Biophysica Acta (BBA) - Bioenergetics, 2000. **1458**(1): p. 199-219.
12. Westlake, B.C., et al., *Concerted electron-proton transfer in the optical excitation of hydrogen-bonded dyes.* Proceedings of the National Academy of Sciences, 2011. **108**(21): p. 8554-8558.
13. Kühne, H. and G.W. Brudvig, *Proton-Coupled Electron Transfer Involving Tyrosine Z in Photosystem II†.* The Journal of Physical Chemistry B, 2002. **106**(33): p. 8189-8196.
14. Faller, P., et al., *Resolving intermediates in biological proton-coupled electron transfer: A tyrosyl radical prior to proton movement.* Proceedings of the National Academy of Sciences, 2003. **100**(15): p. 8732-8735.

15. Siegbahn, P.E.M., *Structures and Energetics for O2 Formation in Photosystem II.* Accounts of Chemical Research, 2009. **42**(12): p. 1871-1880.
16. Sjödin, M., et al., *The mechanism for proton-coupled electron transfer from tyrosine in a model complex and comparisons with Y(Z) oxidation in photosystem II.* Philosophical Transactions of the Royal Society B: Biological Sciences, 2002. **357**(1426): p. 1471-1511.
17. Chou, P.-T., et al., *Excited-State Intramolecular Proton Transfer in 10-Hydroxybenzo[h]quinoline.* The Journal of Physical Chemistry A, 2001. **105**(10): p. 1731-1740.
18. Kubicki, M., T. Borowiak, and W.Z. Antkowiak, *10-Hydroxybenzo[h]quinoline.* Acta Crystallographica Section C, 1995. **51**(6): p. 1173-1175.
19. Hammes-Schiffer, S. and A.V. Soudackov, *Proton-Coupled Electron Transfer in Solution, Proteins, and Electrochemistry†.* The Journal of Physical Chemistry B, 2008. **112**(45): p. 14108-14123.
20. Soudackov, A., E. Hatcher, and S. Hammes-Schiffer, *Quantum and dynamical effects of proton donor-acceptor vibrational motion in nonadiabatic proton-coupled electron transfer reactions.* The Journal of Chemical Physics, 2005. **122**(1): p. 014505.
21. Elsaesser, T., H. Lobentanzer, and A. Seilmeier, *Generation of tunable picosecond pulses in the medium infrared by down-conversion in AgGaS2.* Optics Communications, 1985. **52**(5): p. 355-359.
22. Cerullo, G. and S. De Silvestri, *Ultrafast optical parametric amplifiers.* Review of Scientific Instruments, 2003. **74**(1): p. 1-18.
23. Rospenk, M. and T. Zeegers-Huyskens, *FT-IR (7500−1800 cm-1) Study of Hydrogen-Bond Complexes between Phenols−OH(OD) and Pyridine. Evidence of Proton Transfer in the Second Vibrational Excited State.* The Journal of Physical Chemistry A, 1997. **101**(45): p. 8428-8434.
24. Asselin, M. and C. Sandorfy, *A low temperature infrared study of the band-width and frequency in self-associated alcohols.* Chemical Physics Letters, 1971. **8**(6): p. 601-603.
25. Asselin, M. and C. Sandorfy, *Double Excitation in the Infrared Spectra of Self-Associated Alcohols.* The Journal of Chemical Physics, 1970. **52**(12): p. 6130-6134.
26. Nicodemus, R.A., et al., *Collective Hydrogen Bond Reorganization in Water Studied with Temperature-Dependent Ultrafast Infrared Spectroscopy.* The Journal of Physical Chemistry B, 2011. **115**(18): p. 5604-5616.
27. Lock, A.J. and H.J. Bakker, *Temperature dependence of vibrational relaxation in liquid H2O.* The Journal of Chemical Physics, 2002. **117**(4): p. 1708-1713.
28. Nibbering, E.T.J. and T. Elsaesser, *Ultrafast Vibrational Dynamics of Hydrogen Bonds in the Condensed Phase.* Chemical Reviews, 2004. **104**(4): p. 1887-1914.
29. Rini, M., et al., *Femtosecond mid-infrared spectroscopy of condensed phase hydrogen-bonded systems as a probe of structural dynamics.* Faraday Discussions, 2003. **122**(0): p. 27-40.
30. Nienhuys, H.-K., et al., *Mechanism for vibrational relaxation in water investigated by femtosecond infrared spectroscopy.* The Journal of Chemical Physics, 1999. **111**(4): p. 1494-1500.
31. Loparo, J.J., et al., *Reorientational and configurational fluctuations in water observed on molecular length scales.* Physical Review B, 2004. **70**(18): p. 180201.
32. Fecko, C.J., et al., *Ultrafast Hydrogen-Bond Dynamics in the Infrared Spectroscopy of Water.* Science, 2003. **301**(5640): p. 1698-1702.

33. Petersen, P.B., et al., *Ultrafast N−H Vibrational Dynamics of Cyclic Doubly Hydrogen-Bonded Homo- and Heterodimers.* The Journal of Physical Chemistry B, 2008. **112**(42): p. 13167-13171.
34. Moore, P., et al., *The low frequency density of states and vibrational population dynamics of polyatomic molecules in liquids.* The Journal of Chemical Physics, 1995. **103**(9): p. 3325-3334.
35. Gündoğdu, K., et al., *Relaxation and anharmonic couplings of the O–H stretching vibration of asymmetric strongly hydrogen-bonded complexes.* The Journal of Chemical Physics, 2007. **127**(4): p. 044501.
36. Alecu, I.M., et al., *Computational Thermochemistry: Scale Factor Databases and Scale Factors for Vibrational Frequencies Obtained from Electronic Model Chemistries.* Journal of Chemical Theory and Computation, 2010. **6**(9): p. 2872-2887.
37. Dwyer, J.R., et al., *Ultrafast dynamics of vibrational N–H stretching excitations in the 7-azaindole dimer.* Chemical Physics Letters, 2006. **432**(1–3): p. 146-151.

BIBLIOGRAPHY

1. Alecu, I.M., et al., *Computational Thermochemistry: Scale Factor Databases and Scale Factors for Vibrational Frequencies Obtained from Electronic Model Chemistries.* Journal of Chemical Theory and Computation, 2010. **6**(9): p. 2872-2887.
2. Allerhand, A. and P. von R. Schleyer, *Solvent Effects in Infrared Spectroscopic Studies of Hydrogen Bonding.* Journal of the American Chemical Society, 1963. **85**(4): p. 371-380.
3. Andrews, B., A. Anderson, and B. Torrie, *Raman and infrared spectra of crystalline chloroform.* Chemical Physics Letters, 1984. **104**(1): p. 65-70.
4. apos, et al., *Infrared Spectra in Polarized Light of Crystalline Chloroform.* The Journal of Chemical Physics, 1972. **57**(10): p. 4136-4142.
5. Asselin, M. and C. Sandorfy, *Double Excitation in the Infrared Spectra of Self-Associated Alcohols.* The Journal of Chemical Physics, 1970. **52**(12): p. 6130-6134.
6. Asselin, M. and C. Sandorfy, *A low temperature infrared study of the band-width and frequency in self-associated alcohols.* Chem. Phys. Lett., 1971. **8**: p. 601.
7. Asselin, M. and C. Sandorfy, *A low temperature infrared study of the band-width and frequency in self-associated alcohols.* Chemical Physics Letters, 1971. **8**(6): p. 601-603.
8. Backus, S., et al., *High power ultrafast lasers.* Review of Scientific Instruments, 1998. **69**(3): p. 1207-1223.
9. Barbara, P.F., P.K. Walsh, and L.E. Brus, *Picosecond kinetic and vibrationally resolved spectroscopic studies of intramolecular excited-state hydrogen atom transfer.* The Journal of Physical Chemistry, 1989. **93**(1): p. 29-34.
10. Barone, V., *Vibrational zero-point energies and thermodynamic functions beyond the harmonic approximation.* The Journal of Chemical Physics, 2004. **120**(7): p. 3059-3065.
11. Barry, B.A., *Reaction dynamics and proton coupled electron transfer: Studies of tyrosine-based charge transfer in natural and biomimetic systems.* Biochimica et Biophysica Acta (BBA) - Bioenergetics, 2015. **1847**(1): p. 46-54.
12. Berg, J.M., J.L. Tymoczko, and L. Stryer, *Biochemistry*. 2010: W. H. Freeman.
13. Blair, D.F., et al., *Spectroelectrochemical study of cytochrome c oxidase: pH and temperature dependences of the cytochrome potentials. Characterization of site-site interactions.* Journal of Biological Chemistry, 1986. **261**(25): p. 11524-11537.
14. Brand, L. and J.R. Gohlke, *Fluorescence Probes for Structure.* Annual Review of Biochemistry, 1972. **41**(1): p. 843-868.
15. Brookes, J.F., et al., *Effect of Solvent Polarity on the Vibrational Dephasing Dynamics of the Nitrosyl Stretch in an FeII Complex Revealed by 2D IR Spectroscopy.* The Journal of Physical Chemistry A, 2013. **117**(29): p. 6234-6243.
16. Cerullo, G. and S. De Silvestri, *Ultrafast optical parametric amplifiers.* Review of Scientific Instruments, 2003. **74**(1): p. 1-18.
17. Cheng, M., et al., *Generation of tunable octave-spanning mid-infrared pulses by filamentation in gas media.* Optics Letters, 2012. **37**(11): p. 1787-1789 KW - Ultrafast nonlinear optics KW - Spectroscopy, infrared KW - Pulses KW - Ultrafast phenomena UR - http://ol.osa.org/abstract.cfm?URI=ol-37-11-1787.
18. Chilla, J.L.A. and O.E. Martinez, *Direct determination of the amplitude and the phase of femtosecond light pulses.* Optics Letters, 1991. **16**(1): p. 39-41.

19. Chou, P.-T., et al., *Excited-State Intramolecular Proton Transfer in 10-Hydroxybenzo[h]quinoline.* The Journal of Physical Chemistry A, 2001. **105**(10): p. 1731-1740.
20. Chou, P.-T. and C.-Y. Wei, *Photophysics of 10-Hydroxybenzo[h]quinoline in Aqueous Solution.* The Journal of Physical Chemistry, 1996. **100**(42): p. 17059-17066.
21. Cook, D.J. and R.M. Hochstrasser, *Intense terahertz pulses by four-wave rectification in air.* Optics Letters, 2000. **25**(16): p. 1210-1212 KW - Nonlinear optics, four-wave mixing KW - Infrared, far KW - Ultrafast nonlinear optics KW - Ultrafast technology UR - http://ol.osa.org/abstract.cfm?URI=ol-25-16-1210.
22. Cukier, R.I., *Mechanism for Proton-Coupled Electron-Transfer Reactions.* The Journal of Physical Chemistry, 1994. **98**(9): p. 2377-2381.
23. Cukier, R.I. and D.G. Nocera, *PROTON-COUPLED ELECTRON TRANSFER.* Annual Review of Physical Chemistry, 1998. **49**(1): p. 337-369.
24. Demchenko, A.P. and A.I. Sytnik, *Solvent reorganizational red-edge effect in intramolecular electron transfer.* Proceedings of the National Academy of Sciences, 1991. **88**(20): p. 9311-9314.
25. Dwyer, J.R., et al., *Ultrafast dynamics of vibrational N–H stretching excitations in the 7-azaindole dimer.* Chemical Physics Letters, 2006. **432**(1–3): p. 146-151.
26. Elsaesser, T., et al., *Ultrafast vibrational dynamics and anharmonic couplings of hydrogen-bonded dimers in solution.* Chemical Physics, 2007. **341**(1–3): p. 175-188.
27. Elsaesser, T., H. Lobentanzer, and A. Seilmeier, *Generation of tunable picosecond pulses in the medium infrared by down-conversion in AgGaS2.* Optics Communications, 1985. **52**(5): p. 355-359.
28. Faller, P., et al., *Resolving intermediates in biological proton-coupled electron transfer: A tyrosyl radical prior to proton movement.* Proceedings of the National Academy of Sciences, 2003. **100**(15): p. 8732-8735.
29. Fayer, D., *Ultrafast Infrared And Raman Spectroscopy*. 2001: Taylor & Francis.
30. Fecko, C.J., et al., *Ultrafast Hydrogen-Bond Dynamics in the Infrared Spectroscopy of Water.* Science, 2003. **301**(5640): p. 1698-1702.
31. Fischer, H., *Radical Reaction Rates in Liquids*. Vol. II/13. 1983.
32. Fossey, J., D. Lefort, and J. Sorba, Free Radicals in Organic Chemistry, 1993.
33. Fourkas, J.T. and M.D. Fayer, *The transient grating: a holographic window to dynamic processes.* Accounts of Chemical Research, 1992. **25**(5): p. 227-233.
34. Fourkas, J.T., H. Kawashima, and K.A. Nelson, *Theory of nonlinear optical experiments with harmonic oscillators.* The Journal of Chemical Physics, 1995. **103**(11): p. 4393-4407.
35. Frisch, M.J., et al., *Gaussian 09*. 2009, Gaussian, Inc.: Wallingford, CT, USA.
36. Fuji, T. and T. Suzuki, *Generation of sub-two-cycle mid-infrared pulses by four-wave mixing through filamentation in air.* Optics Letters, 2007. **32**(22): p. 3330-3332 KW - Nonlinear optics, four-wave mixing KW - Infrared KW - Pulses UR - http://ol.osa.org/abstract.cfm?URI=ol-32-22-3330.
37. Fuller, F.D., et al., *Vibronic coherence in oxygenic photosynthesis.* Nat Chem, 2014. **6**(8): p. 706-711.
38. Gennis, R.B., *Multiple proton-conducting pathways in cytochrome oxidase and a proposed role for the active-site tyrosine.* Biochimica et Biophysica Acta (BBA) - Bioenergetics, 1998. **1365**(1–2): p. 241-248.

39. Gilli, P., et al., *Evidence for Intramolecular N−H···O Resonance-Assisted Hydrogen Bonding in β-Enaminones and Related Heterodienes. A Combined Crystal-Structural, IR and NMR Spectroscopic, and Quantum-Mechanical Investigation.* Journal of the American Chemical Society, 2000. **122**(42): p. 10405-10417.
40. Graener, H. and A. Laubereau, *Ultrafast overtone excitation for the study of vibrational population decay in liquids.* Chemical Physics Letters, 1983. **102**(1): p. 100-104.
41. Gündoğdu, K., et al., *Relaxation and anharmonic couplings of the O–H stretching vibration of asymmetric strongly hydrogen-bonded complexes.* The Journal of Chemical Physics, 2007. **127**(4): p. 044501.
42. Hammes-Schiffer, S. and A.V. Soudackov, *Proton-Coupled Electron Transfer in Solution, Proteins, and Electrochemistry†.* The Journal of Physical Chemistry B, 2008. **112**(45): p. 14108-14123.
43. Heyne, K., et al., J. Chem. Phys., 2004. **121**: p. 902.
44. Heyne, K., et al., *Coherent low-frequency motions of hydrogen bonded acetic acid dimers in the liquid phase.* The Journal of Chemical Physics, 2004. **121**(2): p. 902-913.
45. Huse, N., et al., *Anharmonic Couplings Underlying the Ultrafast Vibrational Dynamics of Hydrogen Bonds in Liquids.* Physical Review Letters, 2005. **95**(14): p. 147402.
46. Huse, N., et al., *Vibrational Multilevel Quantum Coherence due to Anharmonic Couplings in Intermolecular Hydrogen Bonds.* Physical Review Letters, 2003. **91**(19): p. 197401.
47. Iaconis, C. and I.A. Walmsley, *Spectral phase interferometry for direct electric-field reconstruction of ultrashort optical pulses.* Optics Letters, 1998. **23**(10): p. 792-794.
48. Ingold, K.U. and G.A. Russell, *Free Radicals*. 1973. 67ff.
49. Inoue, Y., et al., *Ethylene Polymerization Behavior of New Titanium Complexes Having Two Phenoxy-Pyridine Chelate Ligands.* Chemistry Letters, 2001. **30**(10): p. 1060-1061.
50. Kane, D.J. and R. Trebino, *Characterization of arbitrary femtosecond pulses using frequency-resolved optical gating.* Quantum Electronics, IEEE Journal of, 1993. **29**(2): p. 571-579.
51. Kitagawa, T. and T. Ogura, *Oxygen Activation Mechanism at the Binuclear Site of Heme–Copper Oxidase Superfamily as Revealed by Time-Resolved Resonance Raman Spectroscopy*, in *Progress in Inorganic Chemistry*. 2007, John Wiley & Sons, Inc. p. 431-479.
52. Kubicki, M., T. Borowiak, and W.Z. Antkowiak, *10-Hydroxybenzo[h]quinoline.* Acta Crystallographica Section C, 1995. **51**(6): p. 1173-1175.
53. Kühne, H. and G.W. Brudvig, *Proton-Coupled Electron Transfer Involving Tyrosine Z in Photosystem II†.* The Journal of Physical Chemistry B, 2002. **106**(33): p. 8189-8196.
54. Lee, K.F., et al., *Characterization of mid-infrared femtosecond pulses [Invited]*. Journal of the Optical Society of America B, 2008. **25**(6): p. A54-A62.
55. Linden, S., H. Giessen, and J. Kuhl, *XFROG — A New Method for Amplitude and Phase Characterization of Weak Ultrashort Pulses.* physica status solidi (b), 1998. **206**(1): p. 119-124.
56. Lock, A.J. and H.J. Bakker, *Temperature dependence of vibrational relaxation in liquid H2O.* The Journal of Chemical Physics, 2002. **117**(4): p. 1708-1713.
57. Loparo, J.J., et al., *Reorientational and configurational fluctuations in water observed on molecular length scales.* Physical Review B, 2004. **70**(18): p. 180201.

58. Lynch, M.S., et al., *Coherent Fifth-Order Visible–Infrared Spectroscopies: Ultrafast Nonequilibrium Vibrational Dynamics in Solution.* The Journal of Physical Chemistry A, 2012. **116**(26): p. 7023-7032.
59. Malmstroem, B.G., *Vectorial chemistry in bioenergetics: cytochrome c oxidase as a redox-linked proton pump.* Accounts of Chemical Research, 1993. **26**(6): p. 332-338.
60. Markle, T.F. and J.M. Mayer, *Concerted Proton–Electron Transfer in Pyridylphenols: The Importance of the Hydrogen Bond.* Angewandte Chemie International Edition, 2008. **47**(4): p. 738-740.
61. Markle, T.F., et al., *Probing concerted proton–electron transfer in phenol–imidazoles.* Proceedings of the National Academy of Sciences, 2008.
62. Markle, T.F., et al., *Probing concerted proton–electron transfer in phenol–imidazoles.* Proceedings of the National Academy of Sciences, 2008. **105**(24): p. 8185-8190.
63. Mayer, J.M., *PROTON-COUPLED ELECTRON TRANSFER: A Reaction Chemist's View.* Annual Review of Physical Chemistry, 2004. **55**(1): p. 363-390.
64. Mayer, J.M., *Simple Marcus-Theory-Type Model for Hydrogen-Atom Transfer/Proton-Coupled Electron Transfer.* The Journal of Physical Chemistry Letters, 2011. **2**(12): p. 1481-1489.
65. Moore, P., et al., *The low frequency density of states and vibrational population dynamics of polyatomic molecules in liquids.* The Journal of Chemical Physics, 1995. **103**(9): p. 3325-3334.
66. Mukamel, S., *Principles of Nonlinear Optical Spectroscopy*. 1999: Oxford University Press.
67. Neta, P., et al., *Solvent effects in the reactions of peroxyl radicals with organic reductants: evidence for proton-transfer-mediated electron transfer.* The Journal of Physical Chemistry, 1989. **93**(22): p. 7654-7659.
68. Nibbering, E.T.J. and T. Elsaesser, *Ultrafast Vibrational Dynamics of Hydrogen Bonds in the Condensed Phase.* Chemical Reviews, 2004. **104**(4): p. 1887-1914.
69. Nicodemus, R.A., et al., *Collective Hydrogen Bond Reorganization in Water Studied with Temperature-Dependent Ultrafast Infrared Spectroscopy.* The Journal of Physical Chemistry B, 2011. **115**(18): p. 5604-5616.
70. Nienhuys, H.-K., et al., *Mechanism for vibrational relaxation in water investigated by femtosecond infrared spectroscopy.* The Journal of Chemical Physics, 1999. **111**(4): p. 1494-1500.
71. Nitzan, A., *Chemical Dynamics in Condensed Phases: Relaxation, Transfer, and Reactions in Condensed Molecular Systems*. 2013: OUP Oxford.
72. Novoderezhkin, V.I., E. Romero, and R. van Grondelle, *How exciton-vibrational coherences control charge separation in the photosystem II reaction center.* Physical Chemistry Chemical Physics, 2015.
73. Petersen, P.B., et al., *Ultrafast N−H Vibrational Dynamics of Cyclic Doubly Hydrogen-Bonded Homo- and Heterodimers.* The Journal of Physical Chemistry B, 2008. **112**(42): p. 13167-13171.
74. Petersen, P.B. and A. Tokmakoff, *Source for ultrafast continuum infrared and terahertz radiation.* Optics Letters, 2010. **35**(12): p. 1962-1964 KW - Nonlinear optics, four-wave mixing KW - Infrared KW - Ultrafast technology KW - Supercontinuum generation UR - http://ol.osa.org/abstract.cfm?URI=ol-35-12-1962.

75. Rhile, I.J., et al., *Concerted Proton−Electron Transfer in the Oxidation of Hydrogen-Bonded Phenols.* Journal of the American Chemical Society, 2006. **128**(18): p. 6075-6088.
76. Rhile, I.J. and J.M. Mayer, *One-Electron Oxidation of a Hydrogen-Bonded Phenol Occurs by Concerted Proton-Coupled Electron Transfer.* Journal of the American Chemical Society, 2004. **126**(40): p. 12718-12719.
77. Rini, M., et al., *Femtosecond mid-infrared spectroscopy of condensed phase hydrogen-bonded systems as a probe of structural dynamics.* Faraday Discussions, 2003. **122**(0): p. 27-40.
78. Rospenk, M. and T. Zeegers-Huyskens, *FT-IR (7500−1800 cm-1) Study of Hydrogen-Bond Complexes between Phenols−OH(OD) and Pyridine. Evidence of Proton Transfer in the Second Vibrational Excited State.* The Journal of Physical Chemistry A, 1997. **101**(45): p. 8428-8434.
79. Sando, G.M., Q. Zhong, and J.C. Owrutsky, *Vibrational and rotational dynamics of cyanoferrates in solution.* The Journal of Chemical Physics, 2004. **121**(5): p. 2158-2168.
80. Schrauben, J.N., et al., *Multiple-Site Concerted Proton–Electron Transfer Reactions of Hydrogen-Bonded Phenols Are Nonadiabatic and Well Described by Semiclassical Marcus Theory.* Journal of the American Chemical Society, 2012. **134**(40): p. 16635-16645.
81. Siegbahn, P.E.M., *Structures and Energetics for O2 Formation in Photosystem II.* Accounts of Chemical Research, 2009. **42**(12): p. 1871-1880.
82. Sjödin, M., et al., *The mechanism for proton-coupled electron transfer from tyrosine in a model complex and comparisons with Y(Z) oxidation in photosystem II.* Philosophical Transactions of the Royal Society B: Biological Sciences, 2002. **357**(1426): p. 1471-1511.
83. Soudackov, A., E. Hatcher, and S. Hammes-Schiffer, *Quantum and dynamical effects of proton donor-acceptor vibrational motion in nonadiabatic proton-coupled electron transfer reactions.* The Journal of Chemical Physics, 2005. **122**(1): p. 014505.
84. Sundström, V., *Femtobiology.* Annual Review of Physical Chemistry, 2008. **59**(1): p. 53-77.
85. Sung, J. and R.J. Silbey, *Four wave mixing spectroscopy for a multilevel system.* The Journal of Chemical Physics, 2001. **115**(20): p. 9266-9287.
86. Sytnik, A., D. Gormin, and M. Kasha, *Interplay between excited-state intramolecular proton transfer and charge transfer in flavonols and their use as protein-binding-site fluorescence probes.* Proceedings of the National Academy of Sciences, 1994. **91**(25): p. 11968-11972.
87. Sytnik, A. and M. Kasha, *Excited-state intramolecular proton transfer as a fluorescence probe for protein binding-site static polarity.* Proceedings of the National Academy of Sciences, 1994. **91**(18): p. 8627-8630.
88. Tedder, J.M., *Which Factors Determine the Reactivity and Regioselectivity of Free Radical Substitution and Addition Reactions?* Angewandte Chemie International Edition in English, 1982. **21**(6): p. 401-410.
89. Tokmakoff, A. and M.D. Fayer, *Infrared Photon Echo Experiments: Exploring Vibrational Dynamics in Liquids and Glasses.* Accounts of Chemical Research, 1995. **28**(11): p. 437-445.
90. Tokmakoff, A., B. Sauter, and M.D. Fayer, *Temperature-dependent vibrational relaxation in polyatomic liquids: Picosecond infrared pump–probe experiments.* The Journal of Chemical Physics, 1994. **100**(12): p. 9035-9043.

91. Tokmakoff, A., et al., *Vibrational spectral diffusion and population dynamics in a glass-forming liquid: Variable bandwidth picosecond infrared spectroscopy.* The Journal of Chemical Physics, 1995. **102**(10): p. 3919-3931.
92. Tommos, C. and G.T. Babcock, *Proton and hydrogen currents in photosynthetic water oxidation.* Biochimica et Biophysica Acta (BBA) - Bioenergetics, 2000. **1458**(1): p. 199-219.
93. Voet, D. and J.G. Voet, *Biochemistry, 4th Edition*. 2010: John Wiley & Sons.
94. Wenger, O.S., *Proton-coupled electron transfer with photoexcited ruthenium(II), rhenium(I), and iridium(III) complexes.* Coordination Chemistry Reviews, 2015. **282–283**(0): p. 150-158.
95. Westlake, B.C., et al., *Concerted electron-proton transfer in the optical excitation of hydrogen-bonded dyes.* Proceedings of the National Academy of Sciences, 2011. **108**(21): p. 8554-8558.
96. Wikstrom, M., *Identification of the electron transfers in cytochrome oxidase that are coupled to proton-pumping.* Nature, 1989. **338**(6218): p. 776-778.
97. Wright, J.C., *Multiresonant Coherent Multidimensional Spectroscopy.* Annual Review of Physical Chemistry, 2011. **62**(1): p. 209-230.
98. Yabushita, A., T. Fuji, and T. Kobayashi, *SHG FROG and XFROG methods for phase/intensity characterization of pulses propagated through an absorptive optical medium.* Optics Communications, 2001. **198**(1–3): p. 227-232.
99. Yamaguchi, S., et al., *Vibrational dynamics of benzoic acid in nonpolar solvents studied by subpicosecond infrared pump–probe spectroscopy.* Chemical Physics Letters, 2008. **462**(4–6): p. 238-242.

APPENDIX

For simplicity, only the most recent DBQ data collected on November 21, 2014 is described/parameterized here. The analysis of all other data sets discussed in this dissertation is conducted in a similar manner with minimal modification such as the points for piece-wise composition and grating positions used.

A.1 Matlab Files for Building Frequency Axis

```
clear all

%% Setting up Filter Response

%%%%%%%%%%%%%%%   Response of MCT & Filter
%%%%%%%%%%%%%%%%%%%%%%%%%%%%%%%%
patr='C:\Users\Anthony\Documents\Chemistry\Research\Summer11\BBIR_Data\IR\Spectra\Respons
e\';
cd(patr);

MT1=load('MCT\F-35466.TBL');
MP1=load('Filter\Spectragon_BBP-2540-5150c_nm_red_side(2).txt');
LP=load('Filter\Spectragon_LP-4500nm_purple_side(2).txt');
GS=load('Filter\GlassStack-thin_20140618.txt');

MP(:,1)=1000*MP1(:,1);
MP(:,2)=MP1(:,2);

ND03=load('ND\0.3_IR_ND-2.txt');
ND05=load('ND\0.5_IR_ND-2.txt');
ND07=load('ND\old\0.7_IR_ND-1.txt');
ND10=load('ND\1.0_IR_ND-2_2.txt');
ND13=load('ND\old\1.3_IR_ND-1.txt');
ND17=load('ND\old\1.7_IR_ND-1.txt');
ND20=load('ND\2.0_IR_ND-2.txt');
ND3T=load('ND\3.0_IR_ND-2.txt');
ND30a=load('ND\3.0_IR_ND-Thorlabs.txt');
ND0S=load('ND\500micron_Si_2.txt');

% % Abs -> %T
ND30b(:,1)=ND30a(:,1);
ND30b(:,2)=10^-1*(ND30a(:,2)./1  );

ND031(:,1)=ND03(:,1);
ND031(:,2)=-log10(ND03(:,2)./100);
ND0S1(:,1)=ND0S(:,1);
ND0S1(:,2)=(ND0S(:,2));
```

```
ND051(:,1)=ND05(:,1);
ND051(:,2)=-log10(ND05(:,2)./100);
ND071(:,1)=ND07(:,1);
ND071(:,2)=-log10(ND07(:,2)./100);
ND101(:,1)=ND10(:,1);                    %%% Hmm useful for individual
ND101(:,2)=-log10(ND10(:,2)./100);            %%% grating treatment only
ND131(:,1)=ND13(:,1);
ND131(:,2)=-log10(ND13(:,2)./100);
ND171(:,1)=ND17(:,1);
ND171(:,2)=-log10(ND17(:,2)./100);
ND201(:,1)=ND20(:,1);
ND201(:,2)=-log10(ND20(:,2)./100);
ND301(:,1)=ND30b(:,1);
ND301(:,2)=-log10(ND30b(:,2)./100);
ND3T1(:,1)=ND3T(:,1);
ND3T1(:,2)=-log10(ND3T(:,2)./100);

NMP(:,2)=-log10(MP(:,2)./100);
NLP(:,2)=-log10(LP(:,2)./100);
NSP(:,2)=GS(:,2);
NMP(:,1)=10000000./MP(:,1);
NLP(:,1)=10000000./LP(:,1);
NSP(:,1)=GS(:,1);

SP1(:,2)=10.^(-1.*NMP(:,2));
LP1(:,2)=10.^(-1.*NLP(:,2));
GP1(:,2)=10.^(-1.*NSP(:,2));
%% References

Ref1=load('C:\Users\Anthony\Documents\Chemistry\Research\Summer11\BBIR_Data\IR\Reference\
Polystyrene_20110804.txt');
for k=1:length(Ref1(:,1))
 Ref1nm(k,1)=10000000/Ref1(k,1);
end

Ref2=load('C:\Users\Anthony\Documents\Chemistry\Research\Winter13\Reference\WaterVapor-
IR.txt');
for k=1:length(Ref2(:,1))
 Ref2nm(k,1)=10000000/Ref2(k,1);
end

Ref31=load('C:\Users\Anthony\Documents\Chemistry\Research\Autumn13\FTIR\20131011_SNP-
50mM.txt');
Ref3(:,1)=Ref31(:,1);
Ref3(:,2)=Ref31(:,2)./max(Ref31(:,2));

for k=1:length(Ref3(:,1))
 Ref3nm(k,1)=10000000/Ref3(k,1);
end
```

```
cf=load('C:\Users\Anthony\Documents\Chemistry\Research\Winter14\PCET\ND2\Data\20140313\Probe\CorF.mat', 'CorF');

CorF=cf.CorF;
%
pat1='C:\Users\Anthony\Documents\Chemistry\Research\Winter14\PCET\HBQ\Data\20141121\LOp1';  %starts at 3500nm  ; 6 pos

pat1='C:\Users\Anthony\Documents\Chemistry\Research\Winter14\PCET\HBQ\Data\20141121\LOx1';  %starts at 3500nm  ; 6 pos
 spec_name11={'HBQdLO_'};
 glen=06;
 slen=02;

 for k3=1:glen
   % func=['spec_name21(' int2str(k3) ')=[{'''  int2str(k3*500+3000) 'g-SP_ND2-LOSpec_'}];'];
%Strange case of ND2
    func=['spec_name21(' int2str(k3) ')=[{'''  int2str(k3*500+3000) 'g_'}];'];
   % func=['spec_name21(' int2str(k3) ')=[{'''  int2str(k3*500+3000) 'g-psy_'}];'];
    eval(func);
 end

%      for k3=4:06
%        func=['spec_name21(' int2str(k3) ')=[{'''  int2str(k3*500+3000) 'g-LP_ND2-LOSpec_'}];'];
%Strange case of ND2
%        eval(func);
%      end
%      for k3=7:glen
%        func=['spec_name21(' int2str(k3) ')=[{'''  int2str(k3*500+3700) 'g-LP_ND2-LOSpec_'}];'];
%Strange case of ND2
%        eval(func);
%      end

cd(pat1);
%% Load, sort and average

for s1=1:slen
   func=['spec_name31(' int2str(s1) ')=[{''' int2str(s1) '''}];'];
   eval(func);
end

for k2=1:slen
   for k3=1:glen
         func=['BB_' int2str(k3) '(:,:,' int2str(k2) ')=load(char(strcat(      spec_name11 ,spec_name21(' int2str(k3) '),spec_name31(' int2str(k2) '))));'];
         eval(func);
   end
end

zt=glen;
```

```
 for k2=1:zt
       func=['BB_' int2str(k2) '(129:end,:,:)=[];'];
       eval(func);
      % func=['BB_' int2str(k2) '(1:64,:,:)=[];'];
      % eval(func);
 end

 for k2=1:zt
       func=['BB_a' int2str(k2) '=mean(BB_' int2str(k2) ',3);'];
       eval(func);
 end
%% Keeping stripe 1 and Archiving stripe 2

for k2=1:zt
   func=['Arc_' int2str(k2) '(1:64,:)=BB_a' int2str(k2) '(65:128,:);'];
   eval(func);
end

for k2=1:zt
   func=['BB_b' int2str(k2) '(1:64,1)=BB_a' int2str(k2) '(1:64,1);'];
   eval(func);
   func=['BB_b' int2str(k2) '(1:64,2)=CorF.*BB_a' int2str(k2) '( 1: 64,2);'];
   eval(func);
end

%% Piece-wise

  ptm=[160 ; 128 ;  96 ;  64 ;  33 ;  0 ];     % % 20141113 x6 pos ZZZZ
% ptm=[ 206 ; 174 ; 142 ; 110 ; 78 ; 45 ; 0 ];     % % 20140811 x7 ZZZZ
% ptm=[ 207 ; 175 ; 143 ; 110 ; 78 ; 45 ; 0 ];     % % 20140806 x7 ZZZZ
% ptm=[210 ; 178 ; 145 ; 112 ; 79 ; 49 ; 0 ];     % % 20140307 x7

figure
hold on
   plot(BB_b1(1:64,1)+ptm(1)  ,      BB_b1( 1: 64,2,1), '-r')
   plot(BB_b2(1:64,1)+ptm(2)  , BB_b2( 1: 64,2,1), '-b')
   plot(BB_b3(1:64,1)+ptm(3)  ,  BB_b3( 1: 64,2,1), '-g')
   plot(BB_b4( :  ,1)+ptm(4)  , BB_b4( 1: 64,2,1), '-r')
     plot(BB_b5( :  ,1)+ptm(5)  , BB_b5( 1: 64,2,1), '-b')
     plot(BB_b6( :  ,1)+ptm(6)  , BB_b6( 1: 64,2,1), '-g')
 %   plot(BB_b7( :  ,1)+ptm(7)  , BB_b7( 1: 64,2,1), '-r')
 %   plot(BB_b8( :  ,1)+ptm(8)  , BB_b8( 1: 64,2,1), '-b')
 %  plot(BB_b9( :  ,1)+ptm(9)  , BB_b9( 1: 64,2,1), '-g')

%%

% % 20141121 DBQ
 pol(1,:)=[   1 ,  64 ];
 pol(2,:)=[  65 ,  90 ];
```

```
 pol(3,:)=[  91 , 128 ];
 pol(4,:)=[ 129 , 149 ];
 pol(5,:)=[ 150 , 192 ];
 pol(6,:)=[ 193 , 224 ];


for k3=1:glen
   zp(k3)=k3;
end
pi=fliplr(zp);

%%

endpt=pol(end,2);

  BB_N=zeros(endpt,2);
  BB_N(:,1)=1:1:endpt;

%%

% 20130422
for mi=01:zt
   func=['BB_N( pol(mi,1):pol(mi,2),2)=BB_b' int2str(pi(mi)) '(pol(mi,1)-ptm(pi(mi))  :pol(mi,2)-
ptm(pi(mi))  ,2);'];
   eval(func);
end

 figure
 hold on
 plot(BB_N(:,1), BB_N(:,2), '-r')
 xlabel('wavenumber (pixel)')

%%

BB_lm(:,1)=(BB_N(:,1));
BB_lm(:,2)=flipud(BB_N(:,2));

% figure
% hold on
% plot(Ref1nm(:,1), Ref1(:,2), '-r')
% xlabel('\lambda (nm)')
% xlim([1800 5000])
%
figure
hold on
plot(BB_lm(:,1), BB_lm(:,2), '-r')
xlabel('\lambda (pixel)')

%%
```

```
  figure
    plot(Ref1(:,1), Ref1(:,2), '-r', 'linewidth', 2);
  % plot(Ref2(:,1), Ref2(:,2), '.-r', 'linewidth', 2);
  % plot(Ref3(:,1), Ref3(:,2), '.-r', 'linewidth', 2);
  % plot(Ref1nm(:,1), Ref1(:,2), '.-b', 'linewidth', 2);
  % plot(Ref2nm(:,1), Ref2(:,2), '.-b', 'linewidth', 2);
  % plot(Ref3nm(:,1), Ref3(:,2), '.-b', 'linewidth', 2);
  set(gca, 'fontname', 'arial', 'fontsize', 20, 'fontweight', 'bold')
    set(gca, 'tickdir', 'out', 'TickLength', [0.03, 0.01], 'LineWidth',1.5)%'XTick',1200:500:4200,
'XMinorTick', 'on')
  % title('Polystyrene FTIR Spectrum')
  % title('H_2O Vapor FTIR Spectrum')
  % title('SNP FTIR Spectrum')
  ylabel('Intensity')
  xlabel('Wavenumbers (cm^{-1})')
   xlim([1200 4200])
% xlabel('Wavelength (nm)')
%  xlim([3000 8800])
    ylim([ 0.0 2.5])

%% Calibration

  % Point choice

%   %Polystyrene
% %  fx( 1,1)=3268;  %polystyrene 3082cm-1
%    fx(1,1)=3305;  %polystyrene 3026
%    fx(2,1)=3421;  %polystyrene 2923
% % %fx(4,1)=3487;  %polystyrene 3487
%    fx(3,1)=3510;  %polystyrene 2849cm-1
%
%   %CO2
% %   fx( 4,1)=4230;  %CO2 R-branch
%   fx( 4,1)=4259;  %CO2 Q-branch
% %   fx( 6,1)=4272;  %CO2 P-branch
%
%    %Water lines
% % fx(4,1)=4625;
% % fx(5,1)=4677;
% % fx(5,1)=5149;
%
%   %SNP
%  %fx( 7,1)=3854; % Double Crown in SNP @
% %  fx( 7,1)=4661; % CN 2141 cm-1
% %  fx( 8,1)=4890; % MeOH 2030 cm-1
% %  fx( 9,1)=5238; % NO 1909 cm-1

%     fx(1,1)=3066.5; % 2PP point; 3261 cm-1
%     fx(1,1)=3264.8; % ND2 point; 3063 cm-1... perhaps amine stretch?
      fx(1,1)=3274.4; % HBQ-OD ArylCH 3054 cm-1
```

```
      fx(2,1)=3305;  %polystyrene ; 3026
      fx(3,1)=3421;  %polystyrene ; 2923
      fx(4,1)=3510;  %polystyrene ; 2849

%     fx(4,1)=3893;  %2PP point ; 2568.7 cm-1
%     fx(4,1)=3708;  %HBQ point ; 2697   cm-1

% fx(3,1)=4230;  %CO2 R-branch
  fx(5,1)=4259;  %CO2 Q-branch ; 2348
% fx(5,1)=4272;  %CO2 P-branch

   %Water lines
% fx(4,1)=4625;
% fx(5,1)=4677;
% fx(2,1)=5821;
% fx(3,1)=6061;

%   fx(5,1)=4438.7; % CDCl3 CD ; 2252 cm-1

%   fx(6,1)=4661;  %SNP CN
%   fx(7,1)=4890;  %SNP MeOH
%   fx(8,1)=5238;  %SNP NO

   fx(6,1)=4635;  %HBQ-OD v01 shoulder 2157.5 cm-1

   fx(7,1)=4810;  %HBQd-ODmax
   fx(8,1)=6154;  %HBQ C-C; 1625 cm-1
   fx(9,1)=6297; %HBQ C-O 1588cm-1

%    fx(9,1)=6246;  %Polystyrene ; CHCl3 peak
%    fx(10,1)=6700;  %Polystyrene
%    fx(11,1)=6885;  %Polystyrene ;

%%%%% Match points

% % % 20141121
  fx(1,2)= 14;  %special ArylCH
  fx(2,2)= 20;  %PSY (Polystyrene)
  fx(3,2)= 27;  %PSY
  fx(4,2)= 31;  %PSY
  fx(5,2)= 79;  % CO2 Q
  fx(6,2)=101;  %special v01 shoulder
  fx(7,2)=111;  %HBQ-OD
  fx(8,2)=205;  %HBQ
  fx(9,2)=209;  %HBQ


fit1=polyfit(fx(:,1),fx(:,2),1);
r2=corrcoef(fx(:,1),fx(:,2));
```

```
fit=[fit1(1) fit1(2) r2(2,1)];


%% Generate new axis

for nn=1:length(BB_lm)
   ln(nn,1)=(BB_lm(nn,1)-fit1(2))/fit1(1) -  0;    %  HBQOH-13 ; 2PP-3
end

%   figure
%   plot(lnm, BB_lm(:,2))

for nn=1:length(BB_lm)
   wm(nn,1)=10000000./ln(nn,1);
end

BB1=BB_lm(:,2);

%% Plot before filter response division

mx=max(BB1)*1.10;
mn=min(BB1)*1.10;


figure
plot(wm , BB1(:,1), 'r', 'linewidth', 3)
set(gca,'linewidth', 2, 'fontweight', 'bold', 'fontname', 'Arial', 'fontsize', 18)
set(gca, 'tickdir', 'out', 'TickLength', [0.03, 0.01])
xlabel('\omega ')
ylabel('Intensity')
title('BBIR Spectral Before Filter Response')
 xlim([min(wm) max(wm)])
 ylim([mn mx])

%% Reverse Engineering - backing out the axis for each grating position

hm=length(BB_b1(:,1))  ;

 BBG_1=zeros(hm,zt);
 w3G_1=zeros(hm,zt);

wm1=flipud(wm);
for k3=1:zt
   w3G_1(1:64,k3)=wm1(ptm(k3)+1:ptm(k3)+64,1);
end

 for k2=1:zt
    func=['BBG_1(1:64,k2)=BB_b' int2str(k2) '(1:64,2);'];
    eval(func);
 end
```

```
%% plot to check

figure
hold all
for pz=1:zt
   plot(w3G_1(1:64,pz), BBG_1(1:64,pz), '-r', 'linewidth', 2);
end
   plot(wm, BB1(:,1), '-b', 'linewidth', 2)

%% Divide by Response of Filters

rt=length(BBG_1(:,1));
kt=length(BBG_1(1,:));

lz=w3G_1;
c1=glen;
ND1=zeros(rt,c1,kt);
PFil=zeros(rt,2,kt);

 for mz=1:kt
      %Optical Density
   ND1(:, 1,mz)=interp1(ND031(:,1),ND031(:,2), lz(:,mz));
   ND1(:, 2,mz)=interp1(ND051(:,1),ND051(:,2), lz(:,mz));
   ND1(:, 3,mz)=interp1(ND071(:,1),ND071(:,2), lz(:,mz));
   ND1(:, 4,mz)=interp1(ND101(:,1),ND101(:,2), lz(:,mz));
   ND1(:, 5,mz)=interp1(ND131(:,1),ND131(:,2), lz(:,mz));
   ND1(:, 6,mz)=interp1(ND171(:,1),ND171(:,2), lz(:,mz));
   ND1(:, 7,mz)=interp1(ND201(:,1),ND201(:,2), lz(:,mz));
   ND1(:, 8,mz)=interp1(ND301(:,1),ND301(:,2), lz(:,mz));
   ND1(:, 9,mz)=interp1(ND071(:,1),ND071(:,2), lz(:,mz));
   ND1(:,10,mz)=interp1(ND0S1(:,1),ND0S1(:,2), lz(:,mz));
      %Wavelength Dependent
   PFil(:,3,mz)=interp1(NSP(:,1), NSP(:,2), lz(:,mz)); % glass stack
   PFil(:,1,mz)=interp1(NMP(:,1), NMP(:,2), lz(:,mz));
   PFil(:,2,mz)=interp1(NLP(:,1), NLP(:,2), lz(:,mz));
 end
ND=zeros(rt,kt);
BB2=zeros(rt,kt);
BB3=zeros(rt,kt);


% % 20141105
for z=1:rt
% ND(z,1)=ND1(z, 2,1);    %3500   0.5ND
% ND(z,2)=ND1(z, 2,2);    %4000   0.5ND
% ND(z,3)=ND1(z, 2,3);    %4500   0.5ND
% ND(z,4)=ND1(z, 2,4);    %5000   0.5ND
% ND(z,5)=ND1(z, 2,5);    %5500   0.5ND
% ND(z,6)=ND1(z, 2,6);    %6000   0.5ND
```

```
ND(z,1)=0 ;    %3500   Not needed for S2S Norm
ND(z,2)=0 ;    %4000
ND(z,3)=0 ;    %4500
ND(z,4)=0 ;    %5000
ND(z,5)=0 ;    %5500
ND(z,6)=0 ;    %6000
end


 % 20141105
PF(:,1)=PFil(:,1,1);
PF(:,2)=PFil(:,1,2);
PF(:,3)=PFil(:,1,3);
PF(:,4)=PFil(:,2,4);
PF(:,5)=PFil(:,2,5);
PF(:,6)=PFil(:,2,6);

%% Analyzing the LO response - removing the ND filter and Pass filter response

% MCT_C=3276.7;
% divF=1000*MCT_C;
  divF=1;

for z=1:zt
   for rr=1:rt
      BB2(rr,z)=(BBG_1(rr,z)./divF)./10.^(-1.*ND(rr,z));
      BB3(rr,z)=BB2(rr,z)./10.^(-1.*PF(rr,z));
   end
end

% for z=05:06
%     for rr=1:rt
%        BB2(rr,z)=(BBG_1(rr,z)./divF)./10.^(-1.*ND(rr,z));
%        BB3(rr,z)=BB2(rr,z).*10.^(-1./PF(rr,z));
%     end
% end

%% Quick Check

%  figure
% hold on
%   plot(lz(:,2), 0.041*BBG_1(:,2),'r')
%   plot(lz(:,2), 180*BB2(:,2),'b')
%   plot(lz(:,4), BB3(:,4),'r')
%   plot(lz(:,5), BB3(:,5),'g')

 %
  figure
  hold on
  for t=1:zt
```

```
    plot(lz(:,t), BB3(:,t))
  % plot(lz(:,t), BB2(:,t))
 end


%% Piece-wise once again

for mi=01:zt
   BB4( pol(mi,1):pol(mi,2),1)=BB3( pol(mi,1)-ptm(pi(mi))  : pol(mi,2)-ptm(pi(mi))  ,pi(mi));
   w3g( pol(mi,1):pol(mi,2),1)=lz( pol(mi,1)-ptm(pi(mi))  : pol(mi,2)-ptm(pi(mi))  ,pi(mi));
end

lng(:,1)=10000000./w3g(:,1);

%% Check once again
zz=endpt;

figure
 plot(w3g, BB4, '-r', 'linewidth', 2)

%%
SPEC=[lnm wcm BBIR];

SPEC2=SPEC;
w3mat=lz;

%% Save

 save SPEC2 SPEC2
% save SPEC1 SPEC1

 save ND ND
 save PF PF
 save w3mat w3mat
 save BB3 BB3
```

A.2 Pump-probe Data Averaging and Background Subtraction

```
clear all

%% Loading axes calibration Files
cf=load('C:\Users\Anthony\Documents\Chemistry\Research\Winter14\PCET\ND2\Data\20140313\Probe\CorF.mat', 'CorF');
CorF=cf.CorF;

pat1='C:\Users\Anthony\Documents\Chemistry\Research\Winter14\PCET\HBQ\Data\20141121\LOp1';  %starts at 3500nm
%
pat1='C:\Users\Anthony\Documents\Chemistry\Research\Winter14\PCET\HBQ\Data\20141121\LOx1';  %starts at 3500nm
```

```
cd(pat1);

load ND
load PF
load w3mat
load BB3
load SPEC1

w3g=w3mat; %#ok<*NASGU>
BkSp=BB3; %#ok<NASGU>
BBIR=SPEC1(:,3);
wcm=SPEC1(:,2);

%% Examine LO

 figure
 plot(wcm, BBIR, '-r', 'linewidth', 2)

%% Loading the PP scans
%
pat2='C:\Users\Anthony\Documents\Chemistry\Research\Winter14\PCET\HBQ\Data\20141121\HB
Qdp1'; %starts at 3500nm
%
pat2='C:\Users\Anthony\Documents\Chemistry\Research\Winter14\PCET\HBQ\Data\20141121\HB
Qdx1'; %starts at 3500nm
% glen=06;
% scan=40; %CCl4 P 20, X 40

 for k3=1:glen
     % func=['spec_name21(' int2str(k3) ')=[{"_'  int2str(k3*500+3000) '"}];'];  %20141105
    eval(func);
 end

for s1=1:scan
 % func=['spec_name21(' int2str(s1) ')=[{"' int2str(s1) '"}];'];  %ND2
   func=['spec_name11(' int2str(s1) ')=[{"PP_' int2str(s1) '"}];'];
   eval(func);
end

% PS=length(spec_name11); % % For March ND2 only
 PS=length(spec_name21);
spec_name31={'_Diff.dat'};
cd(pat2);
%%
tic

% P data 20140307
for k3=1:PS
```

```
   for k1=1:scan
     func=['PPMat_' int2str(k3) '(:,:,' int2str(k1) ')=load(char(strcat(      spec_name11(' int2str(k1)
'),spec_name21(' int2str(k3) '),spec_name31)));'];   %20140806
     eval(func);

toc % 04/13: 28 sec;  10/13: 40 sec;  10/24:  7 sec; 06/17: 7 sec;
%% Removing pixels beyond 128

% t2=PPMat_1(129,:,40);

 timex=PPMat_2(66,:,1);  % in mm
% timex=PPMat_2(65,:,1);  % in fs
 tconv=1/6671.336602;  %mm/fs
%   S1_0=56990.02;  % fs 20141121 HBQd ZZZZ
%   S1_0=56990.01;  % fs 20141121 HBQd ZZYY

 t2= -1*(timex(1,:)-S1_0)./tconv;      % mm approach
% t2= -1*(timex(1,:)-S1_0);            % fs approach

 save t2 t2

tlen1=length(t2);
%%
for k2=1:PS
   func=['PPM_' int2str(k2) '=PPMat_' int2str(k2) ';'];
   eval(func);
end

for k2=1:PS
   func=['PPM_' int2str(k2) '( 66:end,:,:)=[];'];
   eval(func);
end

%%
for k3=1:PS
  for k2=1:scan
     for k1=1:tlen1
      func=['PPM_a' int2str(k3) '(1:64,k1,k2)=CorF(1:64,1).*PPM_' int2str(k3) '(1:64,k1,k2);'];
      eval(func);
     end
  end
end

%%

wx=64;

MCT_C=3276.7;
% divF=1*MCT_C;
divF=1;
```

```
%%  Averaging and Standard Deviation     ;

for k2=01:PS
   for k31=1:tlen1
      for w1=1:wx
         func=['PPM_aa(' int2str(w1) ',' int2str(k31) ',' int2str(k2) ')=mean(PPM_a' int2str(k2) '('
int2str(w1) ',' int2str(k31) ',:));'];
         eval(func);
         func=['PPM_aaS(' int2str(w1) ',' int2str(k31) ',' int2str(k2) ')=std(PPM_a' int2str(k2) '('
int2str(w1) ',' int2str(k31) ',:));'];
         eval(func);
      end
   end
end
  %% Making Cell for easy saving

  PPC_P.I2{1,1}=PPM_aa;
  PPC_P.I2{1,2}=PPM_aaS;

% PPC_X.I2{1,1}=PPM_aa;
% PPC_X.I2{1,2}=PPM_aaS;

% PPC_S.I2{1,1}=PPM_aa;
% PPC_S.I2{1,2}=PPM_aaS;

  save PPC_P PPC_P
% save PPC_X PPC_X
% save PPC_S PPC_S
  save t2 t2

clear all

pat1='C:\Users\Anthony\Documents\Chemistry\Research\Winter14\PCET\HBQ\Data\20141121\LOp
1'; %starts at 3500nm
%
pat2='C:\Users\Anthony\Documents\Chemistry\Research\Winter14\PCET\HBQ\Data\20141121\HB
Qdp1'; %starts at 3500nm
%
pat1='C:\Users\Anthony\Documents\Chemistry\Research\Winter14\PCET\HBQ\Data\20141121\LOx
1'; %starts at 3500nm
%
pat2='C:\Users\Anthony\Documents\Chemistry\Research\Winter14\PCET\HBQ\Data\20141121\HB
Qdx1'; %starts at 3500nm

cd(pat1);
load w3mat
load BB3
load SPEC1
```

```
cd(pat2);
load t2
  load PPC_P
  PPC=PPC_P;

% load PPC_X
% PPC=PPC_X;

% load PPC_S
% PPC=PPC_S;

w3g=w3mat;
BkSp=BB3;
BBIR=SPEC1(:,3);
wcm=SPEC1(:,2);

PS=length(w3g(1,:));

PPM_aa=PPC.I2{1,1};
PPM_aaS=PPC.I2{1,2};

tlen1=length(t2);
wx=64;

%% piecewise array ; P==parallel  , X==cross

%   % % 20141121 x6
%   ptm=[160 ; 128 ;  96 ;  64 ;  33 ;  0 ];     % % 20141105 x6 pos
%    pol(1,:)=[   1 ,  64 ];
%    pol(2,:)=[  65 ,  90 ];
%    pol(3,:)=[  91 , 128 ];
%    pol(4,:)=[ 129 , 149 ];
%    pol(5,:)=[ 150 , 192 ];
%    pol(6,:)=[ 193 , 224 ];

 zp=zeros(PS,1);

for k3=1:PS
  zp(k3)=k3;
end
pi=flipud(zp);

  wclen=pol(end,end)+wx;

wmx=pol(end,end);

%%

  PP_AVG_A=zeros(PS,tlen1);
```

```
    for k30=1:tlen1
       for mi=01:PS;
          PP_AVG_A( pol(mi,1):pol(mi,2),k30)=PPM_aa(  pol(mi,1)-ptm(pi(mi))  : pol(mi,2)-
ptm(pi(mi))  ,k30,pi(mi));
       end
    end

  PPC.M{5,1}=PP_AVG_A;

%%  Subtracting off probe baseline, i.e. most negative time point

wl1=length(BBIR);
PP_AVG_As=zeros(wl1,tlen1);

for w1=1:wl1
    for ts=1:tlen1
       PP_AVG_As(w1,ts)=PP_AVG_A(w1,ts)-PP_AVG_A(w1,1);
    end
end

PPC.M{5,3}=PP_AVG_As;
    %% Re-save data

    PPC_P=PPC;
  % PPC_X=PPC;

  save PPC_P PPC_P
% save PPC_X PPC_X
% save PPC_S PPC_S
```

A.3 Piece-wise Joining of the Pump-probe Spectra into an Array

```
clear all

%% Loading FTIR for all molecules

pati='C:\Users\Anthony\Documents\Chemistry\Research\Autumn10\PCET_prep-Spectra\';
cd(pati);

  load  ND2    % DOArND2_CHCl3_050601d
  load  Py     % DOAr-Py
  load  HBQ    % HBQ
  load  HBQOD  % HBQ-OD
  load  PP     % 2PP

  FS1=Py;
  FS2=ND2;
  FS3=PP ;
  FS4=HBQ;
  FS5=HBQOD;
```

```
  FTR=FS3;

% wl=find(FTR(:,1)>1700,1, 'last'); %ND2 , Py
% wh=find(FTR(:,1)<2400,1, 'first');

  wh=find(FTR(:,1)>2000,1, 'first'); %HBQ , 2PP
  wl=find(FTR(:,1)>2902,1, 'first');

% wh=find(FTR(:,1)>1640,1, 'first'); %HBQ-OD , 2PP-OD
% wl=find(FTR(:,1)>2502,1, 'first');

FTIR(:,1)=FTR(:,1);
FTzm=max(FTR( wh : wl ,2));
FTIR(:,2)=FTR(:,2)./FTzm;

 %% Loading Data files
%
pat1='C:\Users\Anthony\Documents\Chemistry\Research\Winter14\PCET\HBQ\Data\20141121\LOp
1'; %starts at 3500nm
%
pat2='C:\Users\Anthony\Documents\Chemistry\Research\Winter14\PCET\HBQ\Data\20141121\HB
Qdp1'; %starts at 3500nm
%
pat1='C:\Users\Anthony\Documents\Chemistry\Research\Winter14\PCET\HBQ\Data\20141121\LOx
1'; %starts at 3500nm
%
pat2='C:\Users\Anthony\Documents\Chemistry\Research\Winter14\PCET\HBQ\Data\20141121\HB
Qdx1'; %starts at 3500nm

cd(pat1);
load w3mat
load BB3
load SPEC1
load ND
load PF

cd(pat2);
load t2

  load PPC_P
  PPC=PPC_P;
% load PPC_X
% PPC=PPC_X;
% load PPC_S;
% PPC=PPC_S;

w3g=w3mat;
BkSpg=BB3;
BBIR=SPEC1(:,3);
```

```
wcm=SPEC1(:,2)   ;
NDg=ND;
PFg=PF;

%%

PS=length(w3g(1,:));
PPM_aa=PPC.I2{1,1};
PPM_aaS=PPC.I2{1,2};

 %

tlen1=length(t2  );

wlen=length(wcm);
wx=64;

MCT_C=3276.7;
% divF=1*MCT_C;
  divF=1;

Itzy=[0 0];
Itzx=[wcm(1) wcm(end)];
Itzw=[1 wlen];

%% piecewise array ; P==parallel  , X==cross

%  % % 20141121 x6
% ptm=[160 ; 128 ;  96 ;  64 ;  33 ;  0 ];     % % 20141105 x6 pos ZZZZ
%  pol(1,:)=[   1 ,  64 ];
%  pol(2,:)=[  65 ,  90 ];
%  pol(3,:)=[  91 , 128 ];
%  pol(4,:)=[ 129 , 149 ];
%  pol(5,:)=[ 150 , 192 ];
%  pol(6,:)=[ 193 , 224 ];


for k3=1:PS
  zp(k3)=k3; %#ok<*SAGROW>
end
pi=fliplr(zp);

yptm=zeros(length(ptm),1);

%%

  PP_S=zeros(wlen,tlen1);

% % 20130421
    for k30=1:tlen1
```

```
      for mi=01:PS;
         PP_S( pol(mi,1):pol(mi,2),k30)=PPM_aa(  pol(mi,1)-ptm(pi(mi))  : pol(mi,2)-ptm(pi(mi))
,k30,pi(mi));
%           ND( pol(mi,1):pol(mi,2),1)=NDg( pol(mi,1)-ptm(pi(mi))  : pol(mi,2)-ptm(pi(mi))  ,pi(mi));
% For PP w/o S2S Normalization
%           PF( pol(mi,1):pol(mi,2),1)=PFg( pol(mi,1)-ptm(pi(mi))  : pol(mi,2)-ptm(pi(mi))  ,pi(mi));
% For PP w/o S2S Normalization
         ND( pol(mi,1):pol(mi,2),1)=0;  % For S2S Normalization only
         PF( pol(mi,1):pol(mi,2),1)=0;  % For S2S Normalization only
         BkSp( pol(mi,1):pol(mi,2),1)=BkSpg( pol(mi,1)-ptm(pi(mi))  : pol(mi,2)-ptm(pi(mi))
,pi(mi));
      end
   end

%%  Check composition before filter response removal

wmx=(1:length(PP_S(:,1)));
wml=wmx(end);
zt0=find(t2>=0,1);
zt100=find(t2>=100,1);
zt050=find(t2>= 50,1);
zt500=find(t2>=500,1);

wfl=fliplr(wmx);

figure
hold all
  plot(wmx, PP_S(:,  zt0), '-r','linewidth', 2)
% plot(wmx, PP_S(:,zt100), '-b', 'linewidth', 2)
% plot(wmx, PP_S(:,zt050), '-k', 'linewidth', 2)
% plot(wcm, 2e-3*BkSp(:,1), '-g','linewidth', 2)
% plot(FTIR(:,1), 8e-4*FTIR(:,2), ':k','linewidth', 2)
  plot(Itzw, Itzy, ':k', 'linewidth', 2)
  xlim([35 wml-35])
% xlim([1698 3150])

%% Adding the total matrix to the PP cell after removing bad pixels

PP_As=zeros(wlen,tlen1);
PPA_Bs=zeros(wlen,tlen1);
PPA_Cs=zeros(wlen,tlen1);
PPA_E1=zeros(wlen,tlen1);

%%
tic

wlen3=length(PP_S(:,1));

for w1=1:wlen3
   for k30=1:tlen1
```

```
      PP_As(w1,k30)=PP_S(w1,k30)-PP_S(w1,1);
      PPA_Bs(w1,k30)=(PP_As(w1,k30)./divF)./10.^(-1.*ND(w1,1));
      PPA_Cs(w1,k30)=(PPA_Bs(w1,k30))./10.^(-1.*PF(w1,1));
      PPA_E1(w1,k30)= 1*log10(1-PPA_Cs(w1,k30));
    end
end

toc % 1/2 sec

%% Cross examine PP with FTIR results to check piece-wise composition After filter response
removal

yl=1.1*min(PPA_E1(find(wcm>1901,1,'first'):find(wcm<2800,1,'last'),zt0));
yh=1.3*max(PPA_E1(find(wcm>1901,1,'first'):find(wcm<2800,1,'last'),zt0));

fh=(yh/1.2);

figure
hold all
  plot(wcm    , PPA_E1(:,zt0  ),'-r')
  plot(wcm    , PP_AVG(:,zt0  ), '-b')
  plot(FTIR(:,1), fh*FTIR(:,2), '-k')
  plot(Itzx, Itzy, ':k')
  xlim([wcm(1)-10 wcm(end)-20])
  ylim([yl yh])

%%  Removing CO2 region

  PP_AVG=PPA_E1;

  CO2s=find(wcm>2327,1)-0;
  CO2e=find(wcm>2382,1)+4;
% CO2s=find(wcm>2287,1)-0;
% CO2e=find(wcm>2382,1)+0;

% CH2s=find(wcm>2860,1)-1;
% CH2e=find(wcm>3017,1)+0;
% CH2e=find(wcm>3059,1);
% Cars=find(wcm>1365,1); %ND2
% Care=find(wcm>1590,1)  ;
  Cars=find(wcm>1477,1); %2PP
  Care=find(wcm>1772,1);
% Cars=find(wcm>1530,1)-12; %HBQ
% Care=find(wcm>1642,1)-3;
% Cars=find(wcm>1530,1)   ; %HBQd
% Care=find(wcm>1648,1)  ;

  for k30=1:tlen1
    PP_AVG(Cars:Care,k30)=0;  %% FOR ND2 data
    PP_AVG(CO2s:CO2e,k30)=0;
```

```
 %  PP_AVG(CH2s:CH2e,k30)=0;  %% FOR ND2 data
  end

  PP_AVG_P=PP_AVG;
  PP_AVG_X=PP_AVG;
  PP_AVG_S=PP_AVG;

%%

PPC.F{1,1}=ND;
PPC.F{1,2}=PF;
PPC.F{1,3}=BkSp;

PPC.T1{1,1}=PP_As;
PPC.T1{1,2}=PPA_Bs;
PPC.T1{1,3}=PPA_Cs;
% PPC.T1{1,4}=PPA_D1;
PPC.T1{1,5}=PPA_E1;
  PPC.T1{1,6}=PP_AVG;

PPC.ax{1,1}=wcm;
PPC.ax{1,2}=t2;

%%

% PPC_X=PPC;
  PPC_P=PPC;

  save PPC_P PPC_P
% save PPC_X PPC_X
% save PPC_S PPC_S

%%
%
pat3='C:\Users\Anthony\Documents\Chemistry\Research\Winter14\PCET\HBQ\Data\20141121\Anal
ysis\';
cd(pat3);

% save PP_AVG_P PP_AVG_P
% save PP_AVG_X PP_AVG_X
% save PP_AVG_S PP_AVG_S
% save wcm wcm
% save t2 t2
```

A.4 Pump-probe Vibrational Population Analysis, i.e. fitting

```
clear all

global time y % tp B
```

```
%% PP
pati='C:\Users\Anthony\Google Drive\Chemistry\Research\Autumn10\PCET_prep-Spectra\';
cd(pati);

  load  ND2    % DOArND2_CHCl3_050601d
  load  Py     % DOAr-Py
  load  HBQ    % HBQ
  load  HBQOD  % HBQ-OD
  load  PP     % 2PP

  FS1=Py;
  FS2=ND2;
  FS3=PP ;
  FS4=HBQ;
  FS5=HBQOD;

% pat1='C:\Users\Anthony\Google
Drive\Chemistry\Research\Winter14\PCET\HBQ\Data\20141121\Analysis\';

cd(pat1);
load wcm wcm
load t2 t2
% load PP_AVG_P PP_AVG_P
% load PP_AVG_X PP_AVG_X
% a(:,:,1)=PP_AVG_P(:,:);
% a(:,:,2)=PP_AVG_X(:,:);

  load PP_P PP_P
  load PP_X PP_X
  load PP_Ani PP_Ani
  load PP_AnR PP_AnR
  load PP_Iso PP_Iso
  a1=PP_P;
  a2=PP_X;
  a3=PP_Iso;
  a4=PP_AnR;
  a5=PP_Ani;
w3=wcm;

FTR=FS2;

  wl=find(FTR(:,1)>1700,1, 'last'); %ND2 , Py
  wh=find(FTR(:,1)<2400,1, 'first');

% wh=find(FTR(:,1)>2000,1, 'first'); %HBQ , 2PP
% wl=find(FTR(:,1)>2902,1, 'first');

% wh=find(FTR(:,1)>1640,1, 'first'); %HBQOD , 2PPOD
% wl=find(FTR(:,1)>2502,1, 'first');
```

```
FTIR(:,1)=FTR(:,1);
FTzm=max(FTR( wh : wl ,2));
FTIR(:,2)=FTR(:,2)./FTzm;

 wlen=length(w3(:,1));
 t20o=find(t2>=-1,1);

 % Intensity diff ZZZZ vs ZZYY normalization (Intensity measured by
 % coherent in mV... remember 0.0809 uJ/mV conversion factor)

%  %20140307
%  ZZ=3.40;
%  ZY=3.10;
%  ta(1,:)=t2(1,:)-   10;
%  ta(2,:)=t2(1,:)+    0;

%  %20140806
%  ZZ=5.20;
%  ZY=5.00;
%  ta(1,:)=t2(1,:)-   30;
%  ta(2,:)=t2(1,:)-  120;

%  %20140811
%  ZZ=4.55;
%  ZY=4.50;
%  ta(1,:)=t2(1,:)-    0;
%  ta(2,:)=t2(1,:)-   50;

%  %20141113?
%  ZZ=4.25;
%  ZY=5.55;
%  ta(1,:)=t2(1,:)-    0;
%  ta(2,:)=t2(1,:)-    0;

%  %20141121
%  ZZ=3.8;
%  ZY=4.0;
%  ta(1,:)=t2(1,:)-    0;
%  ta(2,:)=t2(1,:)+   20;

%  PolZ(1)=ZZ;
%  PolZ(2)=ZY;

%  pzlen=length(PolZ);
%  Z=zeros(pzlen,1);
%  NZ=max(PolZ);
%  az=zeros(length(a(:,1,1)),length(a(1,:,1)),length(a(1,1,:)));
%  ai=az;

   % Re-normalizing signal intensity based on Pump fluence
```

```
% for iz=1:pzlen
%   Z(iz)=NZ./PolZ(iz);
% % func=['a' int2str(iz) '(:,:)=Z(iz).*a(:,:,iz);'];
% %  eval(func);
%     for im=1:wlen
%        ai(im,:,iz)=interp1(ta(iz,:),a(im,:,iz),t2,'pchip');
%     end
%   az(:,:,iz)=Z(iz).*ai(:,:,iz);
% end

  % Calculating ZZZZ vs ZZYY Intensity diff for Signal Quality Control

% pucp=find(w3>=2705,1,'first');  %ND2=2167 , HBQOD=2071 , HBQOH&2PP=2705
% pucr=pucp- 5:pucp+ 5;
% putr=t20o-5:t20o+5;
% puln=length(pucr);
% puw3=w3(pucr);
%
% PPF=zeros(puln,1);
% XXF=PPF;
% PXF=PPF;
% PXTr=PPF;
% aXTr=PPF;
% DXTr=PPF;
% an=az;
%
%  for pi=1:puln
%     PPF(pi)=abs(min( az(pucr(pi),putr,1)./ 1 ));
%     XXF(pi)=abs(min( az(pucr(pi),putr,2)./ 1 ));
%   %  PPF(pi)=abs(min( a1(pucr(pi),putr)./ 1 ));
%   %  XXF(pi)=abs(min( a2(pucr(pi),putr)./ 1 ));
%     PXF(pi)=PPF(pi)/XXF(pi);
%  end
%
%  AXF=mean(PXF); % ND2=3.4371 , DBQ=2.4788 , 2PP=2.9580 , HBQ=2.4788
%  AXFn=2.9580;  %Choose value from AXF ref values appropriately
%
%  for pn=1:puln
%     aXTr(pn)=(1/PXF(pn))*(PPF(pn)/XXF(pn));
%     PXTr(pn)=(1/AXF)*(PPF(pn)/XXF(pn));
%     DXTr(pn)=(1/AXFn)*(PPF(pn)/XXF(pn));
%  end
%
%  APXT=mean(PXTr);
%
%    DTr=mean(DXTr);
%
%    for im=1:wlen
%     an(im,:,2)=DTr*az(im,:,2);
```

```
%    end

 %

 % SGolay Filter to remove high frequency noise
tlen=length(t2);
% wg=[];

% % a1(:,:)=sgolayfilt(az(:,:,1),3,7,wg,1);
% % a2(:,:)=sgolayfilt(az(:,:,2),3,7,wg,1);
%   a1(:,:)=sgolayfilt(an(:,:,1),3,7,wg,1);
%   a2(:,:)=sgolayfilt(an(:,:,2),3,7,wg,1);

 % Calculating Isotropic and Anistropic Signal... assuming equal intensity of pump and probe

%   PP_Iso=(a1+2*a2)./3;
%   PP_Ani=(a1-a2)./(a1+2*a2);
%   PP_AnR=(a1-a2);
%   PP_P=a1;
%   PP_X=a2;
%   PP_Ps(:,:)=an(:,:,1);
%   PP_Xs(:,:)=an(:,:,2);
%
%   save PP_Iso PP_Iso
%   save PP_Ani PP_Ani
%   save PP_AnR PP_AnR
%   save PP_P PP_P
%   save PP_X PP_X
%   save PP_Ps PP_Ps
%   save PP_Xs PP_Xs

%%

cspd=0.02997; %cm/ps

nu2wav=1/2/pi()/cspd;  %ans in cm^(-1)
wav2nu=2*pi()*cspd;  %ans in ps^(-1)

resw=zeros(wlen,1);
for n=1:wlen-1
   resw(n)=w3(n+1)-w3(n);
end

res_s=[mean(resw(1:wlen-1)) , std(resw(1:wlen-1))];

time_step1=round(t2(t20o+1)-t2(t20o));

t2z=[-1000 -500 -200 0 t2(end)];
t2zps=t2z/1000;
It2z=[0 0 0 0 0];
```

```
%% Indicating the region to be fit

   %%%DBQ
% pt1=find(w3>1646,1);
% pte=find(w3>2855,1);
% p=pt1:pte;
% v12s=1;
% v12e=find(p==find(wcm>1935,1),1);
% v01s=find(p==find(wcm>1939,1),1);
% v01e=find(p==find(wcm>2194,1),1);
% vUOs=find(p==find(wcm>2200,1),1);
% vUOe=find(p==find(wcm>2340,1),1);
% vOHs=find(p==find(wcm>2604,1),1);
% vOHe=find(p==find(wcm>2860,1),1);

%% Examining the Raw Tw traces

% hp=36;
 b1=find(t2>=-01,1);
 b2=find(t2>= 80,1);
% ymin=min(a1(p(hp),2:end))-5e-4;
% ymax=max(a1(p(hp),2:end))+1e-1;
ppmp=max(a1(pt1:pte,b1));
ppmx=max(a2(pt1:pte,b1));
% ppmi=max(a3(pt1:pte,b1));
% ppma=max(a4(pt1:pte,b1));
  rpx=ppmx/ppmp;
%   rpi=ppmi/ppmp;
%   rpa=ppma/ppmp;

figure
hold on
  plot(w3,    a1(:,b1)./ppmp, 'r', 'linewidth', 2)  % 17 -> 100fs for CH2 , Parallel
% plot(w3, rpx*a2(:,b1  )./ppmx, 'b', 'linewidth', 2)  % 17 -> 100fs for CH2 , Crossed
% plot(w3, rpi*a3(:,b1)./ppmi, 'g', 'linewidth', 2)  % 17 -> 100fs for CH2 , Isotropic
% plot(w3, rpa*a4(:,b1)./ppma, 'm', 'linewidth', 2)  % 17 -> 100fs for CH2 , Anistropic
  plot(FTIR(:,1), FTIR(:,2), '-k', 'linewidth', 2)
set(gca, 'fontname', 'arial', 'fontsize', 20, 'fontweight', 'bold')
set(gca, 'tickdir', 'out', 'TickLength', [0.03, 0.01], 'LineWidth',1.5);%XTick',-200:300:1600,
'XMinorTick', 'off')
  fun=['title(" Spectra of DOAr-ND_2 at \tau_2=' int2str(t2(b1)) ' fs ")'];
% fun=['title(" Spectra of 2PP at \tau_2=' int2str(t2(b1)) ' fs ")'];
% fun=['title(" Spectra of HBQ at \tau_2=' int2str(t2(b1)) ' fs ")'];
 eval(fun)
% legend('PP-P', 'PP-X', 'FTIR')
  legend('PP-P', 'PP-X', 'PP-Istropic', 'PP-Anistropic', 'FTIR')
  legend('boxoff')
xlabel('\omega_3/2\pic (cm^{-1})')
ylabel('Intensity')
```

```
  ylim([-3.4 1.5])
% xlim([min(w3) max(w3)])
% ylim([0 1.1])
  xlim([1600 3100])


 %

% figure
% contourf(t2(12:end), w3, d1(:,12:end), 30)
% set(gca, 'fontname', 'arial', 'fontsize', 20, 'fontweight', 'bold', 'tickdir', 'out')
% title('DOAr-ND2 PP array, \tau_2=100 -> 1700 fs')
% xlabel('\tau_2 (fs)')
% ylabel('\omega/2\pic (cm^{-1})')


%%

% c2=find(w3>=1895,1); % ND2
% c1=find(w3>=1797,1); % ND2
% c1=find(w3>=2201,1);

% c1=find(w3>=1963,1); % 2PP
% c1=find(w3>=2690,1);

% c1=find(w3>=1994,1); % 2PP
% c1=find(w3>=2728,1);

  c1=find(w3>=1890,1); % HBQ
% c1=find(w3>=2770,1);

% c1=find(w3>=1895,1); % HBQ
% c2=find(w3>=2692,1);

% c1=find(w3>=1899,1); % HBQOD
% c1=find(w3>=2075,1);

% ps=  2;
% c1=p( ps);

  % e1=abs(min(a1(c1,:)));
    e1=abs(max(a1(c1,:)));
  % e3=max(a3(c1,:));
  % e4=max(a4(c1,:));


figure
hold on
  plot(t2,     a1( (c1),:)./e1, 'r', 'linewidth', 2)  % 17 -> 100fs for CH2
  plot(t2,     a2(c1,:)./e1, 'b', 'linewidth', 2)  % 17 -> 100fs for CH2
```

```
  plot(t2,     a3(c1,:)./e1, 'g', 'linewidth', 2)  % 17 -> 100fs for CH2
  plot(t2,     a4( (c1),:)./e1, 'm', 'linewidth', 2)  % 17 -> 100fs for CH2
  plot(t2z, It2z, ':k', 'linewidth', 2)
  set(gca, 'fontname', 'arial', 'fontsize', 20, 'fontweight', 'bold')
  set(gca, 'tickdir', 'out', 'TickLength', [0.03, 0.01], 'LineWidth',1.5);%XTick',-200:300:1600,
'XMinorTick', 'off')
% fun=['title(" Trace of DOAr-ND_2 at \omega=' int2str(w3(c1)) ' fs ")'];
% fun=['title(" Trace of 2PP at \omega=' int2str(w3(c1)) ' fs ")'];
  fun=['title(" Trace of HBQ at \omega=' int2str(w3( (c1))) ' fs ")'];
   eval(fun)
   legend('PP-P', 'PP-X', 'PP-Iso', 'PP-Ani')
 % legend('PP-P', 'PP-X', 'PP-Iso')
  xlabel('\tau_2 (fs)')
  ylabel('Intensity')
  xlim([-250 4000])

%%

Drive\Chemistry\Research\Winter14\PCET\HBQ\Data\20141121\Analysis\P';
% pat2='C:\Users\Anthony\Google
Drive\Chemistry\Research\Winter14\PCET\HBQ\Data\20141121\Analysis\X';
% pat2='C:\Users\Anthony\Google
Drive\Chemistry\Research\Winter14\PCET\HBQ\Data\20141121\Analysis\Iso';
% pat2='C:\Users\Anthony\Google
Drive\Chemistry\Research\Winter14\PCET\HBQ\Data\20141121\Analysis\AnR';

  cd(pat2);

 %%

   load smat smat
   load pmat pmat
   load ktsubmat ktsubmat
   load ktfit ktfit
   load tgmat tgmat
   load bounds bounds
   load SEpmat SEpmat
   load phimat phimat

%% Calculated Parameters using Guassian fits%%%%

gp=01;

% Gfactor=sqrt(2*log(2));  %analytical FWHM factor for a Gaussian
Gfactor=sqrt(2);  %analytical FWHM factor for overlapping Gaussian
sigma_fs= 38;
t0=  25;

sigma_ps=sigma_fs/1000;
FWHM=Gfactor*sigma_ps;
```

```
kt=length(t2);
% pts=length(d1(:,1));
% sp=v01s;
% sp=find(p==c1,1);

ts=find(t2>=  90,1);
   %ND2 90fs
   %HBQ-2PP 110

%%

  for sp=v12s+41:v12s+41

pts=p(sp);
st=p(sp);

tlength=ts:kt; %From  ts fs and beyond

time_ps=t2(tlength  )./1000;
time_fs=t2(tlength  );
time_s=t2(tlength  )./1E15;

for n=st:pts
    parp(n,:)= a1(n,tlength);
    parx(n,:)= a2(n,tlength);
    pari(n,:)= a3(n,tlength);
    para(n,:)= a4(n,tlength);
end



%figure
%plot(time_ps, par2(41,:))

plen=length(p);


pm=zeros(plen,16);
SEw=zeros(plen,16);
bound=zeros(2,15);

time=time_ps;

 % Fitting – choose appropriate exponential fit

  % Biexp Fit + C
A0=-5.58e-04 ;
tau0=0.148;
```

```
A1=-4.7e-06  ;
tau1= 1.855;
A2=-1.56e-5   ;
  w0=[     A0,  tau0,      A1, tau1,       A2];
  lb=[  -1e-1, 0.015,   -1e-2, 0.02,  -4.0e-3 ];
  ub=[   1e-1, 0.250,    1e-2, 5.38,   4.0e-3 ];
% w0=[   A0, tau0,    A1, tau1 ];
% lb=[-5e+1, 0.00, -3e+1,  0.3 ];
% ub=[ 0e+1, 0.30,  0e+1,  5.0 ];
options=optimset('MaxFunEvals', 1000000, 'MaxIter', 1000000);

    r=st    ;
    y=pari(st,:);
    [w, resnorm, residual, exitflag,output,lambda,jacobian]=lsqnonlin('exp_fxn_2',w0,lb,ub,options);
      yfit1 = w(1).*exp((-1.*time)./w(2));
      yfit2 = w(3).*exp((-1.*time)./w(4));
      yfit = yfit1 + yfit2 + w(5);
    ktsub(st,:) = (y - yfit );
    wlen=length(w);
    pm(st,1:wlen) = w;
    pm(st,end)=resnorm;
    ktft(st,:) = yfit;
    ci=nlparci(w, residual, 'jacobian', jacobian, 'alpha', 0.10);

 % Std Error of params
% If a 95% confidence interval is available for an absolute measure of intervention effect (e.g. SMD,
risk difference, rate difference), then the standard error can be calculated as
% SE = (upper limit – lower limit) / 3.92.
    % For 90% confidence intervals divide by 3.29 rather than 3.92; for 99% confidence intervals
divide by 5.15

 for ii=1:wlen
    SE(:,ii)=(ci(ii,2)-ci(ii,1))./3.29;
 end
    SEw(st,1:wlen)=SE(1,1:wlen);

 %

figure
  axis square
  box on
hold('on')
 plot(time, (y( 1,:)), '-ok','linewidth',2)
 plot(time,ktft(st,:), '-b','linewidth',2)
 plot(time,ktsub(st,:), '-r','linewidth',2)
%plot(time,yfit1(  :), 'og','linewidth',2)
%plot(time,yfit2(  :), '.b','linewidth',1)
%plot(time,yfit3(  :), ':m','linewidth',2)
%plot(time,yfit4(  :), ':y','linewidth',2)
 plot(t2zps, It2z, ':k', 'linewidth', 2)
```

```
set(gca, 'Tickdir', 'out','FontWeight','bold','FontSize',20)
set(gca, 'FontName', 'Arial','TickLength', [0.03, 0.01],'LineWidth', 2)
  func=['title(" ND_2 Pump-probe Trace at \omega_3=' int2str(w3(p(sp))) ' cm^{-1} ")'];
% func=['title(" 2PP Pump-probe Trace at \omega_3=' int2str(w3(p(sp))) ' cm^{-1} ")'];
% func=['title(" HBQ Pump-probe Trace at \omega_3=' int2str(w3(p(sp))) ' cm^{-1} ")'];
 eval(func)
ylabel('\DeltaA')
xlabel('\tau_2 (ps)')
% legend('Data', 'Fit', 'Difference', 'Component 1', 'Component 2', 'Component 3')%'Component 4')
% legend('Data', 'Fit', 'Difference')
% legend('boxoff')
 %xlim([time(1) time(end)])
  xlim([-0.03  4.0])
hold('off')

 %

tp0=time_ps(1);
t20=find(t2>=0,1);
tlen1=length(t2(1:end));
tlen2=length(t2(t20:end));
% time_step=round(t2(t20+1)-t2(t20));
time_step=time_step1;

dt=time_step/1000;
  et=t2(end)./1000;

if t2(ts)>0
   t1s=ts-t20+1;
      g1=t1s;
      g2=1;
else
   t1s=t20-ts+1;
      g1=1;
      g2=t1s;
end

t2s=t1s-1;

ktsub1=zeros(plen,tlen2);

      k2l=length(ktsub(1,g2:end));
      k1l=length(ktsub1(1,g1:end));
   ktsub1(st,g1:end)=ktsub(st,g2:end    );

time1= 0:dt:et;


for z=st:pts
   parz(z,:)=interp1(time_ps1, ktsub1(z,:), time1);
```

```
end

 % Making sure to zero-pad from zero to beginning of fit

time2=time1;
 %
tplen=length(time2);

if isnan(parz(st,1))==1;
   Nap=isnan(parz(st,:));
   gq=find(Nap<0.5,1,'first');
else
   gq=1;
end

gp1=find(parz(st,gq:tplen)>0,1)+1;

 % Apodization Functions

  sm(st,gq:tplen)=parz(st,gq:tplen);

  for cq=1:gq
    sm(:,cq)=parz(:,gq);
  end
%   time2=time;%(gq:tplen)-time(gq);

  tnlen=length(time2);

  sml=length(sm(:,1));

[rNR cNR]=size(sm );

cNR=cNR';

anr1=1-((1./cNR).*(1:1:cNR)); % Using a line from y = 1 to y = 0 with slope corresponding to the
length of R,NR

fzlfac=1.00;
ftlfac=0.75;
fplfac=0.5;

%Building more apodization functions

% anrz1=nuttallwin(2*fzlfac*cNR)';
% fzlen=round(length(anrz1)/2);
% anrz2=anrz1(fzlen+1:end);
% anrz(1:fzlen)=anrz2;
% anrz(fzlen+1:tnlen)=0;
%
%
```

```
% anrt1=nuttallwin(2*ftlfac*cNR)';
% ftlen=round(length(anrt1)/2);
% anrt2=anrt1(ftlen  :end);
% anrt(1:ftlen)=anrt2;
% anrt(ftlen+1:tnlen)=0;

anrp1=nuttallwin(2*fplfac*cNR)';
fplen=round(length(anrp1)/2)  ;
anrp2=anrp1(fplen+1:end);
anr(1:fplen)=anrp2;
anr(fplen+1:tnlen)=0;


  %

for z=st:pts;
   for fl=1:tnlen
    ymea(z,fl)=mean( sm(z,gp1:tnlen));
   end
%    ysub2(z,:)=( sm(z,:)-ymea(z,:)).*anr ;
   ysub2(z,:)=( sm(z,:)-    0    ).*anr ;
%    cur(z,:)=mean(ymis2(z,:));
%   ymisa(z,:)=sm(z,:).*anr;
%   ymisb(z,:)=sm(z,:).*anr1;
%   ymea2(z,:)=mean(ymisa(z,:));
%   ymis2(z,:)=ymisa(z,:)-ymea2(z,1);
   ysubf0(z,:)=fft(ysub2(z,:), 8192);
   ysubf1(z,:)=fftshift(ysubf0(z,:));
   phif1(z,:)=unwrap(angle(ysubf1(z,:)));
end

  % Plotting to examine application of filter

xm=max(sm(st,:));

%   figure
%   hold on
%   plot(time_ps1, ktsub1(st,:), '-r', 'linewidth', 2)
% % plot(time2, sm(st,:), '-g', 'linewidth', 2)
%   plot(time2, xm*anr , ':k', 'linewidth', 2)
% % plot(time2, xm*anrt, ':r', 'linewidth', 2)
% % plot(time2, xm*anrz, ':b', 'linewidth', 2)
% % plot(time2, ymea(st,:), '-m', 'linewidth', 2)
%   plot(time2, ysub2(st,:), '-b', 'linewidth', 2)

  %

ft=length(ysubf1(1,:));

for v = 1:ft
```

```
    newfreq(v)=v/(ft*time_step);
end

g=0:1:ft;
freq1=zeros(size(g));
freq2=newfreq(1:ft/2);
freq2=fliplr(freq2);
freq2=freq2.*(-1);
freq1(1:ft/2)=freq2;
freq1(ft/2+1)=0;
freq1(ft/2+2:end)=newfreq(1:ft/2);

t2en=time(end)*1000;

w2start=round(0*ft*3*time_step/100000+ft/2+1);
w2end=round(1200*ft*3*time_step/100000+ft/2+1);
w2=freq1(w2start:w2end)'./3e-05; % c = 3E-05 cm/fs

 %

ysubf2 = ysubf1(:,w2start:w2end);
phif2 = phif1(:,w2start:w2end);

phidq = phif2*(180/pi());
phiInt=round( phidq./360);
IntMed=median(phiInt,2);

for z= 1:sml
    phid2(z,:)=phidq(z,:) - 360*IntMed(z);
end

phif3=phid2.*(pi()/180);

ysubf2n=ysubf2./max(ysubf2(z,:));


tgm(st,:)=ysubf2(st,:);

 %

pl1=length(pm(1,:));
se1=length(SEw(1,:));
sl1=length(sm(1,:));
ktl1=length(ktft(1,:));
ktl2=length(ktsub(1,:));

bounds(:,:,sp) = bound(:,:);
pmat(sp,1:pl1) = pm(st,:);
SEpmat(sp,1:se1) = SEw(st,:);
smat(sp,1:sl1) = sm(st,:);
```

```
ktfit(sp,1:ktl1) = ktft(st,:);
ktsubmat(sp,1:ktl2) = ktsub(st,:);
tgmat(sp,:) = tgm(st,:);
phimat(sp,:) = phif2(st,:);

% bounds(:,:,sp) = bound(:,:);
% pmat(sp, :   ) = pm(st,:);
% SEpmat(sp, :   ) = SEw(st,:);
% smat(sp, :   ) = sm(st,:);
% ktfit(sp, :    ) = ktft(st,:);
% ktsubmat(sp, :    ) = ktsub(st,:);
% tgmat(sp,:) = tgm(st,:);
% phimat(sp,:) = phif2(st,:);

  end

%%

 save smat smat
 save pmat pmat
 save ktsubmat ktsubmat
 save ktfit ktfit
 save tgmat tgmat
 save bounds bounds
 save SEpmat SEpmat
 save phimat phimat
   save time time
   save time2 time2
   save w2 w2
% end
```

A.5 Gaussian 09C Input File

Here is an example of the input file for DOAr-ND_2 for calculating the IR frequencies and anharmonic corrections and coupling constants. DOAr-ND_2 was chosen for the sample file due to it being the more difficult of the four to achieve non-imaginary frequencies from the anharmonic calculations after optimization.

```
%chk=DOAr-ND2-freq-anh_2.chk
%nprocs=8
%mem=23500MB
#p opt=verytight int(grid=150770) ub3lyp/6-311++g(d,p) freq=anharmonic

Freq calc of DOAr-6-CMe2ND2 where DOAr = phenol-d

0 1
 H(Iso=2)         -1.35277600   -2.00181900   -0.36456000
 O               -0.43623200   -2.20711900   -0.05831200
 C                0.24311500   -1.02514700   -0.04294300
```

C	-0.41057500	0.22440100	-0.05497100
C	0.38298300	1.37948900	-0.04159000
C	1.77504100	1.33211300	-0.00236500
C	2.38467200	0.07385300	0.02580700
C	1.64727800	-1.10551900	0.00191000
H	-0.09403100	2.35193500	-0.05433900
H	3.46888800	0.00782200	0.06092300
C	-1.94642900	0.30343700	0.00773900
N	-2.49678800	-0.75352500	-0.89403300
C	-2.41840000	-0.03156000	1.43857400
C	-2.50069500	1.68162800	-0.39544300
H(Iso=2)	-2.30346500	-0.52223100	-1.86555700
H(Iso=2)	-3.50634200	-0.81322800	-0.79262100
H	-2.06320700	-1.01479700	1.75108600
H	-3.51281200	-0.02260300	1.49677400
H	-2.03580600	0.71047500	2.14171200
H	-2.16288300	1.96965000	-1.39477300
H	-2.20672500	2.46689700	0.30433700
H	-3.59399600	1.64244100	-0.40154000
C	2.30994200	-2.45841500	0.02358200
H	2.00996800	-3.03338300	0.90482400
H	2.01880600	-3.05369400	-0.84663800
H	3.39714500	-2.35797100	0.03007600
C	2.60450500	2.59525000	-0.00057300
H	1.97503500	3.48306700	0.09466700
H	3.31943800	2.60412600	0.82802200
H	3.18151200	2.69774700	-0.92603700

A.6 Useful Scripts

The following scripts are useful for extracting information from Gaussian09C output files. These scripts could be combined in executables to achieve desired results. At the time of writing this dissertation this has not be achieved.

Awk,Grep scripts that are useful

sparse data file by line to new data file

-$: awk 'NR==[starting line number],NR==[ending line number]' filename > newfile.txt

Find line number of a pattern

-$: grep -[option which is n for line number] ‘pattern’ filename

Ex: (-in ; i = case insensitive , n=give line number)
grep -in ‘68 68 68’ DOAr-ND2-freq-anh_2.log
➔ 400515: 68 68 68 3.26494 0.00278 0.00009

-$: sed -i "s line,to-line \ [find pattern] \ [replace with] \ option/where to look" [file]

VITA

Anthony D. Reynolds was born in Abingdon, Virginia and attended high school at Twin Springs High School in Nickelsville, Virginia. In 2005, he started undergraduate studies in chemistry and history at Berea College where he received his Bachelors of Arts in chemistry with a minor in history in 2009. Anthony continued pursuing his interest in chemistry at the University of Washington, in 2009, culminating in a PhD of chemistry in 2015. While at the University of Washington, he studied under the direction of Munira Khalil investigating low frequency molecular modulations anharmonically-coupled to high frequency hydroxyl/deuteroxyl vibrational modes in proton-coupled electron transfer model systems.